Bernard Barbara

Statement

and

Readings

Abstract

Bernard Barbara

A short review will be given of experimental aspects of decoherence in solid state qubits, including magnetic and superconducting qubits. Most important decoherence mechanisms will be discussed, for single or ensembles of qubits with or without excitation pulse, with different dimensions and degrees of complexity. More specific subjects, such as the effects of decoherence on magnetic molecules or in quantum phase transitions, will be tackled.

LETTERS

Quantum oscillations in a molecular magnet

S. Bertaina[1]†, S. Gambarelli[2], T. Mitra[3], B. Tsukerblat[4], A. Müller[3] & B. Barbara[1,2]

The term 'molecular magnet' generally refers to a molecular entity containing several magnetic ions whose coupled spins generate a collective spin, S (ref. 1). Such complex multi-spin systems provide attractive targets for the study of quantum effects at the mesoscopic scale. In these molecules, the large energy barriers between collective spin states can be crossed by thermal activation or quantum tunnelling, depending on the temperature or an applied magnetic field[2–4]. There is the hope that these mesoscopic spin states can be harnessed for the realization of quantum bits—'qubits', the basic building blocks of a quantum computer—based on molecular magnets[5–8]. But strong decoherence[9] must be overcome if the envisaged applications are to become practical. Here we report the observation and analysis of Rabi oscillations (quantum oscillations resulting from the coherent absorption and emission of photons driven by an electromagnetic wave[10]) of a molecular magnet in a hybrid system, in which discrete and well-separated magnetic V_{15}^{IV} clusters are embedded in a self-organized non-magnetic environment. Each cluster contains 15 antiferromagnetically coupled $S = 1/2$ spins, leading to an $S = 1/2$ collective ground state[11–13]. When this system is placed into a resonant cavity, the microwave field induces oscillatory transitions between the ground and excited collective spin states, indicative of long-lived quantum coherence. The present observation of quantum oscillations suggests that low-dimension self-organized qubit networks having coherence times of the order of $100\,\mu s$ (at liquid helium temperatures) are a realistic prospect.

In the context of quantum computing, it was recently discussed how the decoherence of molecular magnet spin quantum bits could be suppressed, with reference to the discrete low spin clusters V_{15} and Cr_7Ni (ref. 7; see also refs 8 and 14). In both systems, their low spin states cause weak environmental coupling[7], making them candidates for the realization of a long-lived quantum memory. Measurement of the spin relaxation time τ_2 in Cr_7Ni was subsequently reported and found to be interestingly large[15,16]; however, the important Rabi quantum oscillations were not observed, probably because electronic and nuclear degrees of freedom were too strongly linked to each other. As these oscillations have until now only been observed in non-molecular spin systems (see, for example, refs 17–20), it has remained an open question whether quantum oscillations could in principle be realized in molecular magnets[7,8]. This question is now answered by our observation of quantum oscillations of the Rabi type in V_{15}. The main reason for this success lies in the fact that the important pairwise decoherence mechanism[7,8] associated with dipolar interactions could be strongly reduced.

Before discussing the observed quantum oscillations, we first briefly describe the magnetic/electronic structure of the V_{15}^{IV} species as determined experimentally. Following the synthesis of the quasi-spherical mesoscopic cluster anion $\left[V_{15}^{IV}As_6^{III}O_{42}(H_2O)\right]^{6-}$ ($\equiv V_{15}$) nearly two decades ago (ref. 11), the properties of this molecule have

received considerable attention (see, for example, refs 1, 11, 14, 21–25). The V_{15} cluster with an $\sim 1.3\,nm$ diameter exhibits an unique structure with layers of different magnetizations: a large central V_3^{IV} triangle is sandwiched by two smaller V_6^{IV} hexagons[11] (Fig. 1). The 15 $S = 1/2$ spins are coupled by antiferromagnetic super-exchange and Dzyaloshinsky–Moriya (DM) interaction[13,21–25] (see also refs 26, 27) through different pathways, which results in a collective low spin ground state with $S = 1/2$ (refs 12, 13, 24, 25).

Energy spectrum calculations for the full cluster spin space give two $S = 1/2$ (spin doublet) ground states slightly shifted from each other by DM interactions, and an $S = 3/2$ (spin quartet) excited state; these states are 'isolated' from a quasi-continuum of states lying at energy $E/k_B \approx 250\,K$ above the $S = 3/2$ excited state. These low-lying energy states can be obtained with a good accuracy using the generally accepted three-spin approximation (valid below $100\,K$), in which the spins of the inner triangle are coupled by an effective interaction $|J_0| \ll |J'|$ mediated by the spins of the hexagons[12,13,21–25] (Fig. 2 and Methods; J_0 and J' are shown in Fig. 1b).

The spin hamiltonian of V_{15} can be written as:

$$H = -J_0 \sum_{\substack{i,j=1 \\ (i<j)}}^{3} \mathbf{S}_i \mathbf{S}_j + \sum_{ij=12,13,31} \mathbf{D}_{ij}\left(\mathbf{S}_i \times \mathbf{S}_j\right) + A\sum_{i=1}^{3}\mathbf{I}_i\mathbf{S}_j + g\mu_B\mathbf{H}\sum_{i=1}^{3}\mathbf{S}_i \quad (1)$$
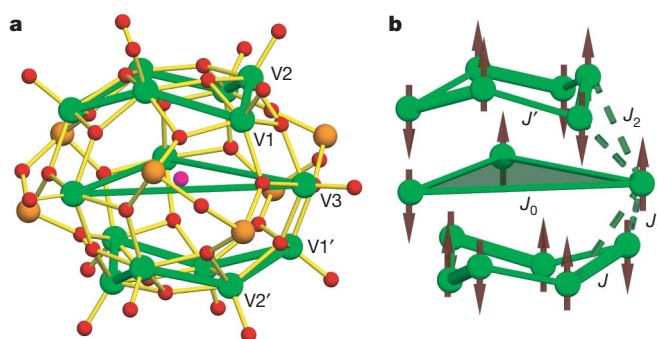

Figure 1 | Structure and exchange interaction pathways of the cluster anion $\left[V_{15}^{IV}As_6^{III}O_{42}(H_2O)\right]^{6-}$. a, The cluster is shown in ball-and-stick representation (green, V; orange, As; red, O). The outer V_6 hexagons are highlighted by thick green lines. A weak deviation from trigonal symmetry can be attributed to the water molecule located in the centre of the cavity (O of the encapsulated water molecule in purple) or/and to the presence of water in the lattice between molecules. The different types of V ions, namely V1, V2, V3, V1′ and V2′, are shown for the definition of different exchange pathways. **b**, Sketch showing the spin arrangement at low temperatures (three-spin approximation), emphasizing some of the exchange interaction pathways (J, J_1, J_2, J'). The coupling J_0 between the spins of the inner triangle is not direct but results from different exchange pathways through the hexagons. The magnetic layer system is defined by one V_3 triangle sandwiched by two V_6 hexagons (for further details see text).

[1]Institut Néel, CNRS, 25 Ave. des Martyrs, BP166, 38042 Grenoble Cedex 9, France. [2]Laboratoire de Chimie Inorganique et Biologique (UMR-E3 CEA-UJF), INAC, CEA-Grenoble, 17 Ave. des Martyrs, 38054 Grenoble Cedex 9, France. [3]Fakultät für Chemie, Universität Bielefeld, Postfach 100131, D-33501 Bielefeld, Germany. [4]Department of Chemistry, Ben-Gurion University of the Negev, PO Box 653, 84105 Beer-Sheva, Israel. †Present address: National High Magnetic Field Laboratory, Florida State University, 1800 East Paul Dirac Drive, Tallahassee, Florida 32310, USA.

where $\mathbf{D}_{ij}$ is the antisymmetric vector of the DM interaction associated with the pair ij, and A is the hyperfine coupling constant of the ^{51}V isotope (see below). The six components of $\mathbf{D}_{ij}$ can be expressed in terms of two parameters, namely D_Z (perpendicular to the plane) and D_{XY} (in-plane). The DM interaction removes the degeneracy of the two low-lying doublets and produces a first order zero-field splitting $\Delta_{DM} \approx \sqrt{3}D_Z$ (plus small second order corrections)[22–25]. The excited (quartet) state shows only a second order splitting caused by a small inter-multiplet mixing through the in-plane component of DM coupling, that is, $\Delta'_{DM} = -D_{XY}^2/8J_0$ (refs 24, 25). The energy separation between the doublet states and quartet state is given by $3J_0/2 \approx -3.67$K (refs 13, 21–25). Figure 2 shows the level scheme calculated by diagonalization of the hamiltonian (equation (1)), with only one free parameter $D_Z \approx 43$ mK adjusted to fit the positions of the measured resonances (a value close to that obtained from magnetization data[13,21,24]), and $D_{XY} = 0$, a choice conditioned by the fact that the transverse DM component has a negligible effect on resonance fields below 0.5 T (this is important in the calculation of transition probabilities only). To ensure legibility, hyperfine interactions are not included in Fig. 2 (they simply broaden the levels).

A new hybrid material, based on the use of a cationic surfactant—DODA ($\left[Me_2N\{(CH_2)_{17}Me\}_2\right]^+$)—as an embedding material for the anionic clusters, was developed for the present work (see Methods). The related frozen system contains V_{15} clusters integrated into the self-organized environment of the surfactant. The clusters—prepared according to ref. 11—were extracted from aqueous solution into chloroform by the surfactant DODA present in large excess. The surfactants, which wrap up the cluster anions, are amphiphilic cations, with their long hydrophobic tails pointing away from the cluster anions, enabling solubility in chloroform. The procedure ensures that the cluster anions cannot get into direct contact with one another; they are clearly separated by the surfactants (mean distance $\sim$13 nm).

Electron paramagnetic resonance (EPR) experiments were performed on this hybrid material at $\sim$4 K using a Bruker E-580 X-band continuous-wave (CW) and pulsed spectrometer operating at 9.7 GHz. The CW-EPR spectrum, recorded at 16 K on a frozen sample, corresponds precisely to that obtained in the solid state in a previous study[12]. In particular, the resonance field shows the same profile and line-width ($\sim$30 mT), compatible with the g-tensor values of a single crystal ($g_{//} = 1.98$ and $g_{\perp} = 1.95$). The measured transition width $W \approx 35$ mT is directly connected with the energy E occurring in the expression of decoherence calculated for a multi-spin molecule[7,8] (see below). Note that this transition width W should be associated with $S = 3/2$, the EPR spectrum being dominated by the excited quartet.

Rabi oscillations were recorded using a nutation pulse of length t, followed (after a delay greater than τ_2) by a $\pi/2-\pi$ sequence. Experimental results showed two different types of Rabi oscillations, corresponding to the resonant transitions 1, 2 and 3 for $S = 3/2$ spins, and 4, 5, 6 and 7 for $S = 1/2$ spins, here called '3/2' and '1/2', respectively (Fig. 3b and a, respectively). Although both types of oscillation are associated with the same collective degrees of freedom of the clusters, they show very different behaviour. In particular, the first type of Rabi frequency compares well with that of a single spin-3/2 system, whereas the Rabi frequency of the second type is much smaller than that of a single spin-1/2. This is a consequence of selection rules: the transition type '3/2' is always allowed, whereas the transitions 5 and 7 of the '1/2' type occur only due to transverse DM interactions or/and breaking of the C_3 symmetry[25] (Methods). Therefore we obtained Rabi oscillations with quite different frequencies, $\Omega_{R\,3/2} \approx 18.5 \pm 0.2$MHz and $\Omega_{R1/2} \approx 4.5 \pm 0.2$MHz, and a small ratio of transition probabilities (or intensities) $R < 6 \times 10^{-2}$ (Fig. 3, Methods). When the transition '1/2' is excited (by a single excitation pulse), a whole spectrum of Rabi oscillations is generated. The frequency of the detected oscillation depends on the characteristics of the detection pulse, such as its length or its amplitude (Fig. 3). This
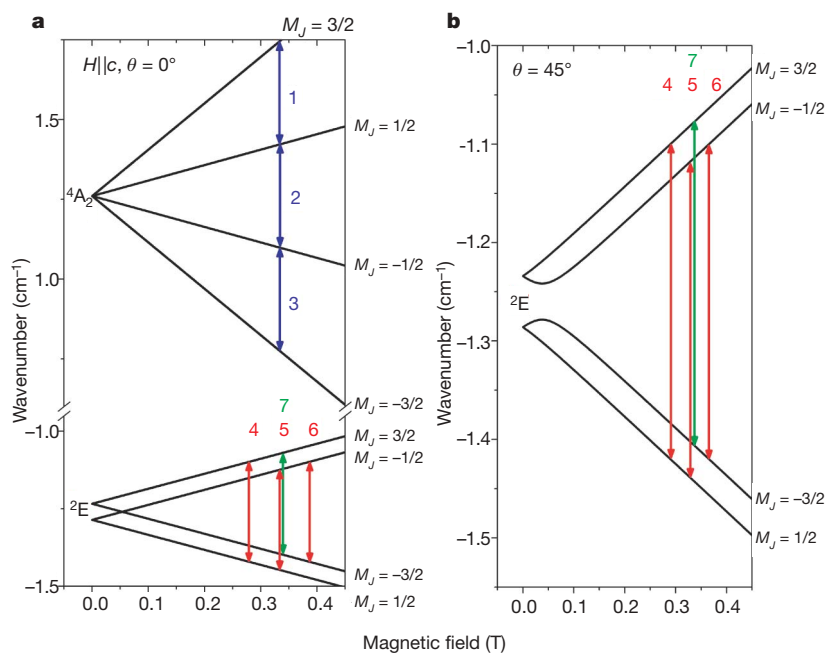

Figure 2 | Low-energy EPR transitions. These calculated diagrams used parameter values $g \approx 1.96$, $J_0 \approx -2.45$ K, $D_Z \approx 43$ mK and $D_{XY} = 0$ (see text for details). **a**, The magnetic field is parallel to the c axis. Whereas the orbital singlet $^4A_2$ ($S = 3/2$) gives the superposition of the three transitions 1, 2, and 3, the orbital doublet ^2E ($S = 1/2$) gives two inter-doublet transitions 4 and 6 which are basically allowed, as well as two intra-doublet transitions 5 and 7 (which are respectively allowed by transverse DM interactions and non-symmetrical exchange interactions due to a small deviation from the trigonal symmetry[24] (Methods)). Second order zero-field splitting of $^4A_2$ and small splitting of the lines 1, 2, and 3 is not shown. The M_I labels correspond to the quantization axis along the DM anisotropy field. **b**, Shown are the transitions 4, 5, 6, and 7 for the angle $\theta = 45°$ between the field and cluster C_3-axis. The M_I labels correspond to the quantization axis along the field in the strong field limit. The boundaries of the measured resonance fields of Fig. 4 correspond to the field distribution given by the positions of labels 4, 5, 6 and 7 above the curves. The blue transitions correspond to $S = 3/2$; the red and the green transitions correspond to $S = 1/2$.

spectrum is due to the presence of an avoided level crossing and the special selection rules; these are caused by the uniaxial anisotropy introduced by the DM interactions in the spin-frustrated (orbitally degenerate) ground state giving the overlapping transitions 4–7 (Fig. 2). The glassy character of the investigated frozen material is also relevant here; this material contains different cluster orientations, leading to a distribution of transverse field components, which gives a scattering of the coefficients of the states entering in the two-level wavefunctions $|\varphi_1\rangle$ and $|\varphi_2\rangle$ and therefore a distribution of the Rabi frequencies $\Omega_{R\,1/2} \propto |\langle\varphi_1|S_+|\varphi_2\rangle|$ (Fig. 2 and Methods). Whereas the splitting of the excited quartet state in a magnetic field is almost isotropic, the distribution function of the associated Rabi frequency is very narrow.

An extension of the experiments shown in Fig. 3 to other values of the applied field showed that Rabi oscillations could be detected for each value of the applied field below 500 mT, while the transitions are inhomogeneously broadened. Figure 4 gives the result of a systematic investigation, consisting of the measurement of the spin-echo intensity at time $t = 0$ in a sweeping magnetic field. Two broad resonance distributions are observed, which correspond to the Rabi oscillations '3/2' and '1/2' of Fig. 3b and a, respectively, which were measured near the maxima $H_{3/2} \approx 357$ mT and $H_{1/2} \approx 335$ mT of the curves of
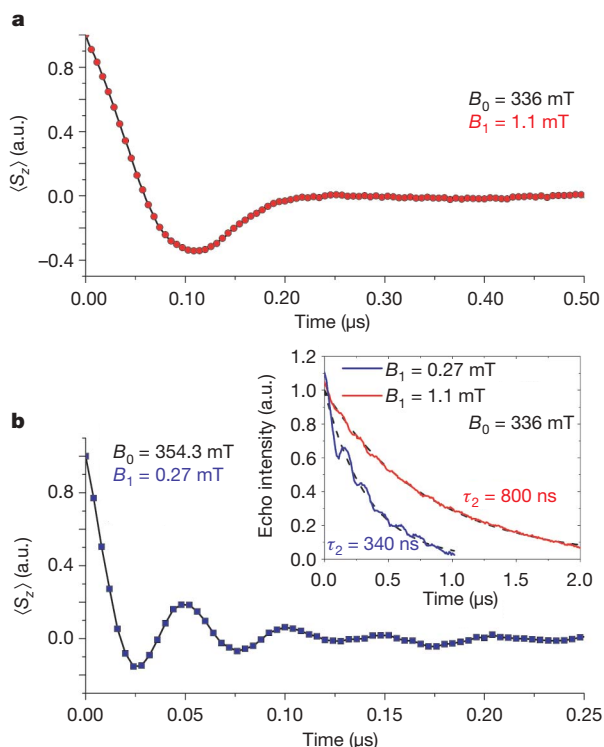
Fig. 4. Whereas the nearly symmetrical type '3/2' distribution shows resonances which are optimally excited by pulse durations and powers similar to those generally used for isolated 3/2 spins, the asymmetrical type '1/2' distribution shows resonances requiring larger power and pulse length, confirming much smaller transition probabilities. The observed inhomogeneous widths ($\sim 50 \pm 10$ mT) result from the existence of different transitions—that is 1 to 3 and 4 to 7 shifted by the longitudinal field components associated with the glassy character of the frozen solution. The width of the resonance of type '1/2' (Fig. 4) fits the transition fields calculated from the hamiltonian (equation (1)) for the resonances 4 to 7 with limiting angles $\vartheta = 0$ and $\pi/2$ (Fig. 2), whereas the width of the resonance of type '3/2' is simply given by the unique resonance field of transitions 1 to 3 (Fig. 2 a). In both cases, the ^{51}V hyperfine interactions contribute equally to the resonance widths.

To conclude, it was possible to entangle the 15 spins of a molecular magnet—a complex system which, formally speaking, entails a Hilbert space of dimension $D_H = 2^{15}$ (Methods)—with photons by performing pulse EPR experiments on a frozen solution of randomly oriented and well separated clusters. Despite the complexity of the system[11–14,21–25] (involving in a formal consideration dozens of cluster electrons and nuclear spins of ^{51}V, ^{75}As and ^{1}H), long-lived Rabi oscillations[10] were generated and selectively detected. An analysis, based on the widely used three-spin approximation of V_{15} (refs 12, 13, 21–25; the related interactions are mediated by the 12 other spins) gives a global interpretation of the results.

The observed coherence on the microsecond timescale seems to be mainly limited by the bath of nuclear spins. Each V_{15} cluster is correspondingly weakly coupled to 36 first-neighbour protons of the six DODA methyl groups distributed around the cluster, and to two water protons at the cluster centre. According to the charge ($6-$) of V_{15}, six cationic DODA surfactants are relevant, with their positively charged parts (six dimethyl groups) attached to the O atoms of the cluster surface (see also ref. 28); the corresponding neutral hybrid just leads to the solubility in the organic solvent. The distance from the H atoms of a methyl group to a V^{IV} is ~ 0.45 nm. For this typical spin–proton distance, the half-width of the gaussian distribution of the coupling energy of a cluster/surfactant unit is $E \approx 3.5$ mK, giving, for the level separation $\Delta \approx 0.4$ K (Fig. 2), the coherence time[7,8]

Figure 3 | Generation and detection of Rabi oscillations. a, Time evolution of the average spin $\langle S_z \rangle$ after a spin-echo sequence. The '1/2' type transition observed near the maximum of the corresponding resonance of Fig. 4 (B_0, 336.0 mT) requires unusually large excitation power $B_1 = 1.1$ mT and pulse length $T_{\pi/2} = 64$ ns. It corresponds to the transitions 4–7 of Fig. 2. The Rabi frequency $\Omega_R = 4.5$ MHz was selected by a detection pulse with characteristics $B_1 = 0.3$ mT and $T_{\pi/2} = 200$ ns. **b,** The '3/2' type transition with Rabi frequency $\Omega_R = 18.5$ MHz was excited near the maximum of the corresponding resonance of Fig. 4 ($B_0 = 354.3$ mT). It requires excitation and detection pulses similar to those usually used for a single spin of 3/2 ($B_1 = 0.27$ mT, $T_{\pi/2} = 16$ ns) and corresponds to the transitions 1–3 of Fig. 2. Inset, spin-echo intensity measured versus time for both oscillations. The coherence times τ_2 obtained from exponential fits are inverse functions of the spin values: 800 ns for $S = 1/2$ (red) and 340 ns for $S = 3/2$ (blue). Superimposed oscillations, mainly observed on the '3/2' type curve come from the precession of proton spins[19]. These oscillations correspond to only a weak perturbation of the Rabi coherence. Temperature, 4 K for all results shown.
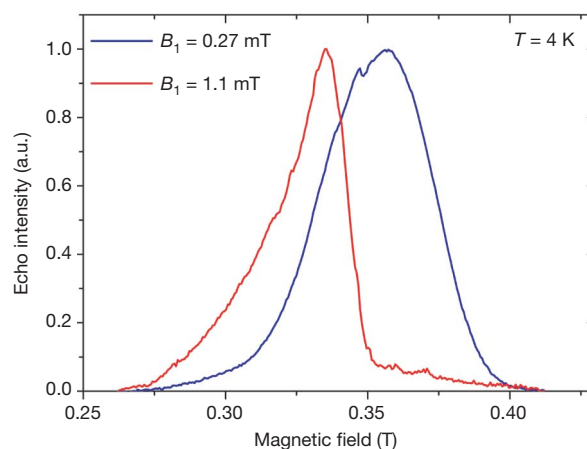

Figure 4 | Distribution of spin-echo intensities. The measurements were done in field sweep experiments for two excitation pulse configurations. The blue curve, corresponding to '3/2' type transitions (obtained with the excitation pulse $B_1 = 0.27$ mT and $T_{\pi/2} = 16$ ns), is nearly symmetrical and has a high transition probability. The red curve, corresponding to '1/2' type transitions (obtained with the excitation pulse $B_1 = 1.1$ mT and $T_{\pi/2} = 64$ ns), is asymmetrical and has a low probability (involving collective orbital degrees of freedom). The resonance fields form a 'band' due to random cluster orientations, while the corresponding distribution widths can be well explained by the dispersions of the resonance transitions 1–3 and 4–7.

$\tau_2^H = 4\pi\Delta/E^2 \approx 18\,\mu s$. The contribution of more distant neighbouring protons should reduce this value to a few microseconds. Regarding the decoherence effect from ^{51}V, the transition width $W \approx 35\,mK$ gives $E = W/2 \approx 17\,mK$ and $\tau_2^V = 0.75\,\mu s$, suggesting that the observed decoherence of the $S = 3/2$ resonances is almost entirely caused by the ^{51}V nuclear spins. The observed larger coherence time of the $S = 1/2$ transitions is presumably due to their smaller hyperfine coupling. In spite of the relatively high temperature of the measurement, the phonons' decoherence[7,8] $\tau_2^{ph} \propto S^{-4}$ is strongly lowered due to the low spin and anisotropy values involved in the electron–phonon[29,30] coupling $\propto |{<}i|S_yS_z + S_zS_y|f{>}|^2$, giving $\tau_2^{ph} \approx 100\,\mu s$, that is, $\tau_2^{ph} \gg \tau_2^H > \tau_2^V$. Finally, the pairwise decoherence mechanism originating from electronic dipolar interaction[7], which is usually considered as the most destructive, is nearly negligible, owing to the strong dilution of the clusters that results from the surfactant environment. This allows weak dipolar interactions only ($\sim 0.5\,\mu K$) and very large coherence times ($\tau_2^{pw} \approx 100\,\mu s$). A comparison of the different decoherence mechanisms suggests that coherence times greater than $100\,\mu s$ should be obtained in molecular magnets at liquid-helium temperatures if nuclear-spin-free molecules and deuterated surfactants are used.

The control of complex coherent spin states of molecular magnets—in which exchange interactions can be tuned by well defined chemical changes of the metal cluster ligand spheres—could finally lead to a way to avoid the 'roadblock' of decoherence. This would be particularly important in the case of self-organized one- or two-dimensional supramolecular networks, where well separated magnetic species could be addressed selectively, following different schemes already proposed for the molecular magnet option.

METHODS SUMMARY

When we refer to the three-spin approximation of V_{15} (refs 12, 13, 21–25), we consider the three spins located on each corner of the inner triangle (Fig. 1b). However these spins do not interact directly but via the other spins of the cluster. Strictly speaking, each hexagon contains three pairs of spins strongly coupled with $J \approx -800\,K$ ('dimers') and each spin of the inner triangle is coupled to two of those pairs, one belonging to the upper hexagon and one belonging to the lower hexagon ($J_1 \approx -150\,K$ and $J_2 \approx -300\,K$). This gives three groups of five spins with resultant spin $S = 1/2$ (superposition of 'entangled' states, coupled through inter-dimer hexagon superexchange $J' \approx -150\,K$), showing that, in fact, the three-spin approximation involves all of the 15 spins of the cluster and therefore the Hilbert space has the dimension $D_H = 2^{15}$ (D_H for the three-spin system is 2^3). This approximation simplifies the evaluation of the low-lying energy levels of the 15 'entangled' states of the V_{15} cluster. For $D_Z \neq 0$ the $S = 1/2$ orbital doublet ^2E, whose basis functions can be labelled by the quantum number of the total pseudo-angular momentum $M_J = M_L + M_S$, is associated with the pseudo-orbital momentum $M_L = +1$ or $M_L = -1$ (refs 24, 25). The allowed EPR transitions satisfy the subsequent selection rules: $\Delta M_L = 0$, $\Delta M_S = \pm 1$, that is $\Delta M_J = \pm 1$ for the inter-doublet transitions 4 and 6, and $\Delta M_L = \mp 1$, $\Delta M_S = \pm 2$, that is $\Delta M_J = \pm 1$ for the weak intra-doublet transition 5 whose transition probability is caused by a small intermultiplet mixing through the in-plane component of the DM coupling. The intensity of this transition is significantly increased when transition 7 becomes allowed due to a weak deviation from the C_3 symmetry (Fig. 1). This also leads to an increased zero-field gap $[\Delta_{DM}^2 + \delta^2]^{1/2}$ where δ is the parameter in the exchange shift $\delta S_1 S_2$.

Full Methods and any associated references are available in the online version of the paper at www.nature.com/nature.

1. Gatteschi, D., Sessoli, R. & Villain, J. *Molecular Nanomagnets* (Oxford Univ. Press, Oxford, UK, 2006).
2. Barbara, B. *et al.* Mesoscopic quantum tunneling of the magnetization. *J. Magn. Magn. Mater.* **140–144,** 1825–1828 (1995).
3. Thomas, L. *et al.* Macroscopic quantum tunneling of magnetization in a single crystal of nanomagnets. *Nature* **383,** 145–147 (1996).
4. Friedman, J. R. *et al.* Macroscopic measurements of resonant magnetization tunneling in high spin molecules. *Phys. Rev. Lett.* **76,** 3830–3833 (1996).
5. Leuenberger, M. N. & Loss, D. Quantum computing in molecular magnets. *Nature* **410,** 789–793 (2001).
6. Aharonov, D., Kitaev, A. & Preskill, J. Fault-tolerant quantum computation with long-range correlated noise. *Phys. Rev. Lett.* **96,** 050504 (2006).
7. Stamp, P. C. E. & Tupitsyn, I. S. Coherence window in the dynamics of quantum nanomagnets. *Phys. Rev. B* **69,** 014401 (2004).
8. Morello, A., Stamp, P. C. E. & Tupitsyn, I. S. Pairwise decoherence in coupled spin qubit networks. *Phys. Rev. Lett.* **97,** 207206 (2006).
9. Prokof'ev, N. V. & Stamp, P. C. E. Theory of the spin bath. *Rep. Prog. Phys.* **63,** 669–726 (2000).
10. Rabi, I. I. Space quantization in a gyrating magnetic field. *Phys. Rev.* **51,** 652–654 (1937).
11. Müller, A. & Döring, J. A novel heterocluster with D_3-symmetry containing twenty-one core atoms: $[As^{III}_6V^{IV}_{15}O_{42}(H_2O)]^{6-}$. *Angew. Chem. Int. Edn Engl.* **27,** 1721 (1988).
12. Gatteschi, D., Pardi, L., Barra, A. L., Müller, A. & Döring, J. Layered magnetic structure of a metal cluster ion. *Nature* **354,** 463–465 (1991).
13. Barbara, B. On the richness of supra-molecular chemistry and its openings in physics. *J. Mol. Struct.* **656,** 135–140 (2003).
14. Wernsdorfer, W., Müller, A., Mailly, D. & Barbara, B. Resonant photon absorption in the low spin molecule V_{15}. *Europhys. Lett.* **66,** 861–867 (2004).
15. Ardavan, A. *et al.* Will spin-relaxation times in molecular magnets permit quantum information processing? *Phys. Rev. Lett.* **98,** 057201 (2007).
16. Wernsdorfer, W. A long-lasting phase. *Nature Mater.* **6,** 174–176 (2007).
17. Mehring, M., Mende, J. & Scherer, W. Entanglement between an electron and a nuclear spin ½. *Phys. Rev. Lett.* **90,** 153001 (2003).
18. Morton, J. J. L. *et al.* Bang–bang control of fullerene qubits using ultrafast phase gates. *Nature Phys.* **2,** 40–43 (2006).
19. Bertaina, S. *et al.* Rare earth solid state qubits. *Nature Nanotechnol.* **2,** 39–42 (2007).
20. Nellutla, S. *et al.* Coherent manipulation of electron spins up to ambient temperatures in Cr^{5+} ($S=1/2$) doped K_3NbO_8. *Phys. Rev. Lett.* **99,** 137601 (2007).
21. Chiorescu, I., Wernsdorfer, W., Müller, A., Bögge, H. & Barbara, B. Butterfly hysteresis loop and dissipative spin reversal in the $S=1/2$, V_{15} molecular complex. *Phys. Rev. Lett.* **84,** 3454–3457 (2000).
22. De Raedt, H. D., Miyashita, S., Michielsen, K. & Machida, M. Dzyaloshinskii-Moriya interactions and adiabatic magnetization dynamics in molecular magnets. *Phys. Rev. B* **70,** 064401 (2004).
23. Chaboussant, G. *et al.* Mechanism of ground-state selection in the frustrated molecular spin cluster V_{15}. *Europhys. Lett.* **66,** 423–429 (2004).
24. Tarantul, A., Tsukerblat, B. & Müller, A. Static magnetization of V_{15} cluster at ultra-low temperatures: Precise estimation of antisymmetric exchange. *Inorg. Chem.* **46,** 161–169 (2007).
25. Tsukerblat, B., Tarantul, A. & Müller, A. Low temperature EPR spectra of the mesoscopic cluster V_{15}: The role of antisymmetric exchange. *J. Chem. Phys.* **125,** 054714 (2006).
26. Dzyaloshinsky, I. A thermodynamic theory of "weak" ferromagnetism of antiferromagnetics. *J. Phys. Chem. Solids* **4,** 241–255 (1958).
27. Moriya, T. Anisotropic superexchange interactions and weak ferromagnetism. *Phys. Rev.* **120,** 91–98 (1960).
28. Volkmer, D. *et al.* Towards nanodevices: Synthesis and characterization of the nanoporous surfactant-encapsulated keplerate (DODA)$_{40}$(NH$_4$)$_2$[(H$_2$O)$_n$ ⊂ Mo$_{132}$O$_{372}$(CH$_3$COO)$_{30}$(H$_2$O)$_{72}$]. *J. Am. Chem. Soc.* **122,** 1995–1998 (2000).
29. Prokof'ev, N. V. & Stamp, P. C. E. Quantum relaxation of magnetisation in magnetic particles. *J. Low Temp. Phys.* **104,** 143–210 (1996).
30. Hartmann-Boutron, F., Politi, P. & Villain, J. Tunneling and magnetic relaxation in mesoscopic molecules. *Int. J. Mod. Phys. B* **10,** 2577–2637 (1996).

METHODS

Sample synthesis. 0.04 g (0.0175 mmol) of freshly prepared brown $K_6\left[V_{15}^{IV}As_6^{III}O_{42}(H_2O)\right]\cdot 8H_2O$ obtained as reported[10] was dissolved in 20 ml of degassed water. After addition of 25 ml of a (degassed) trichloromethane solution of [DODA]Br (1.10 g/1.75 mmol) the reaction medium was stirred under inert atmosphere. The stirring was continued until the olive-brown coloured aqueous layer turned colourless and the corresponding colour appeared in the organic phase. The organic layer was then quickly separated, put into an EPR tube and frozen to liquid nitrogen temperature. All operations were done in an inert atmosphere.

Comparing Rabi frequencies. The frequency of the Rabi oscillations between two states 1 and 2 is given by[6-8,19]:

$$\Omega_R = \Omega_{R0}\,|\langle\varphi_1|S_+|\varphi_2\rangle| \qquad (2)$$

Here $\Omega_{R0} = 2g\mu_B B_1/h_{Planck} = 55.96B_1$ (MHz, mT) is the Rabi frequency of a spin 1/2, B_1 is the amplitude of the a.c. microwave fields, $g \approx 2$ the Landé factor, S_+ the ladder operator and $|\varphi_1\rangle$, $|\varphi_2\rangle$ the wavefunctions associated with these states. The probability of a transition, defined as $P = |\langle\varphi_1|S_+|\varphi_2\rangle|^2$, is directly connected with its Rabi frequency:

$$P = (\Omega_R/\Omega_{R0})^2 \qquad (3)$$

This allows one to evaluate the ratio (R) of the probabilities associated with two transitions (here the '3/2' and '1/2' types) from the measurement of their Rabi frequencies without the knowledge of their wavefunctions:

$$R = P_{3/2}/P_{1/2} = \left(\Omega_{R\,3/2}/\Omega_{R\,1/2}\right)^2 \qquad (4)$$

Using the values of the Rabi frequencies given in Fig. 3, one gets $R \approx (4.5/18.5)^2 \approx 5.9 \times 10^{-2}$. The time $T_{\pi/2}$, during which the excitation pulse is applied to induce a $\pi/2$ rotation, is by definition equal to $1/4\Omega_R$ (refs 6, 19), showing that equation (4) is equivalent to:

$$R = P_{3/2}/P_{1/2} = \left(T_{\pi/2,1/2}/T_{\pi/2,3/2}\right)^2 \qquad (5)$$

This gives another way to determine R. Using the $T_{\pi/2}$ values given in Fig. 4 legend, one gets $R \approx (16/64)^2 \approx 6.2 \times 10^{-2}$, which is very close to the first one and shows that the probability associated with the '1/2' type transition is much smaller than the one associated with '3/2'.

Rare-earth solid-state qubits

S. BERTAINA[1,2], S. GAMBARELLI[3], A. TKACHUK[4], I. N. KURKIN[5], B. MALKIN[5], A. STEPANOV[6] AND B. BARBARA[1]*

[1]Institut Néel, Département Nanosciences, CNRS, 25 Ave. des Martyrs, BP166, 38042 Grenoble Cedex 9, France
[2]Ecole Nationale Supérieure de Physique, INP de Grenoble, Minatec 3 parvis Louis Néel, BP 257, 38016 Grenoble Cedex 9, France
[3]Laboratoire de Chimie Inorganique et Biologie (UMR-E 3 CEA-UJF), DRFMC, CEA-Grenoble, 17 rue des Martyrs 38054 Grenoble Cedex 9, France
[4]S.I. Vavilov State Optical Institute, St Petersburg 199034, Russian Federation
[5]Kazan State University, Kazan 420008, Russian Federation
[6]Laboratoire de Matériaux et Microélectronique de Provence, Faculté St Jérôme, C142, 13397, Marseille Cedex 20, France
*e-mail: bernard.barbara@grenoble.cnrs.fr

Quantum bits (qubits) are the basic building blocks of any quantum computer. Superconducting qubits have been created with a top-down approach that integrates superconducting devices into macroscopic electrical circuits[1–3], and electron-spin qubits have been demonstrated in quantum dots[4–6]. The phase coherence time (τ_2) and the single qubit figure of merit (Q_M) of superconducting and electron-spin qubits are similar — at $\tau_2 \sim \mu s$ and $Q_M \sim 10–1{,}000$ below 100 mK — and it should be possible to scale up these systems, which is essential for the development of any useful quantum computer. Bottom-up approaches based on dilute ensembles of spins have achieved much larger values of τ_2 (up to tens of milliseconds; refs 7,8), but these systems cannot be scaled up, although some proposals for qubits based on two-dimensional nanostructures should be scalable[9–11]. Here we report that a new family of spin qubits based on rare-earth ions demonstrates values of τ_2 ($\sim$50 μs) and Q_M ($\sim$1,400) at 2.5 K, which suggests that rare-earth qubits may, in principle, be suitable for scalable quantum information processing at [4]He temperatures.

In general, a spin qubit state is a linear superposition of the two spin states of an electron $|\uparrow>$ and $|\downarrow>$. This means that the qubit can be represented as $|\psi_s> = \alpha|\uparrow> + \beta|\downarrow>$, where α and β are probability amplitudes, and $|\alpha|^2 + |\beta|^2 = 1$. When measuring this qubit, the probability of outcome $|\uparrow>$ (or $|\downarrow>$) is $|\alpha|^2$ (or $|\beta|^2$). In rare earth (RE) systems, the total spin, **S**, is no longer a good quantum number, because the spin-orbit coupling between **S** and the total orbital angular momentum, **L**, is larger than the coupling of **L** with the electric field gradient of environmental ionic charges (crystal field). The good quantum number is the total angular momentum, $\mathbf{J} = \mathbf{L} + \mathbf{S}$, which is coupled with the crystal field through **L**. The RE qubit states are therefore crystal-field states. In addition, RE elements often have isotopes with a nuclear spin, **I**, that has large hyperfine interactions with **J**, leading to electro-nuclear crystal-field states with wavefunctions $|\Psi_{en}>$ (see Methods).

Qubits based on these electro-nuclear states differ from typical spin qubits in several ways: (1) the crystal field strongly affects the Rabi frequencies that depend on the direction and the strength of applied magnetic fields and electric field gradients, and this could open up new possibilities for scaling; (2) the hyperfine interactions produce up to $3(2I + 1) - 2$ qubits per RE, all with slightly different resonance frequencies, which means that

it should be quite easy to selectively address them with superimposed (low) field pulses; (3) owing to their large magnetic moment ($\sim$10 μ_B), it should be simple to manipulate RE qubits; and (4) the single qubit figure of merit, Q_M, should be large enough to allow quantum information processing at [4]He temperatures (Q_M is the number of coherent single-qubit operations, defined as $\Omega_R\tau_2/\pi$, where Ω_R is the Rabi frequency; equivalently, it is the coherence time divided by half the Rabi period).

This work is an extension of previous research that explored the quantum tunnelling of the magnetization in Mn_{12}-ac and Ho:YLiF$_4$ (refs 12–14). Owing to the strong hyperfine interactions in the latter system, **J** tunnels simultaneously with **I** (electro-nuclear tunnelling). The system chosen to illustrate the concept of RE qubits consists of Er^{3+} ions (J = 15/2 and $g_J = 6/5$) diluted in a single crystalline matrix of $CaWO_4$, which is isomorphic with YLiF$_4$. The main reason for replacing YLiF$_4$ with $CaWO_4$ is to reduce the proportion of nuclear spins, which are an important source of decoherence[15] (the phenomenon by which a quantum system seems to be classical as a result of interactions with its environment).

Continuous-wave electron paramagnetic resonance (CW-EPR) measurements were first performed in Er^{3+}:$CaWO_4$. The transitions for the isotopes with I = 0 and I = 7/2 were observed at [4]He temperatures using a Bruker X-band spectrometer at 9.7 GHz. These transitions occur either between pure crystal-field levels (I = 0) or between electro-nuclear crystal-field sublevels (I = 7/2) (see Methods). In both cases, the observed line-width is small enough for the lifetime of the levels to be much larger than calculated periods of Rabi oscillations (weak decoherence). In order to observe these oscillations, a series of experiments was performed in pulsed-wave EPR (PW-EPR) mode. Eight transitions were observed (Fig. 1).

An example of the measured Rabi oscillations[16] is given in Fig. 2, for I = 0, where the z component of the magnetization, M_z, is plotted against time. It is possible to fit the data to

$$\langle M_z \rangle = M_{z(t=0)}e^{-t/\tau_R}\sin(\Omega_R t) \tag{1}$$

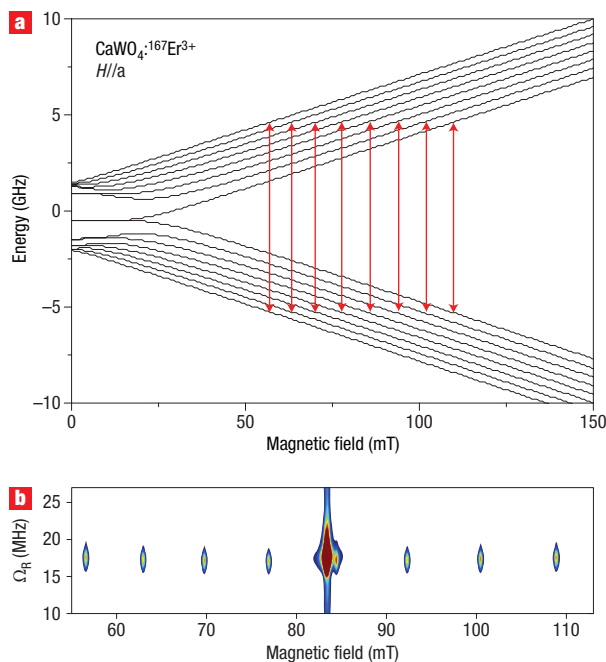using a single exponential damping parameter $\tau_R \sim 0.2$ μs (Ω_R having been previously obtained from a Fourier transform of the

Figure 1 Energy levels and Rabi frequencies for the erbium-doped RE system $^{167}Er^{3+}:CaWO_4$. a, Energy spectrum calculated for a magnetic field perpendicular to the c-axis. In the zero field, the spectrum contains 16 electro-nuclear states ($(2S + 1)(2I + 1)$ with $S = 1/2$ and $I = 7/2$) consisting of a singlet, 7 doublets and another singlet (nine sublevels). The fourth doublet, near the centre of the figure, is well separated from the other levels. When the Zeeman splitting caused by the magnetic field becomes larger than the hyperfine splitting, which sets the energy scale at zero field, the levels vary linearly with the magnetic field, which gives 8 states with effective spin $1/2$ and 8 states with effective spin $-1/2$. Each of these states is labelled by the nuclear spin projection, m_I, which increases from $-7/2$ for the two states at the centre of the figure to $+7/2$ for the lower- and upper-most states. EPR transitions between spins $\pm 1/2$ and $\Delta m_I = 0$ are represented by the vertical arrows. **b**, Rabi frequencies, measured versus static field $H//a$ and ac-field $\mu_0 h = 0.12$ mT//b, on a single crystal of $Er^{3+}:CaWO_4$ ($2 \times 2.5 \times 3$ mm^3, 10^{-5} atomic % Er). They show an intense central peak (for the isotopes $I = 0$) and 8 smaller peaks separated by $\Delta H \approx 6-8$ mT (for the isotope $I = 7/2$, $^{167}Er^{3+}$). Exact diagonalization of equation (4) (see Methods) permits accurate calculation of these frequencies (using the crystal-field and hyperfine constants only[30,32]); one finds $\Omega_R/2\pi = 17.546, 17.302, 17.166, 17.115, 17.137, 17.238, 17.394$ and 17.605 MHz. The colour scale shows the proportion of ions with Rabi frequency Ω_R at a given magnetic field (white < 80, blue = 80, red > 800 arbitrary units).
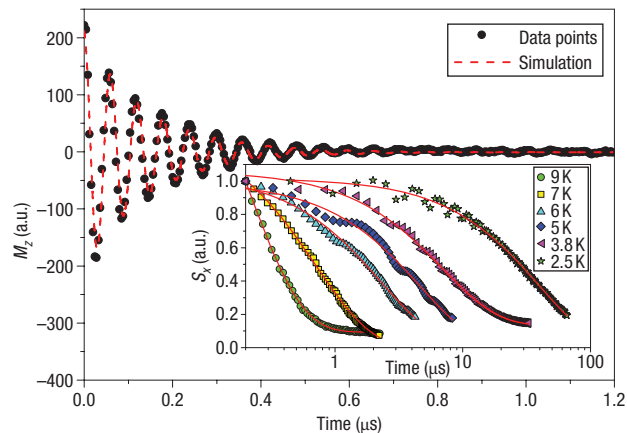

Figure 2 Rabi oscillations and coherence times. Rabi oscillations measured on $I = 0$ isotopes of the same single crystal for $\mu_0 H = 0.522$ T//c, $\mu_0 h = 0.15$ mT//b and $T = 3.5$ K. These oscillations are obtained by the application of a nutation pulse of length t followed, after a delay greater than τ_2 (permitting the transverses spin components to relax), by a $\pi/2 - \pi$ sequence. The resulting echo intensity is averaged over $\sim 10^3$ measurements, giving the z-component of the nutating magnetization at time t (M_z). The dashed line is a fit to equation (1) (see text) giving an exponential decay time $\tau_R = 0.2$ μs $\ll \tau_2 \approx 7$ μs (see Fig. 3). The inset shows the decay of the transverse spin component, S_x, obtained by a conventional spin-echo method at different temperatures, showing that the coherence time τ_2 reaches the 100 μs scale at ^{4}He temperatures. Weak superimposed oscillations come from the ESEEM effect (Electron Spin Echo Envelope Modulation)[34] produced by the super-hyperfine coupling with second neighbour W nuclear spins. One can verify that the oscillation frequency perfectly matches the W nucleus spin Larmor frequency in the applied field (small super hyperfine limit).

data). Other experiments performed at different microwave powers show that τ_R increases as the power decreases, and the number of Rabi oscillations, $N(c)$ (where c is the concentration of Er), remains nearly unchanged; that is, $N(c) \approx \tau_R(c)\Omega_R$, with $N(c) \sim 20$ in the example of Fig. 2. This increase of τ_R is always limited by τ_2 (Fig. 3). All of this suggests the phenomenological expression

$$1/\tau_R(c) \approx \Omega_R/N(c) + 1/\tau_2(c) \qquad (2)$$

where $\tau_R(c)$, $N(c)$ and $\tau_2(c)$ are concentration-dependent. Rabi oscillations are lost for $t \gg \tau_2$ in the low power limit where $\Omega_R \to 0$, and for $t \gg N(c)/\Omega_R$ in the large power limit where $\Omega_R \gg N(c)/\tau_2$. In the first case, τ_2 should be limited by RE

spin-diffusion because of long-range dipolar interactions, as in nuclear magnetic resonance. In the second case, the observed behaviour is characteristic of inhomogeneous nutation frequency. In fact, a weak random crystal field, responsible for the CW line-width[17,18], feeds into some distribution of the $|J,m_J,I,m_I\rangle$ coefficients, resulting in destructive interference of Rabi oscillations ($\Omega_R \propto \langle \phi_1, m_I | J_+ | \phi_2, m_I' \rangle$, see Methods), which go out of phase after a certain number of periods. However, the number of oscillations $N(c)$ depends on concentration, indicating that dipolar interactions must also be taken into account.

Recently, a model relying on the assumption that each spin experiences a stochastic field of mean-square amplitude β, oscillating at the resonance frequency ω, led to the expression

$$1/\tau_R = \beta\Omega_R + 1/2\tau_2 \qquad (3)$$

very similar to equation (2) (ref. 19). This linear dependence on Ω_R was tested on pure $S = 1/2$ spins in amorphous-SiO_2 containing E' centres where a concentration effect has also been obtained[20]. In the frame of the present study, the origin of the stochastic field should be related to both crystal-field distribution and dipolar interactions[21]. In order to check equations (2) and (3) more carefully, $1/\tau_R$ versus Ω_R is plotted for two different directions of the microwave field h (Fig. 3, inset; see also Fig. 4). The obtained curve is continuous, showing that the damping rate scales with the Rabi frequency (and not with the microwave field h when the dipole matrix elements are different) according to an S-shaped curve of, for example, the type $1/\tau_R = 1/\tau_2 f(\Omega_R\tau_2)$, with a progressive saturation at τ_2 when $\Omega_R \to 0$. The dependence

of Ω_R with the direction of the microwave field, h, is demonstrated in Fig. 4, where a simple rotation from $h//b$ to $h//c$ reduces the Rabi frequency by the factor $\Omega_{R//b}/\Omega_{R//c} \sim 6$. This ratio is slightly smaller than the one derived from the proportionality $\Omega_{R//b}/\Omega_{R//c} \approx g_{effb}/g_{effc} \approx 6.7$, because $\Omega_{R//b}$ drops in a few degrees from its maximum value $\Omega_{R//b} \sim 6.7\Omega_{R//c}$ to its minimum value $\sim \Omega_{R//c}$. A better agreement would simply require better angular accuracy in the crystal orientation.

Finally, RE qubits have large Q_M at ^{4}He temperatures and, in principle, they should be scalable. Indeed τ_2 increases with dilution and cooling (Fig. 2b); an extrapolation down to 1.5 K for a concentration of 10^{-6} atomic Er:CaWO$_4$ gives $Q_M \sim 10^4$, which is enough for quantum information processing. Moreover, RE qubits could in principle be selectively addressed and their couplings manipulated, according to variants of existing proposals and realizations[4–6,10,11]. As a matter of fact, they could be inserted in all kinds of matrices structured by lithography, including films, quantum dots or nanowires of semiconducting Si (ref. 22) or GaN (ref. 23), and coupled by controlled carrier injection through the gate voltage[24]. They could be addressed selectively by application of (1) local field pulses of amplitude <25 mT adding algebraically to the static field (this is limited to $n \leq 3(2I + 1) - 2$ qubits; Fig. 1), and (2) continuous electric field gradients for $n > 3(2I + 1) - 2$. A gradient of 10 mV $(nm)^{-2}$ is enough to modify the crystal-field parameters by $\sim 10\%$ in most matrices and therefore the resonance frequency. Interestingly, the $3(2I + 1) - 2$ Rabi oscillations of each ^{167}Er (Fig. 1) may also be used to implement Grover's algorithm[25] on single RE ions (this is a general property of electro-nuclear RE qubits with $I \neq 0$). Spin-state detection could follow schemes like those in refs 4 and 6, but alternative ways using the fast photoluminescent properties of RE (refs 22,23,26) might ultimately be better. Finally, instead of dots one might also use single molecules containing a RE ion[27].
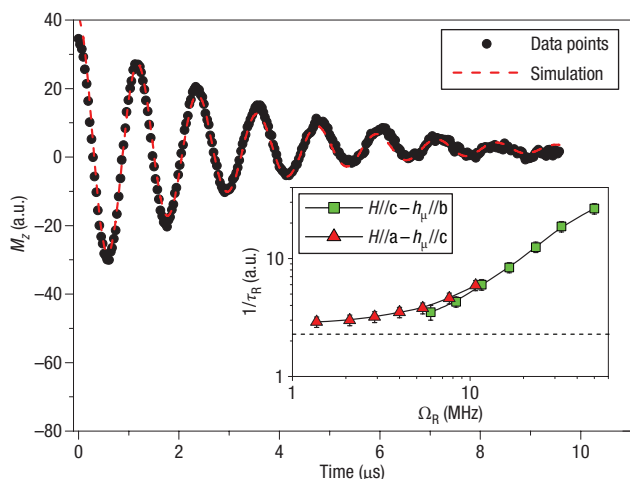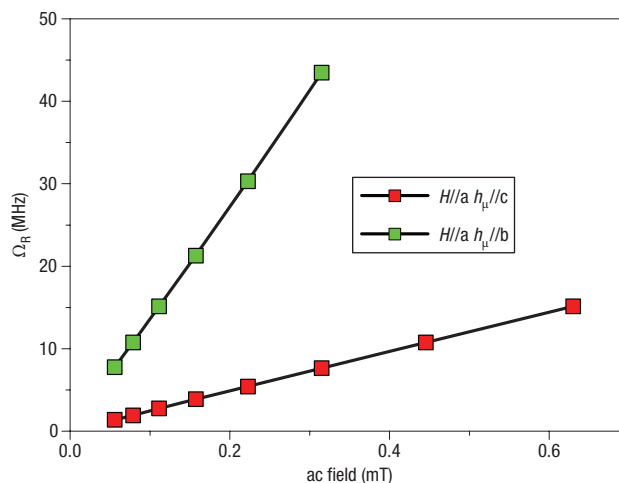

Figure 4 Maximum and minimum coupling of the microwave field to Er effective spins and direction-dependent Rabi frequencies. Rabi frequency, Ω_R, measured for two directions of the microwave field, h_μ, on a single crystal with atomic Er concentration of 5×10^{-4}. The ac field was calibrated by comparison with a coal sample. Owing to the 'easy' plane anisotropy (see Methods), the coupling between Er effective spins and the microwave field is maximum when the latter is in the easy plane (giving large Ω_R) and minimum when it is perpendicular to it (giving small Ω_R).

In conclusion, Rabi oscillations of the angular moment $J = 15/2$ of Er:CaWO$_4$ have been observed for the first time and analysed, evincing a new type of anisotropic electro-nuclear spin qubits. Isotopes with $I = 0$ give a single purely electronic Rabi frequency (single qubit, $\Delta M_J = \pm 1$), and the isotope $I = 7/2$ (^{167}Er) gives a set of eight electro-nuclear frequencies (eight qubits, $\Delta M_J = \pm 1$ and $\Delta M_I = 0$), which are addressed independently. Because the spin-orbit coupling, the magnetic moments and the hyperfine interactions are all large, it should be possible to couple and address selectively a large number of RE qubits using weak electric and magnetic fields. Furthermore, each RE ion could be used to implement Grover's algorithm. All this, together with large Q_M factors ($\sim 10^3$–10^4 between 2.5 and 1.5 K), suggests that RE qubits are good candidates for implementation of quantum computation at ^{4}He temperatures.

METHODS

CRYSTAL-FIELD BACKGROUND

The hamiltonian The single-ion hamiltonian for Er^{3+}:CaWO$_4$ (tetragonal space group I4$_1$/a and S$_4$ point symmetry[28]) contains crystal-field, hyperfine and Zeeman terms:

$$H_{CF} = \alpha_J B_2^0 O_2^0 + \beta_J (B_4^0 O_4^0 + B_4^4 O_4^4) + \gamma_J (B_6^0 O_6^0 + B_6^4 O_6^4 + B_6^{-4} O_6^{-4}) + A_J \mathbf{I} \cdot \mathbf{J} + g_J \mu_B \mu_0 \mathbf{J H} \quad (4)$$

The O_l^m are the Stevens' equivalent operators with the reduced matrix elements α_J, β_J, γ_J (ref. 29), and the B_l^m are the crystal-field parameters determined by high-resolution optical spectroscopy ($B_2^0 = 231$ cm^{-1}, $B_4^0 = -90$ cm^{-1}, $B_4^4 = \pm 852$ cm^{-1}, $B_6^0 = -0.6$ cm^{-1}, $B_6^4 = \pm 396$ cm^{-1} and $B_6^{-4} = \pm 75$ cm^{-1}; ref. 30).

Energy spectra and wavefunctions Exact diagonalization of the 16×16 matrix of equation (4) with $I = H = 0$ reveals an easy plane perpendicular to the c-axis with a doublet ground state of wavefunctions $|\phi_1>$ and $|\phi_2>$. This doublet, with effective spin 1/2 and anisotropic g_{eff} tensor ($g_{//} = 1.247$, $g_\perp = 8.38$; ref. 31), permits a single EPR transition ($\Delta m_J = \pm 1$), which can be

Figure 3 Changing the damping time with the microwave power. When the experiment in Fig. 2 is repeated with the microwave field reduced by a factor of 20, the period of the Rabi oscillations becomes longer (by the same factor of 20), but the number of periods remains of the order of 20 (up to 20 μs). The same fit as in Fig. 2 gives $\tau_R \sim 3$ μs, which is comparable with the $\tau_2 \sim 7$ μs obtained in spin-echo measurements under the same experimental conditions. The inset shows the damping rate of the Rabi oscillations, $1/\tau_R$, plotted against the Rabi frequency, Ω_R, for two directions of the microwave field. The continuity of the curve proves that $1/\tau_R$ depends on Ω_R only and tends to $1/\tau_2$ at low microwave power (dashed line).

observed on I = 0 isotopes (∼77%). The Rabi frequency is given by $\Omega_R = 2g_J\mu_B\langle\phi_1|J_\mu h_\mu|\phi_2\rangle/h \propto g_{eff}$, where h is Planck's constant. Natural Er also contains ^{167}Er with I = 7/2 (∼23%) and $A_J = -4.16 \times 10^{-3}$ cm^{-1} (−125 MHz) (ref. 32). In this case the 128 × 128 matrix leads to the energy spectrum of Fig. 1a. The degeneracy is completely removed by **H** and the new set of wavefunctions $|\Psi_{en}\rangle = \Sigma b_i|J,m_J,I,m_I\rangle$ on the space product $|L,S,J,m_J\rangle \otimes |I,m_I\rangle$ differs from $|\phi_1\rangle$ and $|\phi_2\rangle$ owing to the nuclear degrees of freedom. Figure 1 also shows that 3(2I + 1) − 2 EPR transitions are allowed, giving, for I = 7/2, eight transitions with conservation of I ($\Delta m_J = \pm 1$ and $\Delta m_I = 0$) and 14 transitions without ($\Delta I_J = \pm 1$ and $\Delta m_I = \pm 1$).

References

1. Leggett, A. J. Superconducting qubits — a major roadblock dissolved? *Science* **296**, 861–862 (2002).
2. Chiorescu, I. *et al.* Coherent dynamics of a flux qubit coupled to a harmonic oscillator. *Nature* **431**, 159–163 (2004).
3. Pashkin, A., Astafiev, O., Nakamura, Y. & Tsai, J. S. Demonstration of conditional gate operation using superconducting charge qubits. *Nature* **425**, 941–944 (2003).
4. Koppens, F. L. H. *et al.* Driven coherent oscillations at a single electron spin in a quantum dot. *Nature* **442**, 766–771 (2006).
5. Oosterkamp, T. H. *et al.* Microwave spectroscopy of a quantum-dot molecule. *Nature* **395**, 873–876 (1998).
6. Petta, J. R. *et al.* Coherent manipulation of coupled electron spins in semiconductor quantum dots. *Science* **309**, 2180–2184 (2005).
7. Tyryshkin, A. M., Lyon, S. A., Astashkin, A. V. & Raitsimring, A. M. Electron spin relaxation times in phosphorous donors in silicon. *Phys. Rev. B* **68**, 193207 (2003).
8. Mehring, M., Scherer, W. & Weidinger, A. Pseudo-entanglement of spin states in the multilevel ^{15}N@C$_{60}$ system. *Phys. Rev. Lett.* **93**, 206603 (2004).
9. Vandersypen, L. M. K. *et al.* Experimental realization of Shor's quantum factoring algorithm using nuclear magnetic resonance. *Nature* **414**, 883–887 (2001).
10. Loss, D. & DiVincenzo, D. P. Quantum computation with quantum dots. *Phys. Rev. A* **57**, 120–126 (1998).
11. Kane, B. E. A silicon based nuclear spin quantum computer. *Nature* **393**, 133–137 (1998).
12. Thomas, L. *et al.* Macroscopic quantum tunneling of the magnetization in a single crystal of nanomagnets. *Nature* **383**, 145–148 (1996)
13. Giraud, R., Wernsdorfer, W., Tkatchuk, A., Mailly, D. & Barbara, B. Nuclear spin driven quantum relaxation in LiY$_{0.998}$Ho$_{0.002}$ F$_4$. *Phys. Rev. Lett.* **87**, 057203 (2001).
14. Giraud, R., Tkachuk, A. M. & Barbara, B. Quantum dynamics of atomic magnets: co-tunneling and dipolar-biased-tunneling. *Phys. Rev. Lett.* **91**, 257204 (2003).
15. Stamp, P. C. E. & Tupitsyn, I. S. Coherence window in the dynamics of quantum nanomagnets. *Phys. Rev. B* **69**, 014401 (2004).
16. Rabi, I. I. Space quantization in a gyrating magnetic field. *Phys. Rev.* **51**, 652–655 (1937).
17. Shakurov, G. S. *et al.* Direct measurement of anti-crossings of the electron-nuclear energy levels in LiYF$_4$: Ho with submillimeter EPR spectroscopy. *Appl. Magn. Reson.* **28**, 251–265 (2005).
18. Kurkin, I. N. & Shekun, L. Ya. Paramagnetic resonance linewidths for impurity ions in scheelite single crystals. *Fiz. Tverd. Tela (Leningrad)* **9**, 444–448 (1967).
19. Shakhmuratov, R. N., Gelardi, F. M. & Cannas, M. Non-Bloch transients in solids: free induction decay and transient nutations. *Phys. Rev. Lett.* **79**, 2963–2966 (1997).
20. Agnello, S., Boscaino, R., Cannas, M., Gelardi, F. M. & Shakhmuratov, R. N. Transient nutation decay: the effect of field-modified dipolar interactions. *Phys. Rev. A* **59**, 4087–4090 (1999).
21. Prokof'ev, N. V. & Stamp, P. C. E. Theory of the spin-bath. *Rep. Prog. Phys.* **63**, 669–726 (2000).
22. Gallis, S. *et al.* Photoluminescence in erbium doped amorphous silicon oxycarbide thin films. *Appl. Phys. Lett.* **87**, 091901 (2005).
23. Hori, Y. *et al.* GaN quantum dots doped with Tb. *Appl. Phys. Lett.* **88**, 53102 (2006).
24. Ohno, H. *et al.* Electric-field control of ferromagnetism. *Nature* **408**, 944–946 (2000).
25. Leuenberger, M. N. & Loss, D. Grover algorithm for large nuclear spins in semiconductors. *Phys. Rev. B* **68**, 165317 (2003).
26. Tkachuk, A. M., Razumova, I. K., Malyshev, A. V. & Gapontsev, V. P. Population of lasing erbium in YLT : Er^{3+} crystals under upconversion cw LD pumping. *J. Luminescence* **94–95**, 317–320 (2001).
27. Ishikawa, N., Sugita, M., Ishikawa, T., Koshihara, S. & Kaisu, Y. Lanthanide double-decker complexes functioning as magnets at single-molecular level. *J. Am. Chem. Soc.* **125**, 8694–8695 (2003).
28. Zhang, Y., Holzwarth, N. A. W. & Williams, R. T. Electronic band structures of the scheelite materials CaMoO$_4$, CaWO$_4$, PbMoO$_4$, and PbWO$_4$. *Phys. Rev. B* **57**, 12738 (1998).
29. Stevens, K. W. H. The theory of paramagnetic relaxation. *Proc. Phys. Soc. London* **A65**, 209–217 (1952).
30. Bernal, E. G. Optical spectrum and magnetic properties of Er^{3+} in CaWO$_4$. *J. Chem. Phys.* **55**, 2538–2549 (1971).
31. Antipin, A. A. *et al.* Paramagnetic resonance and spin-lattice relaxation of Er^{3+} and Tb^{3+} ions in CaWO$_4$ crystal lattice. *Sov. Phys. Solid State* **10**, 468–474 (1968).
32. Abragam, A. & Bleaney, B. *Electron Paramagnetic Resonance of Transition Ions* (Clarendon Press, Oxford, 1970).
33. Rowan, L. G., Hahn, E. L. & Mims, W. B. Electronic spin-echo envelope modulation. *Phys. Rev. A* **137**, A61–A71 (1969).

Author contributions

A.T. provided the samples. S.B. and S.G. performed the experiments, and analysed and discussed them with A.S., I.K., B.M. and B.B. B.B. proposed this study and wrote the manuscript, which was commented on by all the authors.

Competing financial interests

The authors declare that they have no competing financial interests.

Reprints and permission information is available online at http://npg.nature.com/reprintsandpermissions/

pole, then α would be the co-latitude of the struts and the longitudinal angle between the struts would be 120°.

16. The presence of the factor of c^2 confirms that this is a relativistic effect. There is no swimming effect in the analogous Newtonian problem.

17. The fact that the swimming displacement per stroke is so small means that, strictly speaking, one should consider the swimming effect relative to the ordinary nonswimming geodesic motion of the

swimmer. However, the calculation that is presented is enough to show the existence of the effect that is surely also present in more complicated situations. Perhaps the most interesting case to consider would be a swimmer in a circular orbit, where the swimming effect could be used to gradually increase the radius of the orbit.

18. I thank J. Touma for infecting me with his interest in geometric phase and for bringing the articles of A. Shapere and F. Wilczek to my atten-

REPORTS

Coherent Quantum Dynamics of a Superconducting Flux Qubit

I. Chiorescu,[1]* Y. Nakamura,[1,2] C. J. P. M. Harmans,[1] J. E. Mooij[1]

We have observed coherent time evolution between two quantum states of a superconducting flux qubit comprising three Josephson junctions in a loop. The superposition of the two states carrying opposite macroscopic persistent currents is manipulated by resonant microwave pulses. Readout by means of switching-event measurement with an attached superconducting quantum interference device revealed quantum-state oscillations with high fidelity. Under strong microwave driving, it was possible to induce hundreds of coherent oscillations. Pulsed operations on this first sample yielded a relaxation time of 900 nanoseconds and a free-induction dephasing time of 20 nanoseconds. These results are promising for future solid-state quantum computing.

It is becoming clear that artificially fabricated solid-state devices of macroscopic size may, under certain conditions, behave as single quantum particles. We report on the controlled time-dependent quantum dynamics between two states of a micron-size superconducting ring containing billions of Cooper pairs (1). From a ground state in which all the Cooper pairs circulate in one direction, application of resonant microwave pulses can excite the system to a state where all pairs move oppositely, and make it oscillate coherently between these two states. Moreover, multiple pulses can be used to create quantum operation sequences. This is of strong fundamental interest because it allows experimental studies on decoherence mechanisms of the quantum behavior of a macroscopic-sized object. In addition, it is of great importance in the context of quantum computing (2) because these fabricated structures are attractive for a design that can be scaled up to large numbers of quantum bits or qubits (3).

Superconducting circuits with mesoscopic Josephson junctions are expected to behave according to the laws of quantum mechanics if they are separated sufficiently from external degrees of

[1]Quantum Transport Group, Department of Nano-Science, Delft University of Technology and Delft Institute for Micro Electronics and Submicron Technology (DIMES), Lorentzweg 1, 2628 CJ Delft, Netherlands. [2]NEC Fundamental Research Laboratories, 34 Miyukigaoka, Tsukuba, Ibaraki 305-8501, Japan.

*To whom correspondence should be addressed. E-mail: chiorescu@qt.tn.tudelft.nl

freedom, thereby reducing the decoherence. Quantum oscillations of a superconducting two-level system have been observed in the Cooper pair box qubit using the charge degree of freedom (4). An improved version of the Cooper pair box qubit showed that quantum oscillations with a high quality factor could be achieved (5). In addition, a qubit based on the phase degree of freedom in a Josephson junction was presented, consisting of a single, relatively large Josephson junction current-biased close to its critical current (6, 7).

Our flux qubit consists of three Josephson junctions arranged in a superconducting loop threaded by an externally applied magnetic flux near half a superconducting flux quantum $\Phi_0 = h/2e$ [(8); a one-junction flux qubit is described in (9)]. Varying the flux bias controls the energy level separation of this effectively two-level system. At half a flux quantum, the two lowest states are symmetric and antisymmetric superpositions of two classical states with clockwise and anticlockwise circulating currents. As shown by previous microwave spectroscopy studies, the qubit can be engineered such that the two lowest eigenstates are energetically well separated from the higher ones (10). Because the qubit is primarily biased by magnetic flux, it is relatively insensitive to the charge noise that is abundantly present in circuits of this kind.

The central part of the circuit, fabricated by electron beam lithography and shadow

evaporation of Al, shows the three in-line Josephson junctions together with the small loop defining the qubit in which the persistent current can flow in two directions, as shown by arrows (Fig. 1A). The area of the middle junction of the qubit is $\alpha = 0.8$ times the area of the two outer ones. This ratio, together with the charging energy $E_C = e^2/2C$ and the Josephson energy $E_J = hI_C/4\pi e$ of the outer junctions (where I_C and C are their critical current and capacitance, respectively), determines the qubit energy levels (Fig. 2A) as a function of the superconductor phase γ_q across the junctions (Fig. 1B). Close to $\gamma_q =$
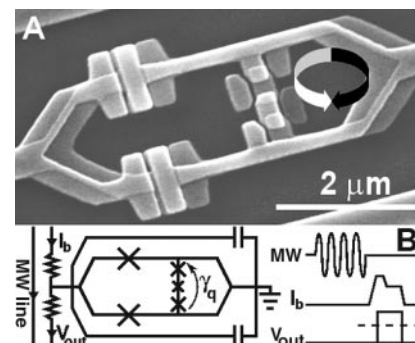

Fig. 1. (A) Scanning electron micrograph of a flux qubit (small loop with three Josephson junctions of critical current ~0.5 μA) and the attached SQUID (large loop with two big Josephson junctions of critical current ~2.2 μA). Evaporating Al from two different angles with an oxidation process between them gives the small overlapping regions (the Josephson junctions). The middle junction of the qubit is 0.8 times the area of the other two, and the ratio of qubit/SQUID areas is about 1:3. Arrows indicate the two directions of the persistent current in the qubit. The mutual qubit/SQUID inductance is $M \approx 9$ pH. (B) Schematic of the on-chip circuit; crosses represent the Josephson junctions. The SQUID is shunted by two capacitors (~5 pF each) to reduce the SQUID plasma frequency and biased through a resistor (~150 ohms) to avoid parasitic resonances in the leads. Symmetry of the circuit is introduced to suppress excitation of the SQUID from the qubit-control pulses. The MW line provides microwave current bursts inducing oscillating magnetic fields in the qubit loop. The current line provides the measuring pulse I_b and the voltage line allows the readout of the switching pulse V_{out}. The V_{out} signal is amplified, and a threshold discriminator (dashed line) detects the switching event at room temperature.

π, the loop behaves as a two-level system with an energy separation $E_{10} = E_1 - E_0$ of the eigenstates $|0\rangle$ and $|1\rangle$ described by the effective Hamiltonian $H = -\varepsilon\sigma_z/2 - \Delta\sigma_x/2$, where $\sigma_{z,x}$ are the Pauli spin matrices, Δ is the level repulsion, and $\varepsilon \approx I_p\Phi_0(\gamma_q - \pi)/\pi$ (where $I_p \approx 2\pi\alpha E_J/\Phi_0$ is the qubit maximum persistent current) (11).

The sample is enclosed in a gold-plated copper shielding box kept at cryogenic temperatures $T = 25$ mK ($k_BT \ll \Delta$). The qubit is initialized to the ground state simply by allowing it to relax. Coherent control of the qubit state is achieved by applying resonant microwave excitations on the microwave (MW) line (Fig. 1B), thereby inducing an oscillating magnetic field through the qubit loop. The qubit state evolves driven by a time-dependent term $(-\frac{1}{2})\varepsilon_{mw}\cos(2\pi Ft)\sigma_z$ in the Hamiltonian where F is the microwave frequency and ε_{mw} is the energy-modulation amplitude proportional to the microwave amplitude. This dynamic evolution is similar to that of spins in magnetic resonance. When the MW frequency equals the energy difference of the qubit, the qubit oscillates between the ground state and the excited state. This phenomenon is known as Rabi oscillation. The Rabi frequency depends linearly on the MW amplitude (12–14).

Readout is performed with an underdamped superconducting quantum interference device (SQUID) with a hysteretic current-voltage characteristic in direct contact with the qubit loop (Fig. 1A). The mutual coupling M is relatively large because of the shared kinetic and geometric inductances of the joint part enhancing the qubit signal. After performing the qubit operation, a bias current pulse I_b is applied to the SQUID (15). The I_b pulse consists of a short current pulse of length ~50 ns followed by a trailing plateau of ~500 ns (Fig. 1B). During the current pulse, the SQUID either switches to the gap voltage or stays at zero voltage. The pulse height and length are set to optimize the distinction of the switching probability between the two qubit states, which couple to the SQUID through the associated circulating currents. Because the readout electronics has a limited bandwidth of ~100 kHz, a voltage pulse of 50 ns is too short to be detected. For that reason the trailing plateau is added, with a current just above the retrapping current of the SQUID. The whole shape is adjusted for maximum readout fidelity. The switching probability is obtained by repeating the whole sequence of reequilibration, microwave control pulses, and readout typically 5000 times.
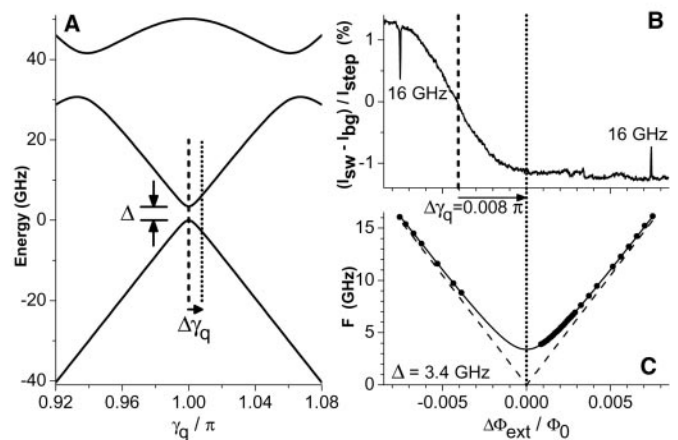
When the SQUID bias current is switched on, the circulating current in the SQUID changes. This circulating current, coupled to the qubit through the mutual inductance, changes the phase bias of the qubit by an estimated amount 0.01π. Consequently, the phase bias at which the quantum operations are performed is different from the phase bias at readout. This can be very useful because at the phase bias near π, where the qubit is least sensitive to flux noise, the expectation

values for the qubit circulating current are extremely small. The automatic phase bias shift can be used to operate near π and to perform readout at a bias with a good qubit signal (11). Care must be taken that the fast shift remains adiabatic and that the whole sequence is completed within the relaxation time.

The average SQUID switching current I_{sw} versus applied flux shows the change of the qubit ground-state circulating current (Fig. 2B). Here, the I_b pulse amplitude is adjusted such that the averaged switching probability is maintained at 50%. A step corresponding to the change of qubit circulating current was observed (around the dashed line). The relative variation of 2.5% of I_{sw} is in agreement with the estimation based on the qubit current I_p and the qubit-SQUID mutual inductance M.

The relevant two energy levels of the qubit were first examined by spectroscopic means. Before each readout, a long microwave pulse (1 μs) at a series of frequencies was applied to observe resonant absorption peaks/dips each time the qubit energy separation E_{10}—adjusted by changing the external flux—coincides with the MW frequency F (10). The dots in Fig. 2C are measured peak/dip positions, obtained by varying F, whereas the continuous line is a numerical fit produced by exact diagonalization (compare Fig. 2A) giving an energy gap $\Delta \approx$ 3.4 GHz. The curves in Fig. 2, B and C, are plotted against the change $\Delta\Phi_{ext}$ in external flux from the symmetry position indicated by the dotted line. In agreement with our numerical simulations, the step (Fig. 2B) is shifted away from the symmetry position of the energy spectrum (Fig. 2C) by a phase bias shift $\Delta\gamma_q \approx 2\pi(\Delta\Phi_{ext}/\Phi_0) \approx 0.008\pi$. The step reflects the external-flux dependence of the qubit circulating current at $I_b \approx I_{sw}$ (after the shift), whereas the spectrum reflects E_{01} at $I_b = 0$ (before the shift) (16).

Next, we used different MW pulse sequences to induce coherent quantum dynamics of the qubit in the time domain. For a given level separation E_{10}, a short resonant MW pulse of variable length with frequency $F = E_{10}$ was applied. Together with the MW amplitude, the pulse length defines the relative occupancy of the ground state and the excited state. The corresponding switching probability was measured with a fixed-bias current pulse amplitude. We obtained coherent Rabi oscillations of the qubit circulating current for a frequency $F = 6.6$ GHz and three different values of the MW power A (Fig. 3). The variation in switching probability is around 60%, indicating that the fidelity in a single readout is of that order. By varying A, we verified the linear dependence of the Rabi frequency on the MW amplitude, a key signature of the Rabi process (Fig. 3B). The oscillation pattern can be fitted to a damped sinusoid. For relatively strong driving (Rabi period below 10 ns), decay times τ_{Rabi} up to ~150 ns are obtained. This large decay time resulted in hundreds of coherent oscillations at large microwave power.

The Rabi scheme also allows the study of the state occupancy relaxation. This can be done by applying a coherent π pulse for full rotation of the qubit into the excited state and varying the delay time before readout. Experiments performed at $F = 5.71$ GHz gave an exponential decay with relaxation time $\tau_{relax} \approx 900$ ns.

As a next step we measured the undriven, free-evolution dephasing time τ_φ by performing a Ramsey interference experiment (17) as follows. Two $\pi/2$ pulses, whose length is determined from the Rabi precession presented above, are applied to the qubit. The first pulse creates a superposition of the $|0\rangle$ and $|1\rangle$ states. If the microwave frequency is detuned by $\delta F = E_{10} - F$ away from resonance, the superposition phase increases with a rate

Fig. 2. (**A**) Calculated energy diagram for the three-junction qubit, for $E_J/E_C = 35$, $E_C = 7.4$ GHz, and $\alpha = 0.8$ (11). $\Delta\gamma_q$ indicates the phase shift induced by the SQUID bias current. (**B**) Ground-state transition step: The sinusoidal background modulation of the SQUID (I_{bg}) is subtracted from the I_b pulse amplitude corresponding to 50% switching probability (I_{sw}) and then normalized to I_{step}, the middle value (at the dashed line). A sharp peak and dip are induced by a long (1 μs) MW radiation burst at 16 GHz, allowing the symmetry point to be found (midpoint of the peak/dip positions, dotted line). Data show I_{sw} versus $\Delta\Phi_{ext}$, the deviation in external flux from this point. The transition step is displaced from this point by $\Delta\gamma_q/2\pi$. (**C**) Frequency of the resonant peaks/dips (dots) versus $\Delta\Phi_{ext}$; the continuous line is a numerical fit with the same parameters as in (A) leading to a value of $\Delta = 3.4$ GHz, whereas the dashed line depicts the case $\Delta = 0$.

$2\pi\delta F$, in the frame rotating with the MW frequency F. After a varying delay time, we apply another $\pi/2$ pulse to measure the final $|0\rangle$ and $|1\rangle$ state occupancy via the switching probability. The readout shows Ramsey fringes with a period $1/\delta F$, as in Fig. 4A, where $E_{10} = 5.71$ GHz and $\delta F = 220$ MHz. The dots represent experimental data, whereas the continuous line is an exponentially damped sinusoidal fitting curve, yielding a free-evolution dephasing time $\tau_\varphi \approx 20$ ns. Note that the oscillation period of 4.5 ns agrees well with $1/\delta F$.

Additional information on the spectral properties of the decohering fluctuations can be obtained with a modified Ramsey experiment. By inserting a π pulse between the two $\pi/2$ pulses (Fig. 4B), we obtain a spin-echo pulse configuration. The role of the π pulse is to reverse the noise-driven diffusion of the qubit phase at the midpoint in time of the free evolution. Dephasing due to fluctuations of lower frequencies should be cancelled by their opposite influence before and after the π pulse (18). Spin-echo oscillations (Fig. 4B) are taken under the same conditions as the Ramsey fringes, but are here recorded as a function of the π pulse position. The period ($\sim$2.3 ns) is half that of the Ramsey interference. We measured the decay of the maximum spin-echo signal (i.e., with the π pulse in the center) versus the delay time between the two $\pi/2$ pulses. The data can be fitted to a half-Gaussian (not shown) with a decay time $\tau_{echo} \approx 30$ ns.

We conclude that with the present device and setup, the dephasing time $\tau_\varphi \approx 20$ ns, as measured with the Ramsey pulses, is much shorter than the relaxation time $\tau_{relax} \approx 900$ ns. Dephasing is probably caused by a variation in time of the qubit energy splitting, attributable to external or internal noise. A likely source is external flux noise, which can be reduced in the future. The present qubit could not be operated at the symmetry point $\gamma_q = \pi$ where the influence of flux noise is minimal (5), presumably as the result of an accidentally close SQUID resonance (19). Other possible noise sources are thermal, charge, critical current, and spin fluctuations. From estimations of the Johnson noise in the bias circuit (20, 21), we find a contribution that is several orders of magnitude weaker.

For strong driving, Rabi oscillations persisted for times much longer than τ_φ. This constitutes no inconsistency. The dependence of the Rabi period on the detuning, due to fluctuations of the qubit energy E_{10}, is weak when the Rabi period is short. The fact that coherence is only marginally improved by the π pulse in the spin-echo experiment seems to indicate the presence of noise at frequencies beyond 10 MHz. Further analysis and additional measurements are needed.

These first results on the coherent time evolution of a flux qubit are very promising. The already high fidelity of qubit excitation and readout can no doubt be improved. Quite likely it is also possible to reduce the dephasing rate. Taken together, these results establish the superconducting flux qubit as an attractive candidate for solid-state quantum computing.

References and Notes

1. A. J. Leggett, A. Garg, *Phys. Rev. Lett.* **54**, 857 (1985).
2. M. A. Nielsen, I. L. Chuang, *Quantum Computation and Quantum Information* (Cambridge Univ. Press, Cambridge, 2000).
3. Y. Makhlin *et al.*, *Rev. Mod. Phys.* **73**, 357 (2001).
4. Y. Nakamura *et al.*, *Nature* **398**, 786 (1999).
5. D. Vion *et al.*, *Science* **296**, 886 (2002).
6. Y. Yu *et al.*, *Science* **296**, 889 (2002).
7. J. M. Martinis *et al.*, *Phys. Rev. Lett.* **89**, 117901 (2002).
8. J. E. Mooij *et al.*, *Science* **285**, 1036 (1999).
9. J. R. Friedman *et al.*, *Nature* **406**, 43 (2000).
10. C. H. van der Wal *et al.*, *Science* **290**, 773 (2000).
11. The two opposite persistent current states, depicted by arrows in Fig. 1A, describe the basis $\{|\uparrow\rangle, |\downarrow\rangle\}$ of Pauli spin matrices. Using the notation $\tan 2\theta = \Delta/\varepsilon$, the qubit eigenstates can be written as $|0\rangle = \cos\theta|\uparrow\rangle + \sin\theta|\downarrow\rangle$ and $|1\rangle = -\sin\theta|\uparrow\rangle + \cos\theta|\downarrow\rangle$ and the expectation values of the corresponding circulating currents as $I_{q0,1} = \pm I_p \cos 2\theta$.
12. I. I. Rabi, *Phys. Rev.* **51**, 652 (1937).
13. M. Grifoni, P. Hänggi, *Phys. Rep.* **304**, 229 (1998).
14. In the frame rotating at the MW frequency $F = E_{10}$, the Rabi precession is around the x axis with a frequency $(\varepsilon_{mw} \sin 2\theta)/h$ [with θ as in (11)].
15. During the qubit initialization and control, the SQUID bias current is set to zero and, as a result of the SQUID symmetry, the qubit is decoupled from the external current noise to first order. At $I_b = 0$, small external noise current flows equally in the two branches of the SQUID even in the presence of the circulating current in the SQUID. See also (21).
16. A part of the energy spectrum is missing, because the readout is not efficient around the step and thus the spectroscopy signal is weak.
17. N. F. Ramsey, *Phys. Rev.* **78**, 695 (1950).
18. E. L. Hahn, *Phys. Rev.* **80**, 580 (1950).
19. In the present device, $\Delta \approx 3.4$ GHz was rather close to the SQUID plasma frequency designed to be $\sim$2 GHz (at $I_b \approx I_{sw}$). This could be a possible explanation for the absence of coherent oscillations for $F = \Delta$.
20. Lin Tian, S. Lloyd, T. P. Orlando, *Phys. Rev. B* **65**, 144516 (2002).
21. C. H. van der Wal, F. K. Wilhelm, C. J. P. M. Harmans, J. E. Mooij, *Eur. Phys. J. B* **31**, 111 (2003).
22. We thank R. N. Schouten, J. B. Majer, A. Lupascu, and K. Semba for experimental help and discussion; D. Esteve and C. Urbina for valuable input; and D. Vion, A. Aassime, C. H. van der Wal, A. C. J. ter Haar, T. Orlando, S. Lloyd, M. Grifoni, F. K. Wilhelm, L. Vandersypen, and P. C. E. Stamp for fruitful discussions. Supported by the Dutch Foundation for Fundamental Research on Matter (FOM), the European Union SQUBIT project, and the U.S. Army Research Office (grant DAAD 19-00-1-0548).

Fig. 3. (A) Rabi oscillations for a resonant frequency $F = E_{10} = 6.6$ GHz and three different microwave powers $A = 0$, -6, and -12 dBm, where A is the nominal microwave power applied at room temperature. The data are well fitted by exponentially damped sinusoidal oscillations. The resulting decay time is $\sim$150 ns for all powers. **(B)** Linear dependence of the Rabi frequency on the microwave amplitude, expressed as $10^{A/20}$. The slope is in agreement with estimations based on sample design.
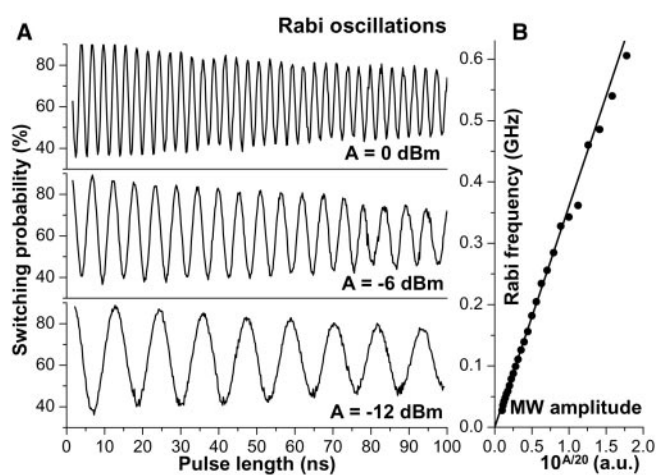

Fig. 4. (A) Ramsey interference: The measured switching probability (dots) is plotted against the time between the two $\pi/2$ pulses. The continuous line is a fit by exponentially damped oscillations with a decay time of 20 ns. The Ramsey interference period of 4.5 ns agrees with the inverse of the detuning from resonance, 220 MHz. The resonant frequency is 5.71 GHz and microwave power $A = 0$ dBm. **(B)** Spin-echo experiment: switching probability versus position of the π pulse between two $\pi/2$ pulses. The period of $\sim$2.3 ns corresponds well to half the inverse of the detuning. The width and timing of microwave pulses in the MW line are shown in each graph. The readout pulse in the bias line immediately follows the last $\pi/2$ pulse (see Fig. 1B).
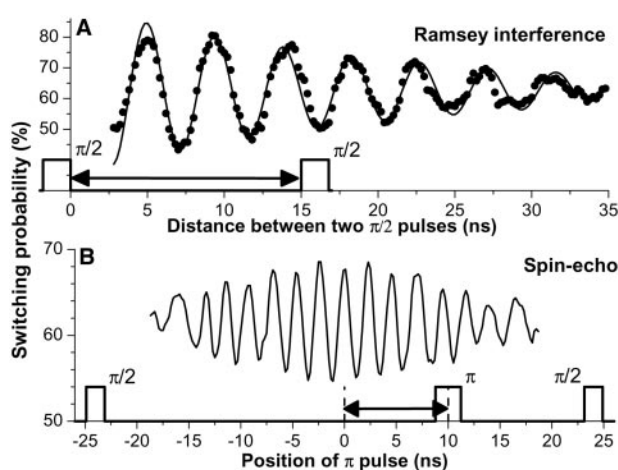
ARTICLES

Driven coherent oscillations of a single electron spin in a quantum dot

F. H. L. Koppens[1], C. Buizert[1], K. J. Tielrooij[1], I. T. Vink[1], K. C. Nowack[1], T. Meunier[1], L. P. Kouwenhoven[1] & L. M. K. Vandersypen[1]

The ability to control the quantum state of a single electron spin in a quantum dot is at the heart of recent developments towards a scalable spin-based quantum computer. In combination with the recently demonstrated controlled exchange gate between two neighbouring spins, driven coherent single spin rotations would permit universal quantum operations. Here, we report the experimental realization of single electron spin rotations in a double quantum dot. First, we apply a continuous-wave oscillating magnetic field, generated on-chip, and observe electron spin resonance in spin-dependent transport measurements through the two dots. Next, we coherently control the quantum state of the electron spin by applying short bursts of the oscillating magnetic field and observe about eight oscillations of the spin state (so-called Rabi oscillations) during a microsecond burst. These results demonstrate the feasibility of operating single-electron spins in a quantum dot as quantum bits.

The use of quantum mechanical superposition states and entanglement in a computer can theoretically solve important mathematical and physical problems much faster than classical computers[1,2]. However, the realization of such a quantum computer represents a formidable challenge, because it requires fast and precise control of fragile quantum states. The prospects for accurate quantum control in a scalable system are thus being explored in a rich variety of physical systems, ranging from nuclear magnetic resonance and ion traps to superconducting devices[3].

Electron spin states were identified early on as an attractive realization of a quantum bit[4], because they are relatively robust against decoherence (uncontrolled interactions with the environment). Advances in the field of semiconductor quantum dots have made this system very fruitful as a host for the electron spin. Since Loss and DiVincenzo's proposal[5] on electron spin qubits in quantum dots in 1998, many of the elements necessary for quantum computation have been realized experimentally. It is now routine to isolate with certainty a single electron in each of two coupled quantum dots[6–9]. The spin of this electron can be reliably initialized to the ground state, spin-up, via optical pumping[10] or by thermal equilibration at sufficiently low temperatures and strong static magnetic fields (for example, $T = 100$ mK and $B_{ext} = 1$ T). The spin states are also very long-lived, with relaxation times of the order of milliseconds[11–13]. Furthermore, a lower bound on the spin coherence time exceeding 1 μs was established, using spin-echo techniques on a two-electron system[14]. These long relaxation and coherence times are possible in part because the magnetic moment of a single electron spin is so weak. On the other hand, this property makes read-out and manipulation of single spins particularly challenging. By combining spin-to-charge conversion with real-time single-charge detection[15–17], it has nevertheless been possible to accomplish single-shot read-out of spin states in a quantum dot[13,18].

The next major achievement was the observation of the coherent exchange of two electron spins in a double dot system, controlled by fast electrical switching of the tunnel coupling between the two quantum dots[14]. Finally, free evolution of a single electron spin about

a static magnetic field (Larmor precession) has been observed, via optical pump–probe experiments[19,20]. The only missing ingredient for universal quantum computation with spins in dots remained the demonstration of driven coherent spin rotations (Rabi oscillations) of a single electron spin.

The most commonly used technique for inducing spin flips is electron spin resonance (ESR)[21]. ESR is the physical process whereby electron spins are rotated by an oscillating magnetic field B_{ac} (with frequency f_{ac}) that is resonant with the spin precession frequency in an external magnetic field B_{ext}, oriented perpendicularly to B_{ac} ($hf_{ac} = g\mu_B B_{ext}$, where μ_B is the Bohr magneton and g the electron spin g-factor). Magnetic resonance of a single electron spin in a solid has been reported in a few specific cases[22–24], but has never been realized in semiconductor quantum dots. Detecting ESR in a single quantum dot is conceptually simple[25], but experimentally difficult to realize, as it requires a strong, high-frequency magnetic field at low temperature, while accompanying alternating electric fields must be minimized. Alternative schemes for driven rotations of a spin in a dot have been proposed, based on optical excitation[26] or electrical control[27–29], but this is perhaps even more challenging and has not been accomplished either.

Here, we demonstrate the ability to control the spin state of a single electron confined in a double quantum dot via ESR. In a double dot system, spin-flips can be detected through the transition of an electron from one dot to the other[30,31] rather than between a dot and a reservoir, as would be the case for a single dot. This has the advantage that there is no need for the electron spin Zeeman splitting (used in a single dot for spin-selective tunnelling) to exceed the temperature of the electron reservoirs (~100 mK; the phonon temperature was ~40 mK). The experiment can thus be performed at a smaller static magnetic field, and consequently with lower, technically less demanding, excitation frequencies. Furthermore, by applying a large bias voltage across the double dot, the spin detection can be made much less sensitive to electric fields than is possible in the single-dot case (electric fields can cause photon-assisted tunnelling; see Supplementary Discussion). Finally, in a double dot, single-spin

[1]Kavli Institute of NanoScience, Delft University of Technology, PO Box 5046, 2600 GA, Delft, The Netherlands.

operations can in future experiments be combined with two-qubit operations to realize universal quantum gates[5], and with spin read-out to demonstrate entanglement[32,33].

Device and ESR detection concept

Two coupled semiconductor quantum dots are defined by surface gates (Fig. 1a) on top of a two-dimensional electron gas. By applying the appropriate negative voltages to the gates the dots can be tuned to the few-electron regime[8]. The oscillating magnetic field that drives the spin transitions is generated by applying a radio-frequency (RF) signal to an on-chip coplanar stripline (CPS) which is terminated in a narrow wire, positioned near the dots and separated from the surface gates by a 100-nm-thick dielectric (Fig. 1b). The current through the wire generates an oscillating magnetic field B_{ac} at the dots, perpendicular to the static external field B_{ext} and slightly stronger in the left dot than in the right dot (see Supplementary Fig. S1).

To detect the ESR-induced spin rotations, we use electrical transport measurements through the two dots in series in the spin blockade regime where current flow depends on the relative spin state of the electrons in the two dots[30,34]. In brief, the device is operated so that current is blocked owing to spin blockade, but this blockade is lifted if the ESR condition ($hf_{ac} = g\mu_B B_{ext}$) is satisfied.
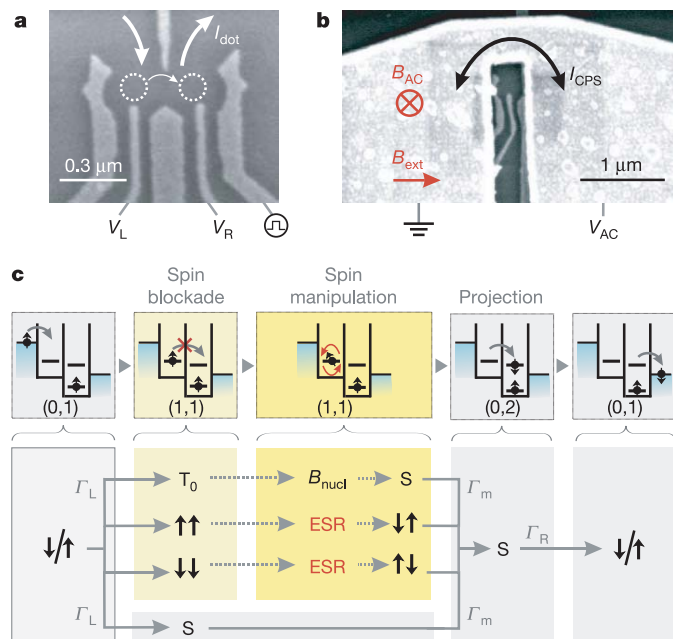

Figure 1 | Device and ESR detection scheme. a, Scanning electron microscope (SEM) image of a device with the same gate pattern as used in the experiment. The Ti/Au gates are deposited on top of a GaAs/AlGaAs heterostructure containing a two-dimensional electron gas 90 nm below the surface. White arrows indicate current flow through the two coupled dots (dotted circles). The right side gate is fitted with a homemade bias-tee (rise time 150 ps) to allow fast pulsing of the dot levels. **b,** SEM image of a device similar to the one used in the experiment. The termination of the coplanar stripline is visible on top of the gates. The gold stripline has a thickness of 400 nm and is designed to have a 50 Ω characteristic impedance, Z_0, up to the shorted termination. It is separated from the gate electrodes by a 100-nm-thick dielectric (Calixerene)[50]. **c,** Diagrams illustrating the transport cycle in the spin blockade regime. This cycle can be described via the occupations (m,n) of the left and right dots as $(0,1) \rightarrow (1,1) \rightarrow (0,2) \rightarrow (0,1)$. When an electron enters the left dot (with rate Γ_L) starting from (0,1), the two-electron system that is formed can be either a singlet S(1,1) or a triplet T(1,1). From S(1,1), further current flow is possible via a transition to S(0,2) (with rate Γ_m). When the system is in T(1,1), current is blocked unless this state is coupled to S(1,1). For T_0, this coupling is provided by the inhomogeneous nuclear field ΔB_N. For T_+ or T_-, ESR causes a transition to ↑↓ or ↓↑, which contains a S(1,1) component and a T_0 component (which is in turn coupled to S(1,1) by the nuclear field).

This spin blockade regime is accessed by tuning the gate voltages such that one electron always resides in the right dot, and a second electron can tunnel from the left reservoir to the left dot (Fig. 1c and Supplementary Fig. S2). If this electron forms a double-dot singlet state with the electron in the right dot (S = ↑↓ − ↓↑; normalization omitted for brevity), it is possible for the left electron to move to the right dot, and then to the right lead (leaving behind an electron in the right dot with spin ↑ or spin ↓), since the right dot singlet state is energetically accessible. If, however, the two electrons form a double-dot triplet state, the left electron cannot move to the right dot because the right dot's triplet state is much higher in energy. The electron also cannot move back to the lead and therefore further current flow is blocked as soon as any of the (double-dot) triplet states is formed.

Role of the nuclear spin bath for ESR detection

In fact, the situation is more complex, because each of the two spins experiences a randomly oriented and fluctuating effective nuclear field of ~1–3 mT (refs 35, 36). This nuclear field, B_N, arises from the hyperfine interaction of the electron spins with the Ga and As nuclear spins in the host material, and is in general different in the two dots, with a difference of ΔB_N. At zero external field and for sufficiently small double dot singlet–triplet splitting (see Supplementary Fig. S2d), the inhomogeneous component of the nuclear field causes all three triplet states (T_0, T_+ and T_-) to be admixed with the singlet S (for example, $T_0 =$ ↑↓ + ↓↑ evolves into S = ↑↓− ↓↑ due to $\Delta B_{N,z}$, and $T_+ =$ ↑↑ and $T_- =$ ↓↓ evolve into S owing to $\Delta B_{N,x}$). As a result, spin blockade is lifted. For $B_{ext} \gg \sqrt{\langle B_N^2 \rangle}$, however, the T_+ and T_- states split off in energy, which makes hyperfine-induced admixing between $T_\pm$ and S ineffective (T_0 and S remain admixed; see Fig. 2a). Here spin blockade does occur, whenever a state with parallel spins (↑↑ or ↓↓) becomes occupied.

ESR is then detected as follows (see Fig. 1c). An oscillating magnetic field resonant with the Zeeman splitting can flip the spin in the left or the right dot. Starting from ↑↑ or ↓↓, the spin state then changes to ↑↓ (or ↓↑). If both spins are flipped, transitions occur between ↑↑ and ↓↓ via the intermediate state $\frac{↑±↓}{\sqrt{2}}\frac{↑±↓}{\sqrt{2}}$. In both cases, states with anti-parallel spins ($S_z = 0$) are created owing to ESR. Expressed in the singlet-triplet measurement basis, ↑↓ or ↓↑ is a superposition of the T_0 and S state (↑↓ = T_0 + S). For the singlet component of this state, the left electron can transition immediately to the right dot and from there to the right lead. The T_0 component first evolves into a singlet due to the nuclear field and then the left electron can move to the right dot as well. Thus whenever the spins are anti-parallel, one electron charge moves through the dots. If such transitions from parallel to anti-parallel spins are induced repeatedly at a sufficiently high rate, a measurable current flows through the two dots.

ESR spectroscopy

The resonant ESR response is clearly observed in the transport measurements as a function of magnetic field (Fig. 2a, b), where satellite peaks develop at the resonant field $B_{ext} = \pm hf_{ac}/g\mu_B$ when the RF source is turned on (the zero-field peak arises from the inhomogeneous nuclear field, which admixes all the triplets with the singlet[36,37]). The key signature of ESR is the linear dependence of the satellite peak location on the RF frequency, which is clearly seen in the data of Fig. 2c, where the RF frequency is varied from 10 to 750 MHz. From a linear fit through the top of the peaks we obtain a g-factor with modulus 0.35 ± 0.01, which lies within the range of reported values for confined electron spins in GaAs quantum dots[11,38–40]. We also verified explicitly that the resonance we observe is magnetic in origin and not caused by the electric field that the CPS generates as well; negligible response was observed when RF power is applied to the right side gate, generating mostly a RF electric field (see Supplementary Fig. S3).

The amplitude of the peaks in Fig. 2b increases linearly with RF power (~B_{ac}^2) before saturation occurs, as predicted[25] (Fig. 2b, inset). The ESR satellite peak is expected to be broadened by either the
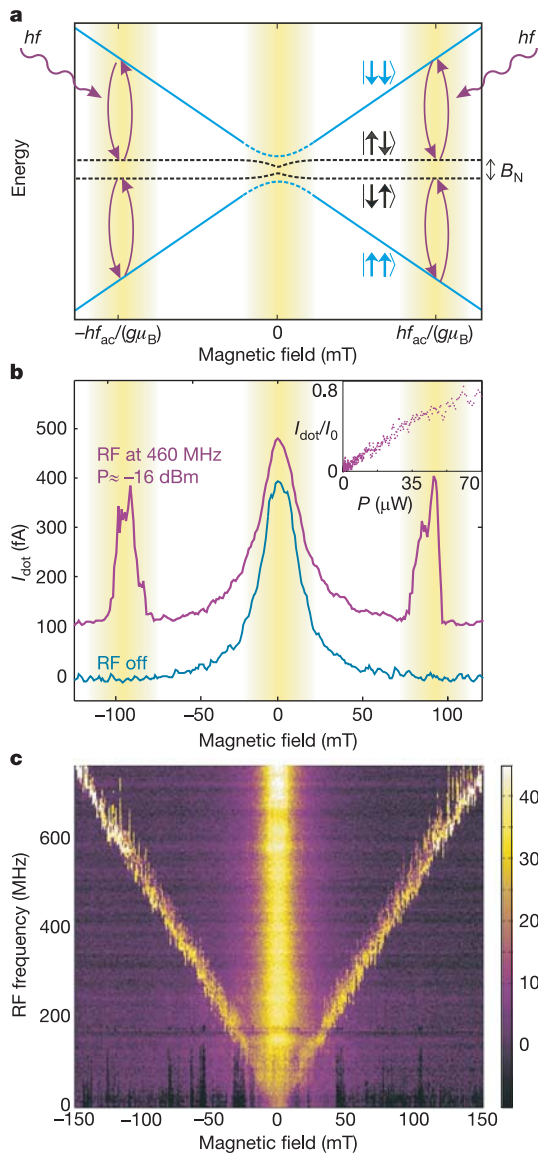
Figure 2 | ESR spin state spectroscopy. a, Energy diagram showing the relevant eigenstates of two electron spins in a double-dot, subject to an external magnetic field and nuclear fields. Because the nuclear field is generally inhomogeneous, the Zeeman energy is different in the two dots and results therefore in a different energy for ↑↓ and ↓↑. ESR turns the spin states ↑↑ and ↓↓ into ↑↓ or ↓↑, depending on the nuclear fields in the two dots. The yellow bands denote the ranges in B_{ext} where spin blockade is lifted (by the nuclear field or ESR) and current will flow through the dots. **b**, Current measured through the double-dot in the spin blockade regime, with (red trace, offset by 100 fA for clarity) and without (blue trace) a RF magnetic field. Satellite peaks appear as the external magnetic field is swept through the spin resonance condition. Each measurement point is averaged for one second, and is therefore expected to represent an average response over many nuclear configurations. The RF power P applied to the CPS is estimated from the power applied to the coax line and the attenuation in the lines. Inset, satellite peak height versus RF power ($f = 408$ MHz, $B_{ext} = 70$ mT, taken at slightly different gate voltage settings). The current is normalized to the current at $B_{ext} = 0$ ($= I_0$). Unwanted electric field effects are reduced by applying a compensating signal to the right side gate with opposite phase as the signal on the stripline (see Supplementary Fig. S4). This allowed us to obtain this curve up to relatively high RF powers. **c**, Current through the dots when sweeping the RF frequency and stepping the magnetic field. The ESR satellite peak is already visible at a small magnetic field of 20 mT and RF excitation of 100 MHz, and its location evolves linearly in field when increasing the frequency. For higher frequencies the satellite peak is broadened asymmetrically for certain sweeps, visible as vertical stripes. This broadening is time dependent, hysteretic in sweep direction, and changes with the dot level alignment. The horizontal line at 180 MHz is due to a resonance in the transmission line inside the dilution refrigerator.

excitation amplitude B_{ac} or incoherent processes, like cotunnelling, inelastic transitions (to the S(0,2) state) or the statistical fluctuations in the nuclear field, whichever of the four has the largest contribution. No dependence of the width on RF power was found within the experimentally accessible range ($B_{ac} < 2$ mT). Furthermore, we suspect that the broadening is not dominated by cotunnelling or inelastic transitions because the corresponding rates are smaller than the observed broadening (see Supplementary Figs S4b and S2d). The observed ESR peaks are steeper on the flanks and broader than expected from the nuclear field fluctuations. In many cases, the peak width and position are even hysteretic in the sweep direction, suggesting that the resonance condition is shifted during the field sweep. We speculate that dynamic nuclear polarization due to feedback of the electron transport on the nuclear spins plays a central part here[37].

Coherent Rabi oscillations

Following the observation of magnetically induced spin flips, we next test whether we can also coherently rotate the spin by applying RF bursts with variable length. In contrast to the continuous-wave experiment, where detection and spin rotation occur at the same time, we pulse the system into Coulomb blockade during the spin manipulation. This eliminates decoherence induced by tunnel events from the left to the right dot during the spin rotations. The experiment consists of three stages (Fig. 3): initialization through spin blockade in a statistical mixture of ↑↑ and ↓↓, manipulation by a RF burst in Coulomb blockade, and detection by pulsing back for projection (onto S(0,2)) and tunnelling to the lead. When one of the electrons is rotated over $(2n + 1)\pi$ (with integer n), the two-electron state evolves to ↑↓ (or ↓↑), giving a maximum contribution to the current (as before, when the two spins are anti-parallel, one electron charge moves through the dots). However, no electron flow is expected after rotations of $2\pi n$, where one would find two parallel spins in the two dots after the RF burst.

We observe that the dot current oscillates periodically with the RF burst length (Fig. 4). This oscillation indicates that we performed driven, coherent electron spin rotations, or Rabi oscillations. A key characteristic of the Rabi process is a linear dependence of the Rabi frequency on the RF burst amplitude, B_{ac} ($f_{Rabi} = g\mu_B B_1/h$ with $B_1 = B_{ac}/2$ due to the rotating wave approximation). We verify this by extracting the Rabi frequency from a fit of the current oscillations of Fig. 4b with a sinusoid, which gives the expected linear behaviour
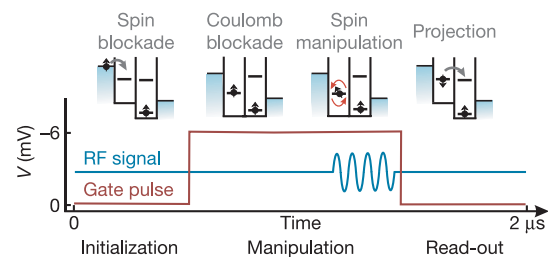

Figure 3 | The control cycle for coherent manipulation of the electron spin. During the 'initialization' stage the double-dot is tuned in the spin blockade regime. Electrons will move from left to right until the system is blocked with two parallel spins (either ↑↑ or ↓↓; in the figure only the ↑↑ case is shown). For the 'manipulation' stage, the right dot potential is pulsed up so none of the levels in the right dot are accessible (Coulomb blockade), and a RF burst with a variable duration is applied. 'Read-out' of the spin state at the end of the manipulation stage is done by pulsing the right dot potential back; electron tunnelling to the right lead will then take place only if the spins were anti-parallel. The duration of the read-out and initialization stages combined was 1 μs, long enough (1 μs $>> 1/\Gamma_L$, $1/\Gamma_M$, $1/\Gamma_R$) to have parallel spins in the dots at the end of the initialization stage with near certainty (this is checked by signal saturation when the pulse duration is prolonged). The duration of the manipulation stage is also held fixed at 1 μs to keep the number of pulses per second constant. The RF burst is applied just before the read-out stage starts.

(Fig. 4b, inset). From the fit we obtain $B_{ac} = 0.59$ mT for a stripline current I_{CPS} of ~1 mA, which agrees well with predictions from numerical finite element simulations (see Supplementary Fig. S1). The maximum B_1 we could reach in the experiment before electric field effects hindered the measurement was 1.9 mT, corresponding to $\pi/2$ rotations of only 27 ns (that is, a Rabi period of 108 ns, see Fig. 4b). If the accompanying electric fields from the stripline excitation could be reduced in future experiments (for example, by improving the impedance matching from coax to CPS), considerably faster Rabi flopping should be attainable.

The oscillations in Fig. 4b remain visible throughout the entire measurement range, up to 1 μs. This is striking, because the Rabi period of ~100 ns is much longer than the time-averaged coherence time T_2^* of 10–20 ns (refs 14, 19, 35, 36) caused by the nuclear field fluctuations. The slow damping of the oscillations is only possible because the nuclear field fluctuates very slowly compared to the timescale of spin rotations and because other mechanisms, such as
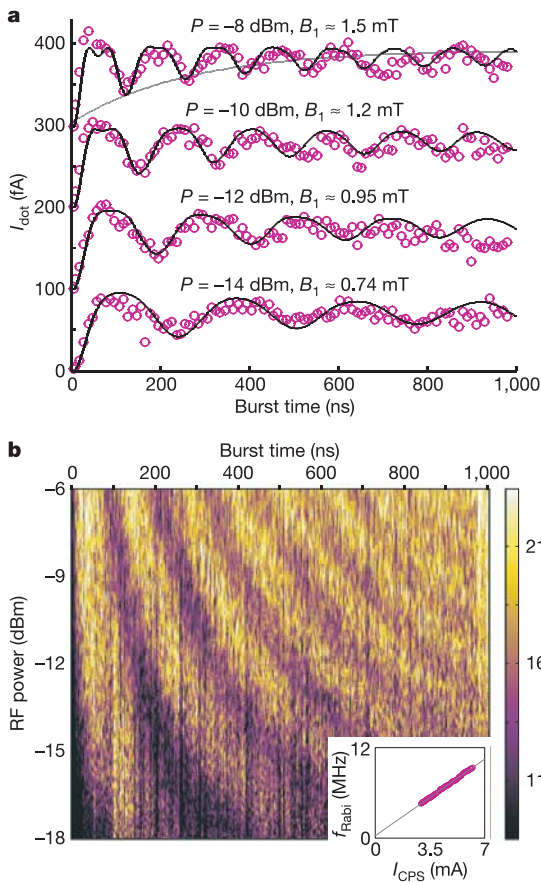
the spin-orbit interaction, disturb the electron spin coherence only on even longer timescales[13,41,42]. We also note that the decay is not exponential (grey line in Fig. 4a), which is related to the fact that the nuclear bath is non-markovian (it has a long memory)[43].

Theoretical model

To understand better the amplitudes and decay times of the oscillations, we model the time evolution of the spins throughout the burst duration. The model uses a hamiltonian that includes the Zeeman splitting for the two spins and the RF field, which we take to be of equal amplitude in both dots ($\mathbf{S}_L$ and $\mathbf{S}_R$ refer to the electron spins in the left and right dot respectively):

$$H = g\mu_B(\mathbf{B}_{ext} + \mathbf{B}_{L,N})\mathbf{S}_L + g\mu_B(\mathbf{B}_{ext} + \mathbf{B}_{R,N})\mathbf{S}_R$$

$$+ g\mu_B \cos(\omega t)\mathbf{B}_{ac}(\mathbf{S}_L + \mathbf{S}_R)$$

where $\mathbf{B}_{L,N}$ and $\mathbf{B}_{R,N}$ correspond to a single frozen configuration of the nuclear field in the left and right dot. This is justified because the electron spin dynamics is much faster than the dynamics of the nuclear system. From the resulting time evolution operator and assuming that the initial state is a statistical mixture of ↑↑ and ↓↓, we can numerically obtain the probability for having anti-parallel spins after the RF burst. This is also the probability that the left electron tunnels to the right dot during the read-out stage.

In the current measurements of Fig. 4a, each data point is averaged over 15 s, which presumably represents an average over many nuclear configurations. We include this averaging over different nuclear configurations in the model by taking 2,000 samples from a gaussian distribution of nuclear fields (with standard deviation $\sigma = \sqrt{\langle B_N^2 \rangle}$), and computing the probability that an electron tunnels out after the RF burst. When the electron tunnels, one or more additional electrons, say m, may subsequently tunnel through before ↑↑ or ↓↓ is formed and the current is blocked again. Taking m and σ as fitting parameters, we find good agreement with the data for $m = 1.5$ and $\sigma = 2.2$ mT (solid black lines in Fig. 4a). This value for σ is comparable to that found in refs 35 and 36. The value found for m is different from what we would expect from a simple picture where all four spin states are formed with equal probability during the initialization stage, which would give $m = 1$. We do not understand this discrepancy, but it could be due to different tunnel rates for ↑ and ↓ or more subtle details in the transport cycle that we have neglected in the model.

Time evolution of the spin states during RF bursts

We now discuss in more detail the time evolution of the two spins during a RF burst. The resonance condition in each dot depends on the effective nuclear field, which needs to be added vectorially to B_{ext}. Through their continuous reorientation, the nuclear spins will bring the respective electron spins in the two dots on and off resonance as time progresses.

When a RF burst is applied to two spins initially in ↑↑, and is on-resonance with the right spin only, the spins evolve as:

$$|\uparrow\rangle|\uparrow\rangle \rightarrow |\uparrow\rangle\frac{|\uparrow\rangle + |\downarrow\rangle}{\sqrt{2}} \rightarrow |\uparrow\rangle|\downarrow\rangle \rightarrow$$

$$|\uparrow\rangle\frac{|\uparrow\rangle - |\downarrow\rangle}{\sqrt{2}} \rightarrow |\uparrow\rangle|\uparrow\rangle$$

When the RF burst is on-resonance with both spins, the time evolution is:

$$|\uparrow\rangle|\uparrow\rangle \rightarrow \frac{|\uparrow\rangle + |\downarrow\rangle}{\sqrt{2}}\frac{|\uparrow\rangle + |\downarrow\rangle}{\sqrt{2}} \rightarrow |\downarrow\rangle|\downarrow\rangle \rightarrow$$

$$\frac{|\uparrow\rangle - |\downarrow\rangle}{\sqrt{2}}\frac{|\uparrow\rangle - |\downarrow\rangle}{\sqrt{2}} \rightarrow |\uparrow\rangle|\uparrow\rangle$$

Figure 4 | Coherent spin rotations. a, The dot current—reflecting the spin state at the end of the RF burst—oscillates as a function of RF burst length (curves offset by 100 fA for clarity). The frequency of B_{ac} is set at the spin resonance frequency of 200 MHz ($B_{ext} = 41$ mT). The period of the oscillation increases and is more strongly damped for decreasing RF power. The RF power P applied to the CPS is estimated from the power applied to the coax line and the attenuation in the lines and RF switch. From P, the stripline current is calculated via the relation $P = \frac{1}{2}\left(\frac{I_{CPS}}{2}\right)^2 Z_0$ assuming perfect reflection of the RF wave at the short. Each measurement point is averaged over 15 s. We correct for a current offset which is measured with the RF frequency off-resonance (280 MHz). The solid lines are obtained from numerical computation of the time evolution, as discussed in the text. The grey line corresponds to an exponentially damped envelope. **b,** The oscillating dot current (represented in colourscale) is displayed over a wide range of RF powers (the sweep axis) and burst durations. The dependence of the Rabi frequency f_{Rabi} on RF power is shown in the inset. f_{Rabi} is extracted from a sinusoidal fit with the current oscillations from 10 to 500 ns for RF powers ranging from −12.5 dBm up to −6 dBm.

In both cases, the RF causes transitions between the ↑ and ↓ states of single spin-half particles. When the RF is on-resonance with both spins, such single-spin rotations take place for both spins simultaneously. Because the current through the dots is proportional to the $S_z = 0$ probability (↑↓ or ↓↑), we see that when both spins are excited simultaneously, the current through the dots will oscillate twice as fast as when only one spin is excited, but with only half the amplitude.

In the experiment, the excitation is on-resonance with only one spin at a time for most of the frozen nuclear configurations (Fig. 5). Only at the highest powers ($B_1/\sqrt{\langle B_{N,z}^2 \rangle} > 1$), both spins may be excited simultaneously (but independently) and a small double Rabi frequency contribution is expected, although it could not be observed, owing to the measurement noise.

Quantum gate fidelity

We can estimate the angle over which the electron spins are rotated in the Bloch sphere based on our knowledge of B_1 and the nuclear field fluctuations in the z-direction, again using the hamiltonian H. For the maximum ratio of $B_1/\sqrt{\langle B_{N,z}^2 \rangle} = B_1/(\sigma/\sqrt{3}) = 1.5$ reached in the present experiment, we achieve an average tip angle of 131° for an intended 180° rotation, corresponding to a fidelity of 73% (Fig. 5). Apart from using a stronger B_1, the tip angle can be increased considerably by taking advantage of the long timescale of the nuclear field fluctuations. First, application of composite pulses, widely used in nuclear magnetic resonance to compensate for resonance off-sets[44], can greatly improve the quality of the rotations. A second solution comprises a measurement of the nuclear field (nuclear state narrowing[45–47]), so that the uncertainty in the nuclear field is reduced, and accurate rotations can be realized for as long as the nuclear field remains constant.
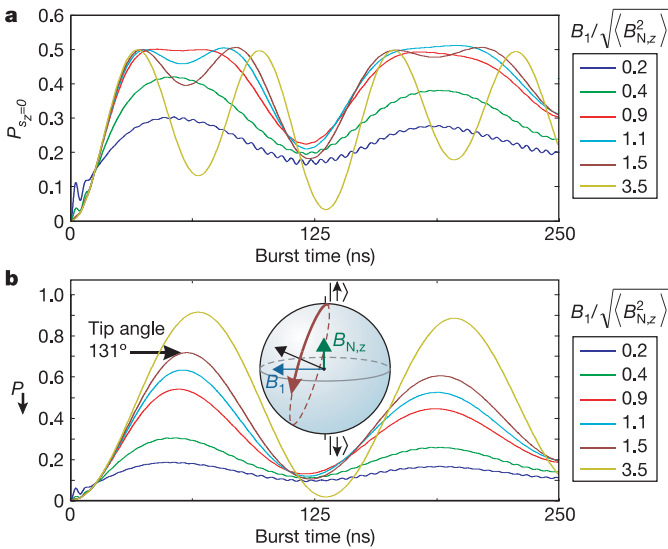

Figure 5 | Time evolution of the spin states. a, Probability for the two spins to be in ↑↓ or ↓↑ ($S_z = 0$) at the end of a RF burst, with initial state ↑↑, computed using the hamiltonian H presented in the main text, for six different values of $\sigma_{N,z} = \langle B_{N,z}^2 \rangle^{1/2}$ (fixed $B_1 = 1.5$ mT, $B_{ext} = 40$ mT, each of the traces is averaged over 2,000 static nuclear configurations). As expected, the oscillation contains a single frequency for B_1 small compared to $\sigma_{N,z}$, corresponding to the Rabi oscillation of a single spin. The oscillation develops a second frequency component, twice as fast as the first, when $B_1/\sigma_{N,z} > 1$. For $B_1/\sigma_{N,z} > 4$ the double frequency component is dominant, reflecting the simultaneous Rabi oscillation of the two spins. **b,** Probability for one of the spins to be ↓ at the end of a RF burst. The spin state evolution is computed as in **a.** This oscillation represents the Rabi oscillation of one spin by itself. For increasing B_1, the maximum angle over which the spin is rotated in the Bloch sphere increases as well. In the experiment, this angle could not be measured directly, because the current measurement constitutes a two-spin measurement, not a single-spin measurement. We can, however, extract the tip angle from $P_\downarrow$.

In future experiments, controllable addressing of the spins in the two dots separately can be achieved through a gradient in either the static or the oscillating magnetic field. Such gradient fields can be created relatively easily using a ferromagnet or an asymmetric stripline. Alternatively, the resonance frequency of the spins can be selectively shifted using local g-factor engineering[48,49]. The single spin rotations reported here, in combination with single-shot spin read-out[13,18] and the tunable exchange coupling in double dots[14], offers many new opportunities, such as measuring the violation of Bell's inequalities or the implementation of simple quantum algorithms.

1. Nielsen, M. A. & Chuang, I. L. *Quantum Computation and Quantum Information* (Cambridge Univ. Press, Cambridge, 2000).
2. Shor, P. W. in *Proc. 35th Annu. Symp. on the Foundations of Computer Science* (ed. Goldwasser, S.) 124–134 (IEEE Computer Society Press, Los Alamitos, California, 1994).
3. Zoller, P. *et al.* Quantum information processing and communication, Strategic report on current status, visions and goals for research in Europe. *Eur. Phys. J. D* 36, 203–228 (2005).
4. DiVincenzo, D. P. Quantum computation. *Science* 270, 255–261 (1995).
5. Loss, D. & DiVincenzo, D. P. Quantum computation with quantum dots. *Phys. Rev. A* 57, 120–126 (1998).
6. Austing, D. G., Honda, T., Muraki, K., Tokura, Y. & Tarucha, S. Quantum dot molecules. *Phys. B Cond. Matter* 249–251, 206–209 (1998).
7. Ciorga, M. *et al.* Addition spectrum of a lateral dot from Coulomb and spin-blockade spectroscopy. *Phys. Rev. B* 61, R16315 (2000).
8. Elzerman, J. M. *et al.* Few-electron quantum dot circuit with integrated charge read out. *Phys. Rev. B* 67, 161308 (2003).
9. Bayer, M. *et al.* Coupling and entangling of quantum states in quantum dot molecules. *Science* 291, 451–453 (2001).
10. Atature, M. *et al.* Quantum-dot spin-state preparation with near-unity fidelity. *Science* 312, 551–553 (2006).
11. Hanson, R. *et al.* Zeeman energy and spin relaxation in a one-electron quantum dot. *Phys. Rev. Lett.* 91, 196802 (2003).
12. Fujisawa, T., Austing, D. G., Tokura, Y., Hirayama, Y. & Tarucha, S. Allowed and forbidden transitions in artificial hydrogen and helium atoms. *Nature* 419, 278–281 (2002).
13. Elzerman, J. M. *et al.* Single-shot read-out of an individual electron spin in a quantum dot. *Nature* 430, 431–435 (2004).
14. Petta, J. R. *et al.* Coherent manipulation of coupled electron spins in semiconductor quantum dots. *Science* 309, 2180–2184 (2005).
15. Schleser, R. *et al.* Time-resolved detection of individual electrons in a quantum dot. *Appl. Phys. Lett.* 85, 2005–2007 (2004).
16. Vandersypen, L. M. K. *et al.* Real-time detection of single-electron tunneling using a quantum point contact. *Appl. Phys. Lett.* 85, 4394–4396 (2004).
17. Lu, W., Ji, Z. Q., Pfeiffer, L., West, K. W. & Rimberg, A. J. Real-time detection of electron tunnelling in a quantum dot. *Nature* 423, 422–425 (2003).
18. Hanson, R. *et al.* Single-shot readout of electron spin states in a quantum dot using spin-dependent tunnel rates. *Phys. Rev. Lett.* 94, 196802 (2005).
19. Dutt, M. V. G. *et al.* Stimulated and spontaneous optical generation of electron spin coherence in charged GaAs quantum dots. *Phys. Rev. Lett.* 94, 227403 (2005).
20. Greilich, A. *et al.* Optical control of spin coherence in singly charged (In,Ga)As/GaAs quantum dots. *Phys. Rev. Lett.* 96, 227401 (2006).
21. Poole, C. P. *Electron Spin Resonance* 2nd edn (Wiley, New York, 1983).
22. Xiao, M., Martin, I., Yablonovitch, E. & Jiang, H. W. Electrical detection of the spin resonance of a single electron in a silicon field-effect transistor. *Nature* 430, 435–439 (2004).
23. Jelezko, F., Gaebel, T., Popa, I., Gruber, A. & Wrachtrup, J. Observation of coherent oscillations in a single electron spin. *Phys. Rev. Lett.* 92, 076401 (2004).
24. Rugar, D., Budakian, R., Mamin, H. J. & Chui, B. W. Single spin detection by magnetic resonance force microscopy. *Nature* 430, 329–332 (2004).
25. Engel, H. A. & Loss, D. Detection of single spin decoherence in a quantum dot via charge currents. *Phys. Rev. Lett.* 86, 4648–4651 (2001).
26. Imamoglu, A. *et al.* Quantum information processing using quantum dot spins and cavity QED. *Phys. Rev. Lett.* 83, 4204–4207 (1999).
27. Kato, Y., Myers, R. C., Gossard, A. C. & Awschalom, D. D. Coherent spin manipulation without magnetic fields in strained semiconductors. *Nature* 427, 50–53 (2003).
28. Golovach, V. N., Borhani, M. & Loss, D. Electric dipole induced spin resonance in quantum dots. Preprint at ⟨www.arXiv.org/cond-mat/0601674⟩ (2006).
29. Tokura, Y., Van der Wiel, W. G., Obata, T. & Tarucha, S. Coherent single electron spin control in a slanting Zeeman field. *Phys. Rev. Lett.* 96, 047202 (2006).
30. Ono, K., Austing, D. G., Tokura, Y. & Tarucha, S. Current rectification by Pauli exclusion in a weakly coupled double quantum dot system. *Science* 297, 1313–1317 (2002).

31. Engel, H. A. *et al.* Measurement efficiency and n-shot readout of spin qubits. *Phys. Rev. Lett.* **93**, 106804 (2004).

32. Blaauboer, M. & DiVincenzo, D. P. Detecting entanglement using a double-quantum-dot turnstile. *Phys. Rev. Lett.* **95**, 160402 (2005).

33. Engel, H. A. & Loss, D. Fermionic bell-state analyzer for spin qubits. *Science* **309**, 586–588 (2005).

34. Johnson, A. C., Petta, J. R., Marcus, C. M., Hanson, M. P. & Gossard, A. C. Singlet-triplet spin blockade and charge sensing in a few-electron double quantum dot. *Phys. Rev. B* **72**, 165308 (2005).

35. Johnson, A. C. *et al.* Triplet-singlet spin relaxation via nuclei in a double quantum dot. *Nature* **435**, 925–928 (2005).

36. Koppens, F. H. L. *et al.* Control and detection of singlet-triplet mixing in a random nuclear field. *Science* **309**, 1346–1350 (2005).

37. Jouravlev, O. N. & Nazarov, Y. V. Electron transport in a double quantum dot governed by a nuclear magnetic field. *Phys. Rev. Lett.* **96**, 176804 (2006).

38. Potok, R. M. *et al.* Spin and polarized current from Coulomb blockaded quantum dots. *Phys. Rev. Lett.* **91**, 016802 (2003).

39. Willems van Beveren, L. H. W. *et al.* Spin filling of a quantum dot derived from excited-state spectroscopy. *New J. Phys.* **7**, 182 (2005).

40. Kogan, A. *et al.* Measurements of Kondo and spin splitting in single-electron transistors. *Phys. Rev. Lett.* **93**, 166602 (2004).

41. Kroutvar, M. *et al.* Optically programmable electron spin memory using semiconductor quantum dots. *Nature* **432**, 81–84 (2004).

42. Golovach, V. N., Khaetskii, A. & Loss, D. Phonon-induced decay of the electron spin in quantum dots. *Phys. Rev. Lett.* **93**, 016601 (2004).

43. Coish, W. A. & Loss, D. Hyperfine interaction in a quantum dot: Non-Markovian electron spin dynamics. *Phys. Rev. B* **70**, 195340 (2004).

44. Vandersypen, L. M. K. & Chuang, I. L. NMR techniques for quantum control and computation. *Rev. Mod. Phys.* **76**, 1037–1069 (2004).

45. Klauser, D., Coish, W. A. & Loss, D. Nuclear spin state narrowing via gate-controlled Rabi oscillations in a double quantum dot. *Phys. Rev. Lett.* **96**, 176804 (2006).

46. Giedke, G., Taylor, J. M., D'Alessandro, D., Lukin, D. & Imamoglu, A. Quantum measurement of the nuclear spin polarization in quantum dots. Preprint at ⟨www.arXiv.org/quant-ph/0508144⟩ (2005).

47. Stepanenko, D., Burkard, G., Giedke, G. & Imamoglu, A. Enhancement of electron spin coherence by optical preparation of nuclear spins. *Phys. Rev. Lett.* **96**, 136401 (2006).

48. Salis, G. *et al.* Electrical control of spin coherence in semiconductor nanostructures. *Nature* **414**, 619–622 (2001).

49. Jiang, H. W. & Yablonovitch, E. Gate-controlled electron spin resonance in GaAs/Al$_x$Ga$_{1-x}$As heterostructures. *Phys. Rev. B* **64**, 041307 (2001).

50. Holleitner, A. W., Blick, R. H. & Eberl, K. Fabrication of coupled quantum dots for multiport access. *Appl. Phys. Lett.* **82**, 1887–1889 (2003).

tinctive features are very similar to those observed in the ~2500-Ma Mt. McRae Shale, and their age is supported by more thorough analytical protocols (24). The discovery and careful analysis of biomarkers in rocks of still greater age and of different Archean environments will potentially offer new insights into early microbial life and its evolution.

References and Notes

1. J. W. Schopf, *Science* **260**, 640 (1993).
2. M. R. Walter, in *Earth's Earliest Biosphere*, J. W. Schopf, Ed. (Princeton Univ. Press, Princeton, NJ, 1983), pp. 187–213.
3. S. J. Mojzsis *et al.*, *Nature* **384**, 55 (1996).
4. J. M. Hayes, I. R. Kaplan, K. W. Wedeking, in (2), pp. 93–134.
5. F. D. Mango, *Nature* **352**, 146 (1991).
6. A. Dutkiewicz, B. Rasmussen, R. Buick, *ibid.* **395**, 885 (1998).
7. K. E. Peters and J. M. Moldowan, *The Biomarker Guide* (Prentice-Hall, Englewood Cliffs, NJ, 1993).
8. R. C. Morris, *Precambrian Res.* **60**, 243 (1993).
9. A. F. Trendall, D. R. Nelson, J. R. de Laeter, S. W. Hassler, *Aust. J. Earth Sci.* **45**, 137 (1998).
10. N. T. Arndt, D. R. Nelson, W. Compston, A. F. Trendall, A. M. Thorne, *ibid.* **38**, 261 (1991).
11. R. E. Smith, J. L. Perdrix, T. C. Parks, *J. Petrol.* **23**, 75 (1982).
12. J. M. Gressier, thesis, University of Sydney, Sydney, Australia (1996).
13. T. C. Hoering and V. Navale, *Precambrian Res.* **34**, 247 (1987).
14. D. R. Nelson, A. F. Trendall, J. R. de Laeter, N. J. Grobler, I. R. Fletcher, *ibid.* **54**, 231 (1992).
15. R. E. Summons, T. G. Powell, C. J. Boreham, *Geochim. Cosmochim. Acta* **52**, 1747 (1988).
16. R. E. Summons and M. R. Walter, *Am. J. Sci.* **290A**, 212 (1990).
17. T. C. Hoering, *Carnegie Inst. Wash. Yearb.* **64**, 215 (1965); *ibid.* **65**, 365, (1966).
18. G. A. Logan, J. M. Hayes, G. B. Heishima, R. E. Summons, *Nature* **376**, 53 (1995); G. A. Logan, R. E. Summons, J. M. Hayes, *Geochim. Cosmochim. Acta* **61**, 5391 (1997).
19. G. A. Logan *et al.*, *Geochim. Cosmochim. Acta*, **63**, 1345 (1999).
20. S. J. Rowland, *Org. Geochem.* **15**, 9 (1990).
21. J. M. Hayes, in *Early Life on Earth*, Nobel Symposium No. 84, S. Bengtson, Ed. (Columbia Univ. Press, New York, 1994), pp. 220–236.
22. J. W. Schopf and B. M. Packer, *Science* **237**, 70 (1987).
23. R. Buick, *ibid.* **255**, 74 (1992).
24. R. E. Summons, L. L. Jahnke, J. M. Hope, G. A. Logan, *Nature*, in press.
25. H. D. Holland and N. J. Beukes, *Am. J. Sci.* **290A**, 1 (1990); A. H. Knoll and H. D. Holland, in *Effects of Past Global Change on Life*, S. M. Stanley, Ed. (National Academy Press, Washington, DC, 1995), pp. 21–33.
26. P. S. Braterman, A. G. Cairns-Smith, R. W. Sloper, *Nature* **303**, 163 (1983).
27. F. Widdel *et al.*, *ibid.* **362**, 834 (1993).
28. P. Cloud, *Science* **160**, 729 (1968); *Econ. Geol.* **68**, 1135 (1973).
29. G. Ourisson, M. Rohmer, K. Poralla, *Annu. Rev. Microbiol.* **41**, 301 (1987).
30. W. Kohl, A. Gloe, H. Reichenbach, *J. Gen. Microbiol.* **129**, 1629 (1983).
31. T.-M. Han and B. Runnegar, *Science* **257**, 232 (1992); A. H. Knoll, *ibid.* **256**, 622 (1992).
32. Supported by the Studienstiftung des Deutschen Volkes (J.J.B.) and American Chemical Society Petroleum Research Fund (R.B.). We thank J. Gressier and RioTinto Exploration for samples, the AGSO Isotope & Organic Geochemistry staff for technical assistance, J. Kamprad for x-ray diffraction analyses, T. Blake, D. Des Marais, L. L. Jahnke, C. J. Boreham, D. S. Edwards, T. G. Powell, D. E. Canfield, and M. R. Walter for advice, and J. M. Hayes, A. Knoll, and an anonymous reviewer for their thoughtful comments. G.A.L. and R.E.S. publish with the permission of the Executive Director of AGSO.

19 May 1999; accepted 13 July 1999

REPORTS

Josephson Persistent-Current Qubit

J. E. Mooij,[1,2]* T. P. Orlando,[2] L. Levitov,[3] Lin Tian,[3] Caspar H. van der Wal,[1] Seth Lloyd[4]

A qubit was designed that can be fabricated with conventional electron beam lithography and is suited for integration into a large quantum computer. The qubit consists of a micrometer-sized loop with three or four Josephson junctions; the two qubit states have persistent currents of opposite direction. Quantum superpositions of these states are obtained by pulsed microwave modulation of the enclosed magnetic flux by currents in control lines. A superconducting flux transporter allows for controlled transfer between qubits of the flux that is generated by the persistent currents, leading to entanglement of qubit information.

In a quantum computer, information is stored on quantum variables such as spins, photons, or atoms (1–3). The elementary unit is a two-state quantum system called a qubit. Computations are performed by the creation of quantum superposition states of the qubits and by controlled entanglement of the information on the qubits. Quantum coherence must be conserved

to a high degree during these operations. For a quantum computer to be of practical value, the number of qubits must be at least 10^4. Qubits have been implemented in cavity quantum electrodynamics systems (4), ion traps (5), and nuclear spins of large numbers of identical molecules (6). Quantum coherence is high in these systems, but it seems difficult or impossible to realize the desired high number of interacting qubits. Solid state circuits lend themselves to large-scale integration, but the multitude of quantum degrees of freedom leads in general to short decoherence times. Proposals have been put forward for future implementation of qubits with spins of individual donor atoms in silicon (7), with spin states in quantum dots (8), and with d-wave superconductors (9); the technology for practical realization still needs to be developed.

In superconductors, all electrons are condensed in the same macrosopic quantum state, separated by a gap from the many quasi-particle states. This gap is a measure for the strength of the superconducting effects. Superconductors can be weakly coupled with Josephson tunnel junctions (regions where only a thin oxide separates them). The coupling energy is given by $E_J(1 - \cos \gamma)$, where the Josephson energy E_J is proportional to the gap of the superconductors divided by the normal-state tunnel resistance of the junction and γ is the gauge-invariant phase difference of the order parameters. The current through a Josephson junction is equal to $I_o \sin \gamma$, with $I_o = (2e/\hbar) E_J$, where e is the electron charge and $\hbar$ is Planck's constant divided by 2π. In a Josephson junction circuit with small electrical capacitance, the numbers of excess Cooper pairs on islands n_i, n_j and the phase differences γ_i, γ_j are related as noncommuting conjugate quantum variables (10). The Heisenberg uncertainty between phase and charge and the occurrence of quantum superpositions of charges as well as phase excitations (vortexlike fluxoids) have been demonstrated in experiments (11). Coherent charge oscillations in a superconducting quantum box have recently been observed (12). Qubits for quantum computing based on charge states have been suggested (13, 14). However, in actual practice, fabricated Josephson circuits exhibit a high level of static and dynamic charge noise due to charged impurities. In contrast, the magnetic background is clean and stable. Here, we present the design of a qubit with persistent currents of opposite sign as its basic states. The qubits

[1]Department of Applied Physics and Delft Institute for Microelectronics and Submicron Technologies, Delft University of Technology, Post Office Box 5046, 2600 GA Delft, Netherlands. [2]Department of Electrical Engineering and Computer Science, [3]Department of Physics and Center for Materials Science and Engineering, [4]Department of Mechanical Engineering, Massachusetts Institute of Technology, Cambridge, MA 02139, USA.

*To whom correspondence should be addressed. E-mail: mooij@qt.tn.tudelft.nl

Fig. 1. Persistent current qubit. (**A**) Three-junction qubit. A superconducting loop with three Josephson junctions (indicated with crosses) encloses a flux that is supplied by an external magnet. The flux is $f\Phi_o$, where Φ_o is the superconducting flux quantum and f is 0.495. Two junctions have a Josephson coupling energy E_J, and the

third junction has αE_J, where $\alpha = 0.75$. This system has two (meta)stable states $|0\rangle$ and $|1\rangle$ with opposite circulating persistent current. The level splitting is determined by the offset from $\Phi_o/2$ of the flux. The barrier between the states depends on the value of α. The qubit is operated by resonant microwave modulation of the enclosed magnetic flux by a superconducting control line (indicated in red). (**B**) Four-junction qubit. The top junction of (A) is replaced by a parallel junction (SQUID) circuit. There are two loops with equal areas; a magnet supplies a static flux $0.330\Phi_o$ to both. Qubit operations are performed with currents in superconducting control lines (indicated in red) on top of the qubit, separated by a thin insulator. The microwave current I_{c1} couples only to the bottom loop and performs qubit operations as in (A). I_{c2} couples to both loops; it is used for qubit operations with suppressed σ_z action and for an adiabatic increase of the tunnel barrier between qubit states to facilitate the measurement.
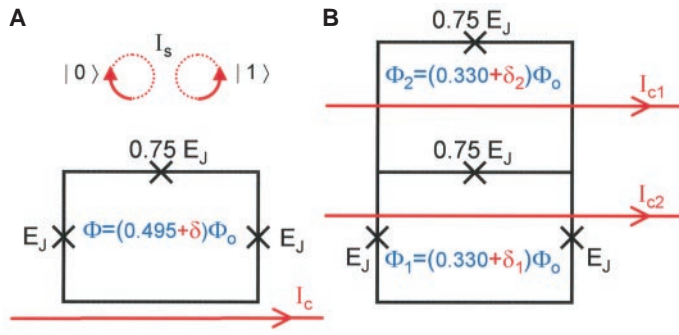
can be driven individually by magnetic microwave pulses; measurements can be made with superconducting magnetometers [superconducting quantum interference devices (SQUIDs)]. They are decoupled from charges and electrical signals, and the known sources of decoherence allow for a decoherence time of more than 1 ms. Switching is possible at a rate of 100 MHz. Entanglement is achieved by coupling the flux, which is generated by the persistent current, to a second qubit. The qubits are small (of order 1 μm), can be individually addressed, and can be integrated into large circuits.

Our qubit in principle consists of a loop with three small-capacitance Josephson junctions in series (Fig. 1A) that encloses an applied magnetic flux $f\Phi_o$ (Φ_o is the superconducting flux quantum $h/2e$, where h is Planck's constant); f is slightly smaller than 0.5. Two of the junctions have equal Joseph-

son coupling energy E_J; the coupling in the third junction is αE_J, with $0.5 < \alpha < 1$. Useful values are $f = 0.495$ and $\alpha = 0.75$ (as chosen in Fig. 1A). This system has two stable classical states with persistent circulating currents of opposite sign. For $f = 0.5$, the energies of the two states are the same; the offset from 0.5 determines the level splitting. The barrier for quantum tunneling between the states depends strongly on the value of α. The four-junction version (Fig. 1B) allows modulation of this barrier in situ. Here, the third junction has been converted into a parallel circuit of two junctions, each with a coupling energy αE_J. The four-junction qubit behaves as the three-junction circuit of Fig. 1A, with an enclosed flux $(f_1 + f_2/2)\Phi_o$ and a third-junction (SQUID) strength $2\alpha E_J \cos(f_2\pi)$. The constant fluxes $f\Phi_o$, $f_1\Phi_o$, and $f_2\Phi_o$ are supplied by an external, static, homogeneous magnetic field. Control lines on a

separate fabrication level couple inductively to individual qubit loops. All operations on qubits are performed with currents in the control lines.

When γ_1 and γ_2 are the gauge-invariant phase differences across the left and right junctions, the Josephson energy of the four-junction qubit U_J is

$$U_J/E_J = 2 + 2\alpha - \cos\gamma_1 - \cos\gamma_2 - 2\alpha \cos$$
$$(f_2\pi)\cos(2f_1\pi + f_2\pi + \gamma_1 - \gamma_2) \qquad (1)$$

In this expression, the self-generated flux has been neglected. Although this flux will be used for coupling of qubits, it is much smaller than the flux quantum and only slightly changes the picture here. U_J is 2π periodic in γ_1 and γ_2 (Fig. 2A) for the parameter values $\alpha = 0.75$ and $f_1 = f_2 = 0.330$. Each unit cell has two minima L_{ij} and R_{ij} with left- and right-handed circulating currents of about $0.75I_o$ at approximate γ_1, γ_2 values of $\pm 0.27\pi$. The minima would have been symmetric for $2f_1 + f_2 = 1$, which corresponds to a three-junction loop enclosing half a flux quantum. The set of all L minima yields one qubit state and the set of R minima the other. In γ_1, γ_2 space, there are saddle-point connections between L and R minima as indicated with red (intracell, in) and blue lines (intercell, out). Along such trajectories, the system can tunnel between its macroscopic quantum states. The Josephson energy along the trajectories is plotted in Fig. 2B. The saddle-point energies U_{in} and U_{out} depend on α and f_2; lower SQUID coupling gives lower U_{in} but higher U_{out}. For $2\alpha \cos(f_2\pi) < 0.5$, the barrier for intracell tunneling has disappeared, and there is only one minimum with zero circulating current.

Motion of the system in γ_1, γ_2 space can be discussed in analogy with motion of a mass-carrying particle in a landscape with periodic potential energy. Motion in phase space leads to voltages across junctions. The kinetic energy is the associated Coulomb charg-
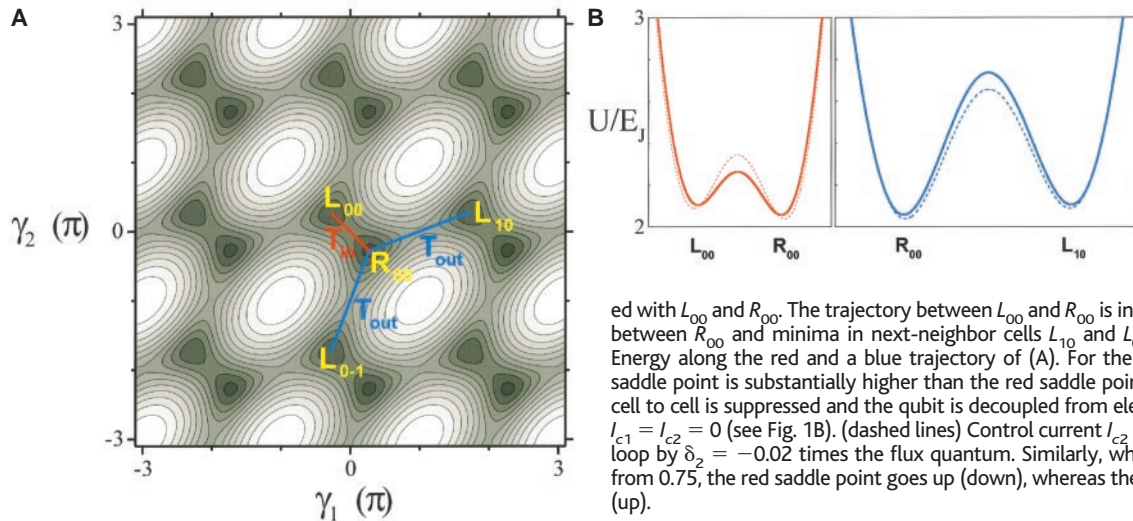

Fig. 2. Josephson energy of qubit in phase space. (**A**) Energy plotted as a function of the gauge-invariant phase differences γ_1 and γ_2 across the left and right junctions of Fig. 1A. The energy is periodic with period 2π. There are two minima in each unit cell, for the center cell indicated with L_{00} and R_{00}. The trajectory between L_{00} and R_{00} is indicated in red; the trajectories between R_{00} and minima in next-neighbor cells L_{10} and L_{0-1} are indicated in blue. (**B**) Energy along the red and a blue trajectory of (A). For the parameters chosen, the blue saddle point is substantially higher than the red saddle point. As a result, tunneling from cell to cell is suppressed and the qubit is decoupled from electrical potentials. (solid lines) $I_{c1} = I_{c2} = 0$ (see Fig. 1B). (dashed lines) Control current I_{c2} reduces the flux in the SQUID loop by $\delta_2 = -0.02$ times the flux quantum. Similarly, when α is increased (decreased) from 0.75, the red saddle point goes up (down), whereas the blue saddle point goes down (up).

ing energy of the junction capacitances. The mass is proportional to the junction capacitance C because other capacitance elements are small. The effective mass tensor has principal values M_a and M_b in the $\gamma_1 - \gamma_2 = 0$ and $\gamma_1 + \gamma_2 = 0$ directions. For the chosen values of the circuit parameters, these principal values are $M_a = \hbar^2/(4E_C)$ and $M_b = \hbar^2/(E_C)$, where the charging energy is defined as $E_C = e^2/2C$. The system will perform plasma oscillations in the potential well with frequencies $\hbar\omega_b \approx 1.3(E_C E_J)^{1/2}$ and $\hbar\omega_a \approx 2.3(E_C E_J)^{1/2}$. The tunneling matrix elements can be estimated by calculation of the action in the Wentzel-Kramers-Brillouin approximation. For tunneling within the unit cell between the minima L and R, the matrix element is $T_{in} \approx \hbar\omega_b \exp[-0.64(E_J/E_C)^{1/2}]$; for tunneling from cell to cell, the matrix element is $T_{out} \approx 1.6\hbar\omega_b\exp[-1.5(E_J/E_C)^{1/2}]$. For the qubit, a subtle balance has to be struck: The plasma frequency must be small enough relative to the barrier height to have well-defined states with a measurable circulating current but large enough (small enough mass) to have substantial tunneling. The preceding qualitative discussion has been confirmed by detailed quantitative calculations in phase space and in charge space (*15*). From these calculations, the best parameters for qubits can be determined. In practice, it is possible to controllably fabricate aluminum tunnel junctions with chosen E_J and E_C values in a useful range.

It is strongly desirable to suppress the intercell tunneling T_{out}. This suppression leads to independence from electrical potentials, even if the charges on the islands are conjugate quantum variables to the phases. The qubit system in phase space is then comparable to a crystal in real space with nonoverlapping atomic wave functions. In such a crystal, the electronic wave functions are independent of momentum; similarly, charge has no influence in our qubit.

Mesoscopic aluminum junctions can be reliably fabricated by shadow evaporation with critical current densities up to 500 A/cm². In practice, a junction of 100 nm² by

100 nm² has E_J around 25 GHz and E_C around 20 GHz. A higher E_J/E_C ratio can be obtained by increasing the area to which E_J is proportional and E_C is inversely proportional. A practical qubit would, for example, have junctions with an area of 200 nm² by 400 nm², $E_J \sim 200$ GHz, $E_J/E_c \sim 80$, level splitting $\Delta E \sim 10$ GHz, barrier height around 35 GHz, plasma frequency around 25 GHz, and tunneling matrix element $T_{in} \sim 1$ GHz. The matrix element for undesired tunneling T_{out} is smaller than 1 MHz. The qubit size would be of order 1 μm; with an estimated inductance of 5 pH, the flux generated by the persistent currents is about $10^{-3}\Phi_o$.

To calculate the dependence of the level splitting on f_1 and f_2, we apply a linearized approximation in the vicinity of $f_1 = f_2 = 1/3$, defining F as the change of U_J away from the minimum of $U_J(\gamma_1,\gamma_2)$. This yields $F/E_J = 1.2[2(f_1 - 1/3)+(f_2 - 1/3)]$. The level splitting without tunneling would be $2F$. With tunneling, symmetric and antisymmetric combinations are created; the level splitting is now $\Delta E = 2(F^2 + T_{in}^2)^{1/2}$. As long as $F \gg T_{in}$, the newly formed eigenstates are localized in the minima of $U_J(\gamma_1,\gamma_2)$.

We discuss qubit operations for the four-junction qubit. They are driven by the currents I_{ca} and I_{cb} in the two control lines (Fig. 1B). The fluxes induced in the two loops, normalized to the flux quantum, are $\delta_1 = (L_{a1}I_{ca} + L_{b1}I_{cb})/\Phi_o$ and $\delta_2 = (L_{a2}I_{ca} + L_{b2}I_{cb})/\Phi_o$. The control line positions are chosen such that $L_{a2} = 0$ and $L_{b2} = -2L_{b1}$. When the two loops have equal areas, $f_1 = f_2$ for zero control current. We assume that the qubit states are defined with zero control current and that δ_1 and δ_2 act as perturbations to this system. The effective Hamiltonian operator (H_{op}) in terms of Pauli spin matrices σ_x and σ_z for the chosen parameters is about

$$H_{op}/\Delta E \approx (80\delta_1 + 42\delta_2)\sigma_z$$
$$- (9.2\delta_1 + 8.3\delta_2)\sigma_x \qquad (2)$$

The numerical prefactors follow from the variational analysis of the influence of δ_1 and δ_2 on the tunnel barrier and the level splitting.

The terms that contain σ_x can be used to induce Rabi oscillations between the two states, applying microwave pulses of frequency $\Delta E/h$. There are two main options, connected to one of the two control lines. Control current I_{ca} changes δ_1, which leads to a Rabi oscillation (σ_x term) as well as a strong modulation of the Larmor precession (σ_z term). As long as the Rabi frequency is far enough below the Larmor frequency, this is no problem. For $\delta_1 = 0.001$, the Rabi frequency is 100 MHz. This mode is the only one available for the three-junction qubit and is most effective near the symmetry point $f = 0.5$ or $f_1 = f_2 = 1/3$. Control current I_{cb} is used to modulate the tunnel barrier. Here, the σ_z action is suppressed by means of the choice $L_{b2}/L_{b1} = \delta_2/\delta_1 = -2$. However, a detailed analysis shows that with δ_2 modulation, it is easy to excite the plasma oscillation with frequency ω_b. One has to restrict δ_2 to remain within the two-level system. Values of 0.001 for δ_1 or δ_2 correspond to about 50-pW microwave power at 10 GHz in the control line. These numbers are well within practical range.

Two or more qubits can be coupled by means of the flux that the circulating persistent current generates. The current is about 0.3 μA, the self-inductance of the loop is about 5 pH, and the generated flux is about $10^{-3}\Phi_o$. When a superconducting closed loop (a flux transporter) with high critical current is placed on top of both qubits, the total enclosed flux is constant. A flux change $\Delta\Phi$ that is induced by a reversal of the current in one qubit leads to a change of about $\Delta\Phi/2$ in the flux that is enclosed by the other qubit. One can choose to couple the flux, generated in the main loop of qubit 1, to the main loop of qubit 2 ($\sigma_z\otimes\sigma_z$ coupling) or to the SQUID loop of qubit 2 ($\sigma_z\otimes\sigma_x$ coupling). A two-qubit gate operation is about as efficient as a single qubit operation driven with $\delta_1 = 0.001$. An example of a possible controlled-NOT operation with fixed coupling runs as follows: The level splitting of qubit 2 depends on the state of qubit 1, the values are ΔE_{20} and ΔE_{21}. When Rabi microwave pulses, resonant with ΔE_{21}, are applied to qubit 2, it will only react if qubit 1 is in its I1> state. In principle, qubits can be coupled at larger distances. An array scheme as proposed by Lloyd (*1, 3*), where only nearest neighbor qubits are coupled, is also very feasible. It is possible to create a flux transporter that has to be switched on by a control current (Fig. 3).

The typical switching times for our qubit are 10 to 100 ns. To yield a practical quantum computer, the decoherence time should be at least 100 μs. We can estimate the influence of known sources of decoherence for our system, but it is impossible to determine the real decoherence time with certainty, except by measurement. We discuss

Fig. 3. Switchable qubit coupler. A superconducting flux transporter (blue) is placed on top of two qubits, separated by a thin insulator. The transporter is a closed loop that contains two Josephson junctions in parallel (SQUID) with high critical current. In the off state, the two loops of the transporter contain an integer number of flux quanta (main loop) and half a flux quantum (SQUID loop), supplied by a permanent magnet. The current response to a flux change is very small. In the on state, the flux in the SQUID loop is made integer by means of a control current I_{ct} (red). As the transporter attempts to keep the flux in its loop constant, a flux change induced by qubit 1 is transmitted to qubit 2. As shown here, the two three-junction qubits experience $\sigma_z\otimes\sigma_z$-type coupling. The flux values have to be adjusted for the influence of circulating currents.
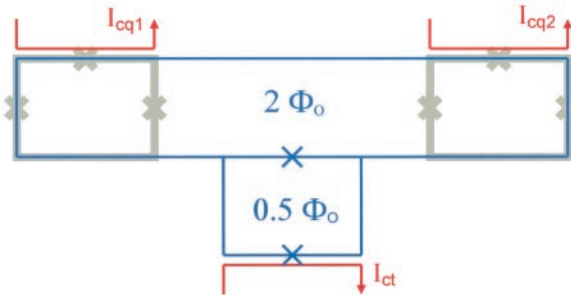
some decohering influences here. All quasi-particle states in the superconductor have to remain unoccupied. In equilibrium, the number is far below 1 at temperatures below 30 mK. Extreme care must be taken to shield the sample from photons. Even 4 K blackbody photons have enough energy to break a Cooper pair. Adequate shielding is possible on the time scale of our computer. Inductive coupling to bodies of normal metal has to be avoided. By decoupling the qubit from electrical potentials, we have eliminated coupling to charged defects in substrate or tunnel barriers. The aluminum nuclei have a spin that is not polarized by the small magnetic fields at our temperature of 25 mK. Statistical fluctuations will occur, but their time constant is very long because of the absence of electronic quasi-particles. The net effect will be a small static offset of the level splitting, within the scale of the variations due to fabrication. The dephasing time that results from unintended dipole-dipole coupling of qubits is longer than 1 ms if the qubits are farther apart than 1 μm. Emission of photons is negligible for the small loop. Overall, the sources of decoherence that we know allow for a decoherence time above 1 ms.

Requirements for a quantum computer are that the qubits can be prepared in well-defined states before the start of the computation and that their states can be measured at the end. Initialization will proceed by cooling the computer to below 50 mK and having the qubits settle in the ground state. For the measurement, a generated flux of $10^{-3}\Phi_o$ in an individual qubit can be detected with a SQUID if enough measuring time is available. A good SQUID has a sensitivity of $10^{-5}\Phi_o/\mathrm{Hz}^{1/2}$, so that a time of 100 μs is required. Usual SQUIDs have junctions that are shunted with normal metal. The shunt introduces severe decoherence in a qubit when the SQUID is in place, even if no measurement is performed. We are developing a nonshunted SQUID that detects its critical current by discontinuous switching. For a measurement at the end of a quantum computation scheme, the qubit can be frozen by an adiabatic increase of the tunnel barrier between the two qubit states. As Fig. 2 indicates, we can increase the barrier by a change of control current. A similar procedure, as suggested by Shnirman and Schön (14), for charge qubits can be followed.

The proposed qubit should be of considerable interest for fundamental studies of macroscopic quantum coherence, apart from its quantum computing potential. Compared with the radio frequency SQUID systems that have been used in attempts to observe such effects (16) and also have been suggested as possible qubits for quantum computation (17), the much smaller size of the qubit decouples it substantially better from the environment.

References and Notes

1. S. Lloyd, *Science* **261**, 1569 (1993).
2. C. H. Bennett, *Phys. Today* **48** (no. 10), 24 (1995); D. P. DiVincenzo, *Science* **270**, 255 (1995); T. P. Spiller, *Proc. IEEE* **84**, 1719 (1996).
3. S. Lloyd, *Sci. Am.* **273** (no. 4), 140 (1995).
4. Q. A. Turchette, C. J. Hood, W. Lange, H. Mabuchi, H. J. Kimble, *Phys. Rev. Lett.* **75**, 4710 (1995).
5. C. Monroe, D. M. Meekhof, B. E. King, W. M. Itano, D. J. Wineland, *ibid.*, p. 4714.
6. N. A. Gershenfeld and I. L. Chuang, *Science* **275**, 350 (1997).
7. B. Kane, *Nature* **393**, 133 (1998).
8. D. Loss and D. DiVincenzo, *Phys. Rev. A* **57**, 120 (1998).
9. L. B. Ioffe, V. B. Geshkenbein, M. V. Feigel'man, A. L. Fauchère, G. Blatter, *Nature* **398**, 679 (1999).
10. D. V. Averin and K. K. Likharev, in *Mesoscopic Phenomena in Solids*, B. L. Altshuler, P. A. Lee, R. A. Webb, Eds. (North Holland, Amsterdam, 1991), pp. 173–271.
11. W. J. Elion, M. Matters, U. Geigenmuller, J. E. Mooij, *Nature* **371**, 594 (1994); L. S. Kuzmin and D. B. Haviland, *Phys. Rev. Lett.* **67**, 2890 (1991); P. Joyez, D. Esteve, M. H. Devoret, *ibid.* **80**, 1956 (1998).
12. Y. Nakamura, Yu. A. Pashkin, J. S. Tsai, *Nature* **398**, 786 (1999).
13. A. Shnirman, G. Schön, Z. Hermon, *Phys. Rev. Lett.* **79**, 2371 (1997); D. V. Averin, *Solid State Commun.* **105**, 659 (1998); Yu. Makhlin, G. Schön, A. Shnirman, *Nature* **398**, 305 (1999).
14. A. Shnirman and G. Schön, *Phys. Rev. B* **57**, 15400 (1998).
15. T. P. Orlando *et al.*, in preparation.
16. C. D. Tesche, *Phys. Rev. Lett.* **64**, 2358 (1990); R. Rouse, S. Han, J. E. Lukens, *ibid.* **75**, 1614 (1995).
17. M. F. Bocko, A. M. Herr, M. J. Feldman, *IEEE Trans. Appl. Supercond.* **7**, 3638 (1997).
18. We thank J. J. Mazo, C. J. P. M. Harmans, A. C. Wallast, and H. Tanaka for important discussions. This work is partially supported by Army Research Office grant DAAG55-98-1-0369, Stichting voor Fundamenteel Onderzoek der Materie, NSF Award 67436000IRG, and the New Energy and Industrial Technology Development Organization.

Energetic Iron(VI) Chemistry: The Super-Iron Battery

Stuart Licht,* Baohui Wang, Susanta Ghosh

Higher capacity batteries based on an unusual stabilized iron(VI) chemistry are presented. The storage capacities of alkaline and metal hydride batteries are largely cathode limited, and both use a potassium hydroxide electrolyte. The new batteries are compatible with the alkaline and metal hydride battery anodes but have higher cathode capacity and are based on available, benign materials. Iron(VI/III) cathodes can use low-solubility K_2FeO_4 and $BaFeO_4$ salts with respective capacities of 406 and 313 milliampere-hours per gram. Super-iron batteries have a 50 percent energy advantage compared to conventional alkaline batteries. A cell with an iron(VI) cathode and a metal hydride anode is significantly (75 percent) rechargeable.

Improved batteries are needed for various applications such as consumer electronics, communications devices, medical implants, and transportation needs. The search for higher capacity electrochemical storage has focused on a wide range of materials, such as carbonaceous materials (1), tin oxide (2), grouped electrocatalysts (3), or macroporous minerals (4). Of growing importance are rechargeable (secondary) batteries such as metal hydride (MH) batteries (5), which this year have increased the commercial electric car range to 250 km per charge. In consumer electronics, primary, rather than secondary, batteries dominate. Capacity, power, cost, and safety factors have led to the annual global use of approximately 6×10^{10} alkaline or dry batteries, which use electrochemical storage based on a Zn anode, an aqueous electrolyte, and a MnO_2 cathode, and which constitute the vast majority of consumer batteries. Despite the need for safe, inexpensive, higher capacity electrical storage, the aqueous MnO_2/Zn battery has been a dominant primary battery chemistry for over a century. Contemporary alkaline and MH batteries have two common features: Their storage capacity is largely cathode limited and both use a KOH electrolyte.

We report a new class of batteries, referred to as super-iron batteries, which contain a cathode that uses a common material (Fe) but in an unusual (greater than 3) valence state. Although they contain the same Zn anode and electrolyte as conventional alkaline batteries, the super-iron batteries provide >50% more energy capacity. In addition, the Fe(VI) chemistry is rechargeable, is based on abundant starting materials, has a relatively environmentally benign discharge product, and appears to be compatible with the anode of either the primary alkaline or secondary MH batteries.

The fundamentals of MnO_2 chemistry continue to be of widespread interest (6). The storage capacity of the aqueous MnO_2/Zn

Department of Chemistry and Institute of Catalysis Science, Technion—Israel Institute of Technology, Haifa 32000, Israel.

*To whom correspondence should be addressed. E-mail: chrlicht@techunix.technion.ac.il

18. The International HapMap Consortium, *Nature* **426**, 789 (2003).
19. A. R. Templeton, E. Boerwinkle, C. F. Sing, *Genetics* **117**, 343 (1987).
20. D. W. Schultz *et al.*, *Hum. Mol. Genet.* **12**, 3315 (2003).
21. M. Hayashi *et al.*, *Ophthalmic Genet.* **25**, 111 (2004).
22. G. J. McKay *et al.*, *Mol. Vis.* **10**, 682 (2004).
23. S. Rodríguez de Cordoba, J. Esparza-Gordillo, E. Goicoechea de Jorge, M. Lopez-Trascasa, P. Sanchez-Corral, *Mol. Immunol.* **41**, 355 (2004).
24. L. V. Johnson, W. P. Leitner, M. K. Staples, D. H. Anderson, *Exp. Eye Res.* **73**, 887 (2001).
25. R. F. Mullins, S. R. Russell, D. H. Anderson, G. S. Hageman, *FASEB J.* **14**, 835 (2000).
26. J. Ambati *et al.*, *Nat. Med.* **9**, 1390 (2003).
27. G. S. Hageman *et al.*, *Prog. Retinal Eye Res.* **20**, 705 (2001).
28. J. Esparza-Gordillo *et al.*, *Immunogenetics* **56**, 77 (2004).
29. G. Wistow *et al.*, *Mol. Vis.* **8**, 205 (2002).
30. R. F. Mullins, N. Aptsiauri, G. S. Hageman, *Eye* **15**, 390 (2001).
31. A. M. Blom, L. Kask, B. Ramesh, A. Hillarp, *Arch. Biochem. Biophys.* **418**, 108 (2003).
32. J. M. Seddon, G. Gensler, R. C. Milton, M. L. Klein, N. Rifai, *JAMA* **291**, 704 (2004).
33. The Raymond and Beverly Sackler Fund for Arts and Sciences' generous support made this project possible. We thank Raymond Sackler, J. Sackler, and E. Vosburg for their input and encouragement. We also thank AREDS participants and investigators; G. Gensler, T. Clemons, and A. Lindblad for work on the AREDS Genetic Repository; S. Westman and A. Evan for assistance with the microarrays; R. Fariss for the human retinal sections and advice on confocal microscopy; E. Johnson for assistance with immunostaining; and J. Majewski for constructive comments on the manuscript. Partially funded by NIH-K25HG000060 and NIH-R01EY015771 (J.H.), Macula Vision Research Foundation and the David Woods Kemper Memorial Foundation (C.B.), NIH-R01MH44292 (J.O.), and NIH-K01RR16090 and Yale Pepper Center for Study of Diseases in Aging (C.Z.). This work also benefited from the International HapMap Consortium making their data available prior to publication.

REPORTS

Quantum Phase Transition of a Magnet in a Spin Bath

H. M. Rønnow,[1,2,3]* R. Parthasarathy,[2] J. Jensen,[4] G. Aeppli,[5] T. F. Rosenbaum,[2] D. F. McMorrow[3,4,6]

The excitation spectrum of a model magnetic system, LiHoF$_4$, was studied with the use of neutron spectroscopy as the system was tuned to its quantum critical point by an applied magnetic field. The electronic mode softening expected for a quantum phase transition was forestalled by hyperfine coupling to the nuclear spins. We found that interactions with the nuclear spin bath controlled the length scale over which the excitations could be entangled. This generic result places a limit on our ability to observe intrinsic electronic quantum criticality.

The preparation and preservation of entangled quantum states is particularly relevant for the development of quantum computers, where interacting quantum bits (qubits) must produce states sufficiently long lived for meaningful manipulation. The state lifetime, typically referred to as decoherence time, is derived from coupling to the background environment. For solid-state quantum computing schemes, the qubits are typically electron spins, and they couple to two generic background environments (*1*). The oscillator bath—that is, delocalized environmental modes (*2*) such as thermal vibrations coupled via magnetoelastic terms to the spins—can be escaped by lowering the temperature to a point where the lattice is essentially

frozen. Coupling to local degrees of freedom, such as nuclear magnetic moments that form a spin bath, may prove more difficult to avoid, because all spin-based candidate materials for quantum computation have at least one naturally occurring isotope that carries nuclear spin.

Experimental work in this area has been largely restricted to the relaxation of single, weakly interacting magnetic moments such as those on large molecules (*3*); much less is known about spins as they might interact in a real quantum computer. In this regard, the insight that quantum phase transitions (QPTs) (*4*) are a good arena for looking at fundamental quantum properties of strongly interacting spins turns out to be valuable, as it has already been for explorations of entanglement. In particular, we show that coupling to a nuclear spin bath limits the distance over which quantum mechanical mixing affects the electron spin dynamics.

QPTs are transitions between different ground states driven not by thermal fluctuations but by quantum fluctuations controlled by a parameter such as doping, pressure, or magnetic field (*5*, *6*). Much of the interest in QPTs stems from their importance for understanding materials with unconventional properties, such as heavy fermion systems and high-temperature

superconductors. However, these materials are rather complex and do not easily lend themselves to a universal understanding of QPTs. To this end, it is desirable to identify quantum critical systems with a well-defined and solvable Hamiltonian and with a precisely controllable tuning parameter. One very simple model displaying a QPT is the Ising ferromagnet in a transverse magnetic field (*5*, *7–9*) with the Hamiltonian

$$\mathcal{H} = -\sum_{ij} \mathcal{J}_{ij}\, \sigma_i^z \cdot \sigma_j^z - \Gamma \sum_i \sigma_i^x \quad (1)$$

where $\mathcal{J}_{ij}$ is the coupling between the spins on sites i and j represented by the Pauli matrices σ^z with eigenvalues ± 1. In the absence of a magnetic field, the system orders ferromagnetically below a critical temperature T_c. The transverse-field Γ mixes the two states and leads to destruction of long-range order in a QPT at a critical field Γ_c, even at zero temperature. In the ferromagnetic state at zero field and temperature, the excitation spectrum is momentum independent and is centered at the energy $4\sum_j J_{ij}$ associated with single-spin reversal. Upon application of a magnetic field, however, the excitations acquire a dispersion, softening to zero at the zone center $q = 0$ when the QPT is reached.

We investigated the excitation spectrum around the QPT in LiHoF$_4$, which is an excellent physical realization of the transverse-field Ising model, with an added term accounting for the hyperfine coupling between electronic and nuclear moments (*10–12*). The dilution series LiHo$_x$Y$_{1-x}$F$_4$ is the host for a wide variety of collective quantum effects, ranging from tunneling of single moments and domain walls to quantum annealing, entanglement, and Rabi oscillations (*13–17*). These intriguing properties rely largely on the ability of a transverse field, whether applied externally or generated internally by the off-diagonal part of the magnetic dipolar interaction, to mix two degenerate crystal field states of each Ho ion.

[1]Laboratory for Neutron Scattering, ETH-Zürich and Paul Scherrer Institut, 5232 Villigen, Switzerland. [2]James Franck Institute and Department of Physics, University of Chicago, Chicago, IL 60637, USA. [3]Risø National Laboratory, DK-4000 Roskilde, Denmark. [4]Ørsted Laboratory, Niels Bohr Institute fAPG, Universitetsparken 5, 2100 Copenhagen, Denmark. [5]London Centre for Nanotechnology and Department of Physics and Astronomy, University College London, London WC1E 6BT, UK. [6]ISIS, Rutherford Appleton Laboratory, Chilton, Didcot OX11 0QX, UK.

*To whom correspondence should be addressed. E-mail: henrik.ronnow@psi.ch

The Ho ions in LiHoF$_4$ are placed on a tetragonal Scheelite lattice with parameters $a = 5.175$ Å and $c = 10.75$ Å. The crystal-field ground state is a $\Gamma_{3,4}$ doublet with only a c component to the angular momentum and hence can be represented by the $\sigma^z = \pm 1$ Ising states. A transverse field in the a-b plane mixes the higher lying states with the ground state; this produces a splitting of the doublet, equivalent to an effective Ising model field. The phase diagram of LiHoF$_4$ (Fig. 1A) was determined earlier by susceptibility measurements (10) and displays a zero-field T_c of 1.53 K and a critical field of $H_c = 49.5$ kOe in the zero temperature limit. The same measurements confirmed the strong Ising anisotropy, with longitudinal and transverse g factors differing by a factor of 18 (10). The sudden increase in H_c below 400 mK was explained by alignment of the Ho nuclear moments through the hyperfine coupling. Corrections to phase diagrams as a result of hyperfine couplings have a long history (18) and were noted for the LiREF$_4$ (RE = rare earth) series, of which LiHoF$_4$ is a member, more than 20 years ago (19). What is new here is that the application of a transverse field and the use of high-resolution neutron scattering spectroscopy allow us to carefully study the dynamics as we tune through the quantum critical point (QCP).

We measured the magnetic excitation spectrum of LiHoF$_4$ with the use of the TAS7 neutron spectrometer at Risø National Laboratory, with an energy resolution (full width at half maximum) of 0.06 to 0.18 meV (20). The transverse field was aligned to better than 0.35°, and the sample was cooled in a dilution refrigerator. At the base temperature of 0.31 K, giving a critical field of 42.4 kOe, the excitation spectrum was mapped out below, at, and above the critical field (Fig. 2). For all fields, a single excitation branch disperses upward from a minimum gap at (2,0,0) toward (1,0,0). From (1,0,0) to (1,0,1), the mode shows little dispersion but appears to broaden. The discontinuity on approaching $(1,0,1 - \varepsilon)$ and $(1 + \varepsilon, 0, 1)$ as $\varepsilon \to 0$ reflects the anisotropy and long-range nature of the magnetic dipole coupling. However, the most important observation is that the (2,0,0) energy, which is always lower than the calculated single-ion energy (~ 0.39 meV at 42.4 kOe), shrinks upon increasing the field from 36 to 42.4 kOe and then hardens again at 60 kOe. At this qualitative level, what we see agrees with the mode softening predicted for the simple Ising model in a transverse field. However, it appears that the mode softening is incomplete. At the critical field of 42.4 kOe, the mode retains a finite energy of 0.24 ± 0.01 meV. This result is apparent in Fig. 1B, which shows the gap energy as a function of the external field.

To obtain a quantitative understanding of our experiments, we consider the full rare-earth Hamiltonian, which closely resembles that of


Fig. 1. (A) Phase diagram of LiHoF$_4$ as a function of transverse magnetic field and temperature from susceptibility (10) (circles) and neutron scattering (squares) measurements. Lines are $1/z$ calculations with (solid) and without (dashed) hyperfine interaction. Horizontal dashed guide marks the temperature 0.31 K at which inelastic neutron measurements were performed. (B) Field dependence of the lowest excitation energy in LiHoF$_4$ measured at $Q = (1 + \varepsilon, 0, 1)$. Lines are calculated energies scaled by $Z = 1.15$ with (solid) and without (dashed) hyperfine coupling. The dashed vertical guides show how in either case the minimum energy occurs at the field of the transition [compare with (A)]. (C) Schematic of electronic (blue) and nuclear (red) levels as the transverse field is lowered toward the QCP. Neglecting the nuclear spins, the electronic transition (light blue arrow) would soften all the way to zero energy. Hyperfine coupling creates a nondegenerate multiplet around each electronic state. The QCP now occurs when the excited-state multiplet through level repulsion squeezes the collective mode of the ground-state multiplet to zero energy, hence forestalling complete softening of the electronic mode. Of course, the true ground and excited states are collective modes of many Ho ions and should be classified in momentum space. (D) Calculated ratio of the minimum excitation energy E_c to the single-ion splitting Δ at the critical field as a function of temperature. This measures how far the electronic system is from the coherent limit, for which $E_c/\Delta = 0$.

HoF$_3$ (21, 22). Each Ho ion is subject to the crystal field, the Zeeman coupling, and the hyperfine coupling. The interaction between moments is dominated by the long-range dipole coupling, with a small nearest neighbor exchange interaction J_{12}:

$$\mathcal{H} = \sum_i \left[\mathcal{H}_{CF}(\mathbf{J}_i) + A\mathbf{J}_i \cdot \mathbf{I}_i - g\mu_B \mathbf{J}_i \cdot \mathbf{H} \right]$$
$$- \frac{1}{2} \sum_{ij} \sum_{\alpha\beta} \mathcal{J}_D D_{\alpha\beta}(ij) J_{i\alpha} J_{j\beta}$$
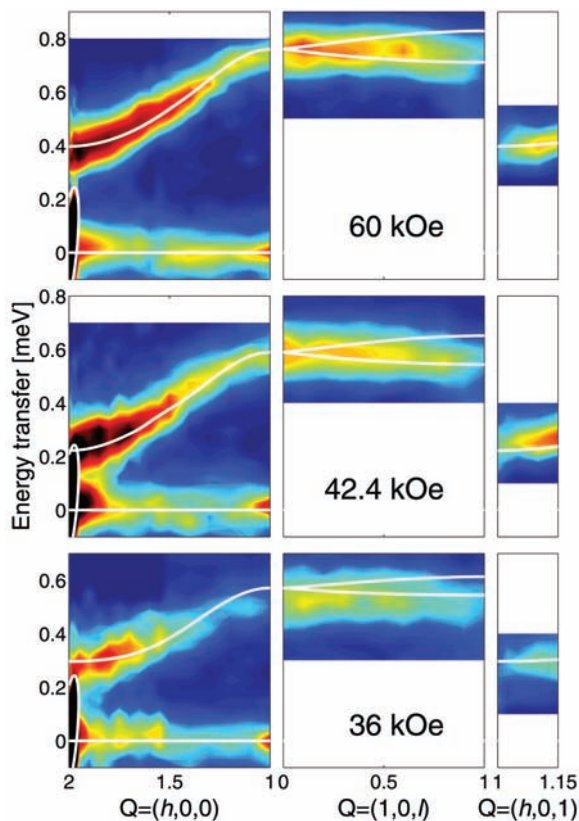$$- \frac{1}{2} \sum_{ij}^{n.n.} \mathcal{J}_{12} \, \mathbf{J}_i \cdot \mathbf{J}_j \quad (2)$$

where $\mathbf{J}$ and $\mathbf{I}$ are the electronic and nuclear moments, respectively, and for ^{165}Ho^{3+} $J = 8$ and $I = 7/2$. Hyperfine resonance (23) and heat capacity measurements (24) show the hyperfine coupling parameter $A = 3.36$ μeV as for the isolated ion, with negligible nuclear-quadrupole coupling. The Zeeman term is reduced by the demagnetization field. The normalized dipole tensor $D_{\alpha\beta}(ij)$ is directly calculable, and the dipole coupling strength J_D is simply fixed by lattice constants and the magnetic moments of the ions at $J_D = (g\mu_B)^2 N = 1.1654$ μeV, where μ_B is the Bohr magneton. This leaves as free parameters various numbers appearing in the crystal-field Hamiltonian H_{CF} and the exchange constant J_{12}. The former are determined (25) largely from electron spin resonance for dilute Ho atoms substituted for Y in LiYF$_4$, whereas the latter is constrained
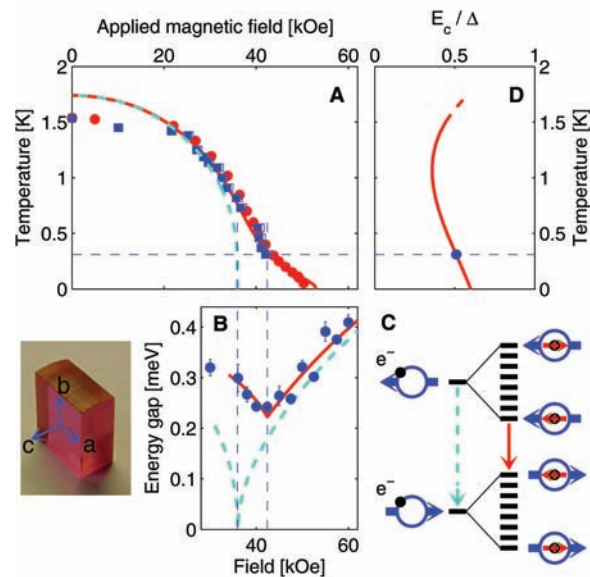
by the phase diagram determined earlier (10) (Fig. 1A). We have used an effective medium theory (9) previously applied to HoF$_3$ (26) to fit the phase diagram, and we conclude that a good overall description—except for a modest (14%) overestimate of the zero-field transition temperature—is obtained for $J_{12} = -0.1$ μeV. On the basis of quantum Monte Carlo simulation data, others (27) have also concluded that J_{12} is substantially smaller than J_D.

Having established a good parameterization of the Hamiltonian, we model the dynamics, where expansion to order $1/z$ (where z is the number of nearest neighbors of an ion in the lattice) leads to an energy-dependent renormalization $[1 + \Sigma(\omega)]^{-1}$ (on the order of 10%) of the dynamic susceptibility calculated in the random phase approximation, with the self energy $\Sigma(\omega)$ evaluated as described in (26). For the three fields investigated in detail, the dispersion measured by neutron scattering is closely reproduced throughout the Brillouin zone. As indicated by the solid lines in Fig. 2, the agreement becomes excellent if the calculated excitation energies are multiplied by a renormalization factor $Z = 1.15$. The point is not that the calculation is imperfect but rather that it matches the data as closely as it does. Indeed, it also predicts a weak mode splitting of about 0.08 meV at $(1,0,1 - \varepsilon)$, consistent with the increased width in the measurements. The agreement for the discontinuous jump between $(1,0,1 - \varepsilon)$ and $(1 + \varepsilon, 0, 1)$ as a result of the long-range nature of the dipole coupling shows that this is indeed the dominant coupling.

Fig. 2. Pseudocolor representation of the inelastic neutron scattering intensity for LiHoF$_4$ at $T = 0.31$ K observed along the reciprocal space trace $(2,0,0) \rightarrow (1,0,0) \rightarrow (1,0,1) \rightarrow (1.15,0,1)$. White lines show the $1/z$ calculation for the excitation energies as described in the text. White ellipses around the $(2,0,0)$ Bragg peak indicate 5 times the resolution tail (full width at half maximum).

Fig. 3. Measured intensities of the excitations along $Q = (h,0,0)$ at the same values of the field as in Fig. 2. Lines are calculated with geometric and resolution corrections applied to allow comparison to the neutron data.

The simple origin of the incomplete softening and enhanced critical field (Fig. 1, B and C) is easiest to understand if we start from the polarized paramagnetic state above H_c, where the experiment, the purely electronic calculation, and the theory including the hyperfine coupling all coincide. At high fields, the only effect of the hyperfine term is to split both the ground state and the electronic excitation modes into multiplets that are simply the direct products of the electronic and nuclear levels, with a total span of $2A\langle J\rangle I \approx 0.1$ meV (Fig. 1C). Upon lowering the field, the electronic mode softens and would reach zero energy at $H_c^0 = 36$ kOe in the absence of hyperfine coupling. The hyperfine coupling, however, already mixes the original ground and excited (soft mode) states above H_c. As this happens, the formation of a composite spin from mixed nuclear and electronic contributions immediately stabilizes ordering along the c axis of the crystal. In other words, the hyperfine coupling shunts the electronic mode, raising the critical field to the observed $H_c = 42.4$ kOe, where the mode reaches a nonzero minimum. This process is accompanied by transfer of intensity from the magnetic excitation of electronic origin to soft modes of much lower energy (in the 10-μeV range) that have an entangled nuclear/electronic character. Cooling to very low temperatures would reveal these modes as propagating and softening to zero at the QCP, but at the temperatures

reachable in our measurements there is thermalization, dephasing the composite modes to yield the strong quasi-elastic scattering appearing around $Q = (2,0,0)$ and zero energy at the critical field, as in Fig. 2.

The intensities of the excitations are simply proportional to the matrix elements $|\langle f|\sum_j \exp(iQ \cdot R_j)J_j^+|0\rangle|^2$, and therefore provide a direct measure of the wave functions via the interference effects implicit in the spatial Fourier transform of J_j. Figure 3 shows intensities recorded along $(h,0,0)$ for the three fields 36, 42.4, and 60 kOe. They follow a momentum dependence characterized by a broad peak near $(2,0,0)$, which is well described by our theory. In the absence of hyperfine interactions, the intensity at H_c^0 would diverge as q approaches $(2,0,0)$, reflecting that the real-space dynamical coherence length ξ_c of the excited state grows to infinity. The finite width of the peak observed at H_c corresponds in real space to a distance on the order of the interholmium spacing; because the hyperfine interactions forestall the softening of the electronic mode, the implication is that these interactions also limit the distance over which the electronic wave functions can be entangled (4). Thus, Fig. 3 is a direct demonstration of the limitation of quantum coherence in space via coupling to a nuclear spin bath. ξ_c is obtained from a sum over matrix elements connecting the ground state to a particular set of excited states, whereas the thermodynamic correlation length
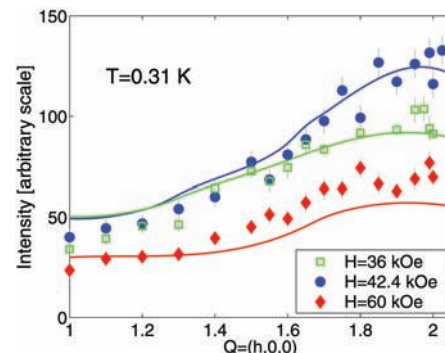
ξ_t is derived from the equal time correlation function $S(r)$, which is the sum over all final states. ξ_t diverges at second-order transitions such as those in LiHoF$_4$, where the quasielastic component seen in our data dominates the long-distance behavior of $S(r)$ at $T_c(H)$. It is the electronic mode, and hence ξ_c, that dictates to what extent LiHoF$_4$ can be characterized and potentially exploited as a realization of the ideal transverse-field Ising model.

Beyond providing a quantitative understanding of the excitations near the QCP of a model experimental system, we obtain new insight by bringing together the older knowledge from rare-earth magnetism and the contemporary ideas of entanglement, qubits, and decoherence. Although the notion of the spin bath was developed to address decoherence in localized magnetic clusters and molecules (1), our work discloses its importance for QPTs. In particular, we establish that the spin bath is a generic feature that will limit our ability to observe intrinsic electronic quantum criticality. This may not matter much for transition metal oxides with very large exchange constants, but it could matter for rare earth and actinide intermetallic compounds, which show currently unexplained crossovers to novel behaviors at low (<1 K) temperatures [see, e.g., (28)].

For magnetic clusters, decoherence can be minimized in a window between the oscillator bath–dominated high-temperature regions and the spin bath–dominated low-temperature regions (29). Our calculations suggest that the dense quantum critical magnet shows analogous behavior. Here the interacting electron spins themselves constitute the oscillator bath, and the extent to which the magnetic excitation softens at $T_c(H)$, as measured by the ratio of the zone center energy E_c to the field-induced single-ion splitting Δ (Fig. 1D), gauges the electronic decoherence. E_c/Δ achieves its minimum not at $T = 0$ but rather at an intermediate temperature $T \approx 1$ K, exactly where the phase boundary in Fig. 1A begins to be affected by the nuclear hyperfine interactions.

References and Notes

1. N. V. Prokof'ev, P. C. E. Stamp, *Rep. Prog. Phys.* **63**, 669 (2000).
2. R. P. Feynman, F. L. Vernon, *Ann. Phys.* **24**, 118 (1963).
3. W. Wernsdorfer, S. Bhaduri, R. Tiron, D. N. Hendrickson, G. Christou, *Phys. Rev. Lett.* **89**, 197201 (2002).
4. A. Osterloh, L. Amico, G. Falci, R. Fazio, *Nature* **416**, 608 (2002).
5. S. Sachdev, *Phys. World* **12**, 33 (1999).
6. S. Sachdev, *Quantum Phase Transitions* (Cambridge Univ. Press, Cambridge, 1999).
7. P. G. de Gennes, *Solid State Commun.* **1**, 132 (1963).
8. R. J. Elliott, P. Pfeuty, C. Wood, *Phys. Rev. Lett.* **25**, 443 (1970).
9. R. B. Stinchcombe, *J. Phys. C* **6**, 2459 and 2484 (1973).
10. D. Bitko, T. F. Rosenbaum, G. Aeppli, *Phys. Rev. Lett.* **77**, 940 (1997).
11. T. F. Rosenbaum et al., *J. Appl. Phys.* **70**, 5946 (1991).
12. D. Bitko, thesis, University of Chicago (1997).
13. R. Giraud et al., *Phys. Rev. Lett.* **87**, 057203 (2001).
14. J. Brooke, D. Bitko, T. F. Rosenbaum, G. Aeppli, *Science* **284**, 779 (1999).
15. J. Brooke, T. F. Rosenbaum, G. Aeppli, *Nature* **413**, 610 (2001).
16. S. Ghosh, R. Parthasarathy, T. F. Rosenbaum, G. Aeppli, *Science* **296**, 2195 (2002).
17. S. Ghosh et al., *Nature* **425**, 48 (2003).
18. K. Andres, *Phys. Rev. B* **7**, 4295 (1973).
19. R. W. Youngblood, G. Aeppli, J. D. Axe, J. A. Griffin, *Phys. Rev. Lett.* **49**, 1724 (1982).
20. H. M. Rønnow, thesis, Risø National Laboratory, Denmark (2000).
21. M. J. M. Leask et al., *J. Phys. C* **6**, 505 (1994).
22. A. P. Ramirez, J. Jensen, *J. Phys. C* **6**, L215 (1994).
23. J. Magariño, J. Tuchendler, P. Beauvillain, I. Laursen, *Phys. Rev. B* **21**, 18 (1980).
24. G. Mennenga, L. J. de Jongh, W. J. Huiskamp, *J. Magn. Magn. Mater.* **44**, 59 (1984).
25. H. M. Rønnow et al., in preparation.
26. J. Jensen, *Phys. Rev. B* **49**, 11833 (1994).
27. P. B. Chakraborty, P. Henelius, H. Kjønsberg, A. W. Sandvik, S. M. Girvin, *Phys. Rev. B* **70**, 144411 (2004).
28. P. Gegenwart et al., *Phys. Rev. Lett.* **89**, 056402 (2002).
29. P. C. E. Stamp, I. S. Tupitsyn, *Phys. Rev. B* **69**, 014401 (2004).
30. We thank G. McIntyre for his expert assistance during complementary measurements on the D10 diffractometer at the Institut Laue Langevin, Grenoble, France. Work at the University of Chicago was supported by NSF Materials Research Science and Engineering Centers grant DMR-0213745. Work in London was supported by the Wolfson–Royal Society Research Merit Award Program and the Basic Technologies program of the UK Research Councils.

Atomic-Scale Visualization of Inertial Dynamics

A. M. Lindenberg,[1] J. Larsson,[2] K. Sokolowski-Tinten,[3] K. J. Gaffney,[1] C. Blome,[4] O. Synnergren,[2] J. Sheppard,[5] C. Caleman,[6] A. G. MacPhee,[7] D. Weinstein,[7] D. P. Lowney,[7] T. K. Allison,[7] T. Matthews,[7] R. W. Falcone,[7] A. L. Cavalieri,[8] D. M. Fritz,[8] S. H. Lee,[8] P. H. Bucksbaum,[8] D. A. Reis,[8] J. Rudati,[9] P. H. Fuoss,[10] C. C. Kao,[11] D. P. Siddons,[11] R. Pahl,[12] J. Als-Nielsen,[13] S. Duesterer,[4] R. Ischebeck,[4] H. Schlarb,[4] H. Schulte-Schrepping,[4] Th. Tschentscher,[4] J. Schneider,[4] D. von der Linde,[14] O. Hignette,[15] F. Sette,[15] H. N. Chapman,[16] R. W. Lee,[16] T. N. Hansen,[2] S. Techert,[17] J. S. Wark,[5] M. Bergh,[6] G. Huldt,[6] D. van der Spoel,[6] N. Timneanu,[6] J. Hajdu,[6] R. A. Akre,[18] E. Bong,[18] P. Krejcik,[18] J. Arthur,[1] S. Brennan,[1] K. Luening,[1] J. B. Hastings[1]

The motion of atoms on interatomic potential energy surfaces is fundamental to the dynamics of liquids and solids. An accelerator-based source of femtosecond x-ray pulses allowed us to follow directly atomic displacements on an optically modified energy landscape, leading eventually to the transition from crystalline solid to disordered liquid. We show that, to first order in time, the dynamics are inertial, and we place constraints on the shape and curvature of the transition-state potential energy surface. Our measurements point toward analogies between this nonequilibrium phase transition and the short-time dynamics intrinsic to equilibrium liquids.

In a crystal at room temperature, vibrational excitations, or phonons, only slightly perturb the crystalline order. In contrast, liquids explore a wide range of configurations set by the topology of a complex and time-dependent potential energy surface (*1*, *2*). By using light to trigger changes in this energy landscape, well-defined initial and final states can be generated to which a full range of time-resolved techniques may be applied. In particular, light-induced structural transitions between the crystalline and liquid states of matter may act as simple models for dynamics intrinsic to the liquid state or to transition states in general (*3*).

In this context, a new class of nonthermal processes governing the ultrafast solid-liquid melting transition has recently emerged, supported by time-resolved optical (*4–7*) and x-ray (*8–10*) experiments and with technological applications ranging from micromachining to eye surgery (*11*). Intense femtosecond excitation of semiconductor materials results in the excitation of a dense electron-hole plasma, with accompanying dramatic changes in the interatomic potential (*12–14*). At sufficiently high levels of excitation, it is thought that this process leads to disordering of the crystalline lattice on time scales faster than the time scale for thermal equilibration [often known as the electron-phonon coupling time, on the order of a few picoseconds (*15*)]. In a pioneering study, Rousse et al. (*9*) determined that the structure of indium antimonide (InSb) changes on sub-picosecond time scales, but the mechanism by which this occurs and the

microscopic pathways the atoms follow have remained elusive, in part because of uncertainties in the pulse duration of laser-plasma sources and signal-to-noise limitations.

Research and development efforts leading toward the Linac Coherent Light Source (LCLS) free-electron laser have facilitated the construction of a new accelerator-based x-ray source, the Sub-Picosecond Pulse Source (SPPS), which uses the same linac-based acceleration and electron bunch compression schemes to be used at future free-electron lasers (*16*, *17*). In order to produce femtosecond x-ray bursts, electron bunches at the Stanford Linear Accelerator Center (SLAC) are chirped and then sent through a series of energy-dispersive magnetic chicanes to create 80-fs electron pulses. These pulses are then transported through an undulator to create sub-100-femtosecond x-ray pulses (*18*). In order to overcome the intrinsic jitter between x-rays and a Ti:sapphire-based femtosecond laser

[1]Stanford Synchrotron Radiation Laboratory/Stanford Linear Accelerator Center (SLAC), Menlo Park, CA 94025, USA. [2]Department of Physics, Lund Institute of Technology, Post Office Box 118, S-22100, Lund, Sweden. [3]Institut für Optik und Quantenelektronik, Friedrich-Schiller Universität Jena, Max-Wien-Platz 1, 07743 Jena, Germany. [4]Deutsches Elektronen-Synchrotron DESY, Notkestrasse 85, 22607 Hamburg, Germany. [5]Department of Physics, Clarendon Laboratory, Parks Road, University of Oxford, Oxford OX1 3PU, UK. [6]Department of Cell and Molecular Biology, Biomedical Centre, Uppsala University, SE-75124 Uppsala, Sweden. [7]Department of Physics, University of California, Berkeley, CA 94720, USA. [8]FOCUS (Frontiers in Optical Coherent and Ultrafast Science) Center, Department of Physics and Applied Physics Program, University of Michigan, Ann Arbor, MI 48109, USA. [9]Advanced Photon Source, [10]Materials Science Division, Argonne National Laboratory, Argonne, IL 60439, USA. [11]National Synchrotron Light Source, Brookhaven National Laboratory, Upton, NY 11973, USA. [12]Consortium for Advanced Radiation Sources, University of Chicago, Chicago, IL 60637, USA. [13]Niels Bohr Institute, Copenhagen University, 2100 Copenhagen Ø, Denmark. [14]Institut für Experimentelle Physik, Universität Duisburg-Essen, D-45117 Essen, Germany. [15]European Synchrotron Radiation Facility, 38043 Grenoble Cedex 9, France. [16]Physics Department, Lawrence Livermore National Laboratory, Livermore, CA 94550, USA. [17]Max Plank Institute for Biophysical Chemistry, Am Faßberg 11, 37077 Göttingen, Germany. [18]SLAC, Menlo Park, CA 94025, USA.

A silicon-based nuclear spin quantum computer

B. E. Kane

Semiconductor Nanofabrication Facility, School of Physics, University of New South Wales, Sydney 2052, Australia

Quantum computers promise to exceed the computational efficiency of ordinary classical machines because quantum algorithms allow the execution of certain tasks in fewer steps. But practical implementation of these machines poses a formidable challenge. Here I present a scheme for implementing a quantum-mechanical computer. Information is encoded onto the nuclear spins of donor atoms in doped silicon electronic devices. Logical operations on individual spins are performed using externally applied electric fields, and spin measurements are made using currents of spin-polarized electrons. The realization of such a computer is dependent on future refinements of conventional silicon electronics.

Although the concept of information underlying all modern computer technology is essentially classical, phsyicists know that nature obeys the laws of quantum mechanics. The idea of a quantum computer has been developed theoretically over several decades to elucidate fundamental questions concerning the capabilities and limitations of machines in which information is treated quantum mechanically[1,2]. Specifically, in quantum computers the ones and zeros of classical digital computers are replaced by the quantum state of a two-level system (a qubit). Logical operations carried out on the qubits and their measurement to determine the result of the computation must obey quantum-mechanical laws. Quantum computation can in principle only occur in systems that are almost completely isolated from their environment and which consequently must dissipate no energy during the process of computation, conditions that are extraordinarily difficult to fulfil in practice.

Interest in quantum computation has increased dramatically in the past four years because of two important insights: first, quantum algorithms (most notably for prime factorization[3,4] and for exhaustive search[5]) have been developed that outperform the best known algorithms doing the same tasks on a classical computer. These algorithms require that the internal state of the quantum computer be controlled with extraordinary precision, so that the coherent quantum state upon which the quantum algorithms rely is not destroyed. Because completely preventing decoherence (uncontrolled interaction of a quantum system with its surrounding environment) is impossible, the existence of quantum algorithms does not prove that they can ever be implemented in a real machine.

The second critical insight has been the discovery of quantum error-correcting codes that enable quantum computers to operate despite some degree of decoherence and which may make quantum computers experimentally realizable[6,7]. The tasks that lie ahead to create an actual quantum computer are formidable: Preskill[8] has estimated that a quantum computer operating on 10^6 qubits with a 10^{-6} probability of error in each operation would exceed the capabilities of contemporary conventional computers on the prime factorization problem. To make use of error-correcting codes, logical operations and measurement must be able to proceed in parallel on qubits throughout the computer.

The states of spin 1/2 particles are two-level systems that can potentially be used for quantum computation. Nuclear spins have been incorporated into several quantum computer proposals[9–12] because they are extremely well isolated from their environment and so operations on nuclear spin qubits could have low error rates. The primary challenge in using nuclear spins in quantum computers lies in measuring the spins. The bulk spin resonance approach

to quantum computation[11,12] circumvents the single-spin detection problem essentially by performing quantum calculations in parallel in a large number of molecules and determining the result from macroscopic magnetization measurements. The measurable signal decreases with the number of qubits, however, and scaling this approach above about ten qubits will be technically demanding[37].

To attain the goal of a 10^6 qubit quantum computer, it has been suggested that a 'solid state' approach[13] might eventually replicate the enormous success of modern electronics fabrication technology. An attractive alternative approach to nuclear spin quantum computation is to incorporate nuclear spins into an electronic device and to detect the spins and control their interactions electronically[14]. Electron and nuclear spins are coupled by the hyperfine interaction[15]. Under appropriate circumstances, polarization is transferred between the two spin systems and nuclear spin polarization is detectable by its effect on the electronic properties of a sample[16,17]. Electronic devices for both generating and detecting nuclear spin polarization, implemented at low temperatures in GaAs/Al_xGa_{1-x}As heterostructures, have been developed[18], and similar devices have been incorporated into nanostructures[19,20]. Although the number of spins probed in the nanostructure experiments is still large ($\sim 10^{11}$; ref. 19), sensitivity will improve in optimized devices and in systems with larger hyperfine interactions.

Here I present a scheme for implementing a quantum computer on an array of nuclear spins located on donors in silicon, the semiconductor used in most conventional computer electronics. Logical operations and measurements can in principle be performed independently and in parallel on each spin in the array. I describe specific electronic devices for the manipulation and measurement of nuclear spins, fabrication of which will require significant advances in the rapidly moving field of nanotechnology. Although it is likely that scaling the devices proposed here into a computer of the size envisaged by Preskill[8] will be an extraordinary challenge, a silicon-based quantum computer is in a unique position to benefit from the resources and ingenuity being directed towards making conventional electronics of ever smaller size and greater complexity.

Quantum computation with a ^{31}P array in silicon

The strength of the hyperfine interaction is proportional to the probability density of the electron wavefunction at the nucleus. In semiconductors, the electron wavefunction extends over large distances through the crystal lattice. Two nuclear spins can consequently interact with the same electron, leading to electron-mediated or indirect nuclear spin coupling[15]. Because the electron is sensitive to externally applied electric fields, the hyperfine inter-

action and electron-mediated nuclear spin interaction can be controlled by voltages applied to metallic gates in a semiconductor device, enabling the external manipulation of nuclear spin dynamics that is necessary for quantum computation.

The conditions required for electron-coupled nuclear spin computation and single nuclear spin detection can arise if the nuclear spin is located on a positively charged donor in a semiconductor host. The electron wavefunction is then concentrated at the donor nucleus (for s orbitals and energy bands composed primarily of them), yielding a large hyperfine interaction energy. For shallow-level donors, however, the electron wavefunction extends tens or hundreds of ångströms away from the donor nucleus, allowing electron-mediated nuclear spin coupling to occur over comparable distances. The quantum computer proposed here comprises an array of such donors positioned beneath the surface of a semiconductor host (Fig. 1). A quantum mechanical calculation proceeds by the precise control of three external parameters: (1) gates above the donors control the strength of the hyperfine interactions and hence the resonance frequency of the nuclear spins beneath them; (2) gates between the donors turn on and off electron-mediated coupling between the nuclear spins[13]; (3) a globally applied a.c. magnetic field B_{ac} flips nuclear spins at resonance. Custom adjustment of the coupling of each spin to its neighbours and to B_{ac} enables different operations to be performed on each of the spins simultaneously. Finally, measurements are performed by transferring nuclear spin polarization to the electrons and determining the electron spin state by its effect on the orbital wavefunction of the electrons, which can be probed using capacitance measurements between adjacent gates.

An important requirement for a quantum computer is to isolate the qubits from any degrees of freedom that may lead to decoherence. If the qubits are spins on a donor in a semiconductor, nuclear spins in the host are a large reservoir with which the donor spins can interact. Consequently, the host should contain only nuclei with spin $I = 0$. This simple requirement unfortunately eliminates all III–V semiconductors as host candidates, because none of their constituent elements possesses stable $I = 0$ isotopes[21]. Group IV semiconductors are composed primarily $I = 0$ isotopes and can in principle be purified to contain only $I = 0$ isotopes. Because of the

advanced state of Si materials technology and the tremendous effort currently underway in Si nanofabrication, Si is the obvious choice for the semiconductor host.

The only $I = 1/2$ shallow (group V) donor in Si is ^{31}P. The Si:^{31}P system was exhaustively studied 40 years ago in the first electron–nuclear double-resonance experiments[22,23]. At sufficiently low ^{31}P concentrations at temperature $T = 1.5$ K, the electron spin relaxation time is thousands of seconds and the ^{31}P nuclear spin relaxation time exceeds 10 hours. It is likely that at millikelvin temperatures the phonon limited ^{31}P relaxation time is of the order of 10^{18} seconds (ref. 24), making this system ideal for quantum computation.

The purpose of the electrons in the computer is to mediate nuclear spin interactions and to facilitate measurement of the nuclear spins. Irreversible interactions between electron and nuclear spins must not occur as the computation proceeds: the electrons must be in a non-degenerate ground state throughout the computation. At sufficiently low temperatures, electrons only occupy the lowest energy-bound state at the donor, whose twofold spin degeneracy is broken by an applied magnetic field B. (The valley degeneracy of the Si conduction band is broken in the vicinity of the donor[25]. The lowest donor excited state is approximately 15 meV above the ground state[23].) The electrons will only occupy the lowest energy spin level when $2\mu_B B \gg kT$, where μ_B is the Bohr magneton. (In Si, the Landé g-factor is very close to $+2$, so $g = 2$ is used throughout this discussion.) The electrons will be completely spin-polarized ($n_\uparrow/n_\downarrow < 10^{-6}$) when $T \leq 100$ mK and $B \geq 2$ tesla. A quantum-mechanical computer is non-dissipative and can consequently operate at low temperatures. Dissipation will arise external to the computer from gate biasing and from eddy currents caused by B_{ac}, and during polarization and measurement of the nuclear spins. These effects will determine the minimum operable temperature of the computer. For this discussion, I will assume $T = 100$ mK and $B = 2$ T. Note that these conditions do not fully polarize the nuclear spins, which are instead aligned by interactions with the polarized electrons.

Magnitude of spin interactions in Si:^{31}P

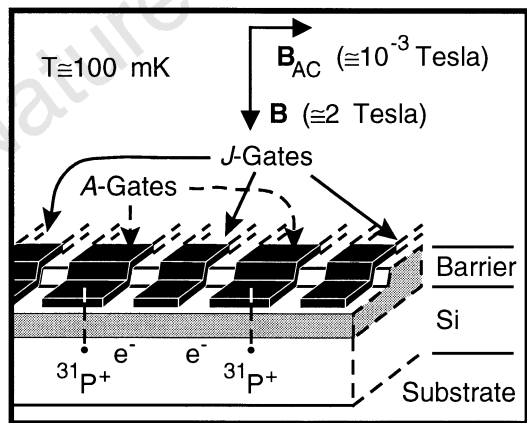The size of the interactions between spins determines both the time

Figure 1 Illustration of two cells in a one-dimensional array containing ^{31}P donors and electrons in a Si host, separated by a barrier from metal gates on the surface. 'A gates' control the resonance frequency of the nuclear spin qubits; 'J gates' control the electron-mediated coupling between adjacent nuclear spins. The ledge over which the gates cross localizes the gate electric field in the vicinity of the donors.
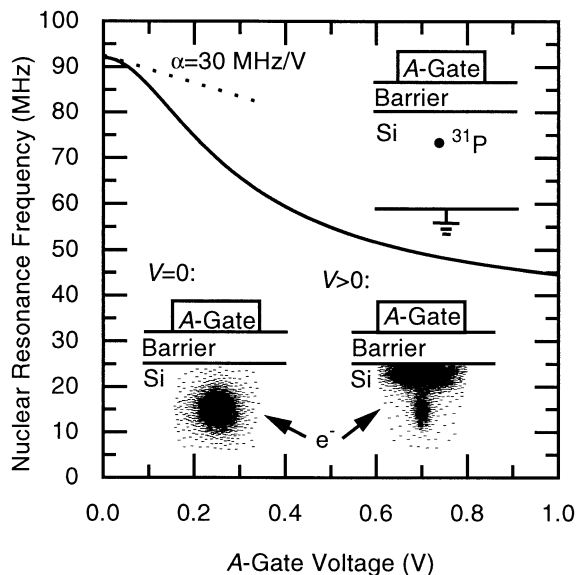

Figure 2 An electric field applied to an A gate pulls the electron wavefunction away from the donor and towards the barrier, reducing the hyperfine interaction and the resonance frequency of the nucleus. The donor nucleus–electron system is a voltage-controlled oscillator with a tuning parameter α of the order of 30 MHz V^{-1}.

required to do elementary operations on the qubits and the separation necessary between donors in the array. The hamiltonian for a nuclear spin–electron system in Si, applicable for an $I = 1/2$ donor nucleus and with $B\|z$ is $H_{en} = \mu_B B\sigma_z^e - g_n\mu_n B\sigma_z^n + A\sigma^e\cdot\sigma^n$, where σ are the Pauli spin matrices (with eigenvalues ± 1), μ_n is the nuclear magneton, g_n is the nuclear g-factor (1.13 for ^{31}P; ref. 21), and $A = \frac{8}{3}\pi\mu_B g_n\mu_n|\Psi(0)|^2$ is the contact hyperfine interaction energy, with $|\Psi(0)|^2$, the probability density of the electron wavefunction, evaluated at the nucleus. If the electron is in its ground state, the frequency separation of the nuclear levels is, to second order

$$h\nu_A = 2g_n\mu_n B + 2A + \frac{2A^2}{\mu_B B} \tag{1}$$

In Si:[31]P, $2A/h = 58$ MHz, and the second term in equation (1) exceeds the first term for $B < 3.5$ T.

An electric field applied to the electron-donor system shifts the electron wavefunction envelope away from the nucleus and reduces the hyperfine interaction. The size of this shift, following estimates of Kohn[25] of shallow donor Stark shifts in Si, is shown in Fig. 2 for a donor 200 Å beneath a gate. A donor nuclear spin–electron system close to an 'A gate' functions as a voltage-controlled oscillator: the precession frequency of the nuclear spin is controllable externally, and spins can be selectively brought into resonance with B_{ac}, allowing arbitrary rotations to be performed on each nuclear spin.

Quantum mechanical computation requires, in addition to single spin rotations, the two-qubit 'controlled rotation' operation, which rotates the spin of a target qubit through a prescribed angle if, and only if, the control qubit is oriented in a specified direction, and leaves the orientation of the control qubit unchanged[26,27]. Performing the controlled rotation operation requires nuclear-spin exchange between two donor nucleus-electron spin systems[13], which will arise from electron-mediated interactions when the donors are sufficiently close to each other. The hamiltonian of two coupled donor nucleus–electron systems, valid at energy scales small compared to the donor-electron binding energy, is $H = H(B) + A_1\sigma^{1n}\cdot\sigma^{2e} + A_2\sigma^{2n}\cdot\sigma^{2e} + J\sigma^{1e}\cdot\sigma^{2e}$, where $H(B)$ are the magnetic field interaction terms for the spins. A_1 and A_2 are the hyperfine interaction energies of the respective nucleus–electron systems. $4J$, the exchange energy, depends on the overlap of the electron wavefunctions. For well separated donors[28]

$$4J(r) \cong 1.6\frac{e^2}{\epsilon a_B}\left(\frac{r}{a_B}\right)^{\frac{5}{2}}\exp\left(\frac{-2r}{a_B}\right) \tag{2}$$

where r is the distance between donors, ϵ is the dielectric constant of the semiconductor, and a_B is the semiconductor Bohr radius. This function, with values appropriate for Si, is plotted in Fig. 3. Equation (2), originally derived for H atoms, is complicated in Si by its valley degenerate anisotropic band structure[29]. Exchange coupling terms from each valley interfere, leading to oscillatory behaviour of $J(r)$. In this discussion, the complications introduced by Si band structure will be neglected. In determining $J(r)$ in Fig. 3, the transverse mass for Si ($\cong 0.2m_e$) has been used, and $a_B = 30$ Å. Because J is proportional to the electron wave function overlap, it can be varied by an electrostatic potential imposed by a 'J-gate' positioned between the donors[13]. As shall be seen below, significant coupling between nuclei will occur when $4J \approx \mu_B B$, and this condition approximates the necessary separation between donors of 100–200 Å. Whereas actual separations may be considerably larger than this value because the J gate can be biased positively to reduce the barrier between donors, the gate sizes required for the quantum computer are near the limit of current electronics fabrication technology.

For two-electron systems, the exchange interaction lowers the electron singlet ($|\uparrow\downarrow - \downarrow\uparrow\rangle$) energy with respect to the triplets[30]. (The $|\uparrow\downarrow\rangle$ notation is used here to represent the electron spin state,

and the $|01\rangle$ notation the nuclear state; in the $|\downarrow\downarrow 11\rangle$ state, all spins point in the same direction. For simplicity, normalization constants are omitted.) In a magnetic field, however, $|\downarrow\downarrow\rangle$ will be the electron ground state if $J < \mu_B B/2$ (Fig. 4a). In the $|\downarrow\downarrow\rangle$ state, the energies of the nuclear states can be calculated to second order in A using perturbation theory. When $A_1 = A_2 = A$, the $|10 - 01\rangle$ state is lowered in energy with respect to $|10 + 01\rangle$ by:

$$h\nu_J = 2A^2\left(\frac{1}{\mu_B B - 2J} - \frac{1}{\mu_B B}\right) \tag{3}$$

The $|11\rangle$ state is above the $|10 + 01\rangle$ state and the $|00\rangle$ state below the $|10 - 01\rangle$ state by an energy $h\nu_A$, given in equation (1). For the Si:[31]P system at $B = 2$ T and for $4J/h = 30$ GHz, equation (3) yields $\nu_J = 75$ kHz. This nuclear spin exchange frequency approximates the rate at which binary operations can be performed on the computer (ν_J can be increased by increasing J, but at the expense of also increasing the relaxation rate of the coupled nuclear–electron spin excitations). The speed of single spin operations is determined by the size of B_{ac} and is comparable to 75 kHz when $B_{ac} = 10^{-3}$ T.

Spin measurements

Measurement of nuclear spins in the proposed quantum computer is accomplished in a two-step process: distinct nuclear spin states are adiabatically converted into states with different electron polarization, and the electron spin is determined by its effect on the symmetry of the orbital wavefunction of an exchange-coupled two-electron system. A procedure for accomplishing this conversion is shown in Fig. 4. While computation is done when $J < \mu_B B/2$ and the electrons are fully polarized, measurements are made when $J > \mu_B B/2$, and $|\uparrow\downarrow - \downarrow\uparrow\rangle$ states have the lowest energy (Fig. 4a). As the electron levels cross, the $|\downarrow\downarrow\rangle$ and $|\uparrow\downarrow - \downarrow\uparrow\rangle$ states are coupled by hyperfine interactions with the nuclei. During an adiabatic increase in J, the two lower-energy nuclear spin states at $J = 0$ evolve into $|\uparrow\downarrow - \downarrow\uparrow\rangle$ states when $J > \mu_B B/2$, whereas the two higher-energy nuclear states remain $|\downarrow\downarrow\rangle$. If, at $J = 0$, $A_1 > A_2$, the orientation of nuclear spin 1 alone will determine whether the system evolves into the $|\uparrow\downarrow - \downarrow\uparrow\rangle$ or the $|\downarrow\downarrow\rangle$ state during an adiabatic increase in J.

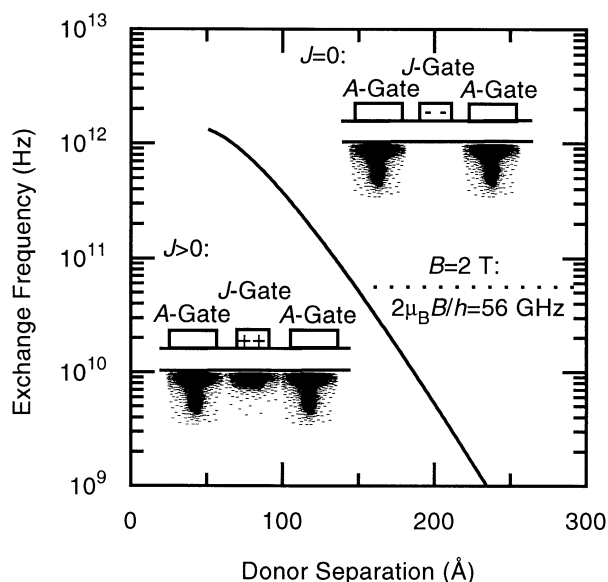A method to detect the electron spin state by using electronic

Figure 3 J gates vary the electrostatic potential barrier V between donors to enhance or reduce exchange coupling, proportional to the electron wavefunction overlap. The exchange frequency ($4J/h$) when $V = 0$ is plotted for Si.

means is shown in Fig. 4b. Both electrons can become bound to the same donor (a D^- state) if the A gates above the donors are biased appropriately. In Si:P, the D^- state is always a singlet with a second electron binding energy of 1.7 meV (refs 31, 32). Consequently, a differential voltage applied to the A gates can result in charge motion between the donors that only occurs if the electrons are in a singlet state. This charge motion is measurable using sensitive single-electron capacitance techniques[33]. This approach to spin measurement produces a signal that persists until the electron spin relaxes, a time that, as noted above, can be thousands of seconds in Si:P.

The spin measurement process can also be used to prepare nuclear spins in a prescribed state by first determining the state of a spin and flipping it if necessary so that it ends up in the desired spin state. As with the spin computation procedures already discussed, spin measurement and preparation can in principle be performed in parallel throughout the computer.

Initializing the computer

Before any computation, the computer must be initialized by calibrating the A gates and the J gates. Fluctuations from cell to cell in the gate biases necessary to perform logical operations are an inevitable consequence of variations in the positions of the donors and in the sizes of the gates. The parameters of each cell, however, can be determined individually using the measurement capabilities of the computer, because the measurement technique discussed here does not require precise knowledge of the J and A couplings. The A-gate voltage at which the underlying nuclear spin is resonant with an applied B_{ac} can be determined using the technique of adiabatic fast passage[34]: when $B_{ac} = 0$, the nuclear spin is measured and the A gate is biased at a voltage known to be off resonance. B_{ac} is then switched on, and the A gate bias is swept through a prescribed
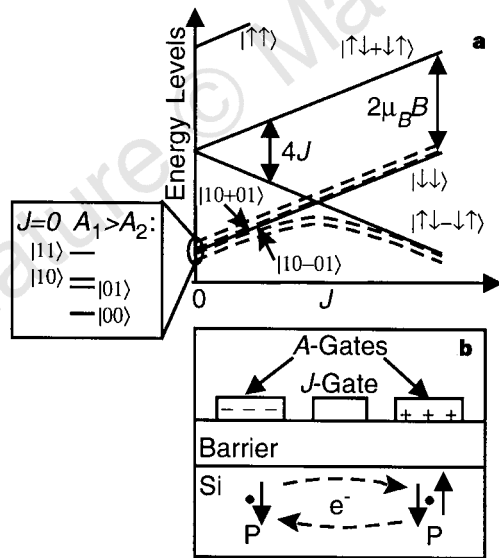

Figure 4 Two qubit quantum logic and spin measurement. **a**, Electron (solid lines) and lowest energy-coupled electron-nuclear (dashed lines) energy levels as a function of J. When $J < \mu_B B/2$, two qubit computations are performed by controlling the $|10 - 01\rangle - |10 + 01\rangle$ level splitting with a J gate. Above $J = \mu_B B/2$, the states of the coupled system evolve into states of differing electron polarization. The state of the nucleus at $J = 0$ with the larger energy splitting (controllable by the A gate bias) determines the final electron spin state after an adiabatic increase in J. **b**, Only $|\uparrow\downarrow - \downarrow\uparrow\rangle$ electrons can make transitions into states in which electrons are bound to the same donor (D^- states). Electron current during these transitions is measurable using capacitive techniques, enabling the underlying spin states of the electrons and nuclei to be determined.

voltage interval. B_{ac} is then switched off and the nuclear spin is measured again. The spin will have flipped if, and only if, resonance occurred within the prescribed A-gate voltage range. Testing for spin flips in increasingly small voltage ranges leads to the determination of the resonance voltage. Once adjacent A gates have been calibrated, the J gates can be calibrated in a similar manner by sweeping J-gate biases across resonances of two coupled cells.

This calibration procedure can be performed in parallel on many cells, so calibration is not a fundamental impediment to scaling the computer to large sizes. Calibration voltages can be stored on capacitors located on the Si chip adjacent to the quantum computer. External controlling circuitry would thus need to control only the timing of gate biases, and not their magnitudes.

Spin decoherence introduced by gates

In the quantum computer architecture outlined above, biasing of A gates and J gates enables custom control of the qubits and their mutual interactions. The presence of the gates, however, will lead to decoherence of the spins if the gate biases fluctuate away from their desired values. These effects need to be considered to evaluate the performance of any gate-controlled quantum computer. During the computation, the largest source of decoherence is likely to arise from voltage fluctuations on the A gates. (When $J < \mu_B B/2$, modulation of the state energies by the J gates is much smaller than by the A gates. J exceeds $\mu_B B/2$ only during the measurement process, when decoherence will inevitably occur.) The precession frequencies of two spins in phase at $t = 0$ depends on the potentials on their respective A gates. Differential fluctuations of the potentials produce differences in the precession frequency. At some later time $t = t_\phi$, the spins will be 180° out of phase; t_ϕ can be estimated by determining the transition rate between $|10 + 01\rangle$ (spins in phase) and $|10 - 01\rangle$ (spins 180° out of phase) of a two-spin system. The hamiltonian that couples these states is $H_\phi = \frac{1}{4}h\Delta(\sigma_z^{1n} - \sigma_z^{2n})$, where Δ is the fluctuating differential precession frequency of the spins. Standard treatment of fluctuating hamiltonians[34] predicts: $t_\phi^{-1} = \pi^2 S_\Delta(\nu_{st})$, where S_Δ is the spectral density of the frequency fluctuations, and ν_{st} is the frequency difference between the $|10 - 01\rangle$ and $|10 + 01\rangle$ states. At a particular bias voltage, the A gates have a frequency tuning parameter $\alpha = d\Delta/dV$. Thus:

$$t_\phi^{-1} = \pi^2 \alpha^2(V) S_V(\nu_{st}) \tag{4}$$

where S_V is the spectral density of the gate voltage fluctuations.

S_V for good room temperature electronics is of order 10^{-18} V^2/Hz, comparable to the room temperature Johnson noise of a 50-Ω resistor. The value of α, estimated from Fig. 2, is 10–100 MHz V^{-1}, yielding $t_\phi = 10$–1,000 s; α is determined by the size of the donor array cells and cannot readily be reduced (to increase t_ϕ) without reducing the exchange interaction between cells. Because α is a function of the gate bias (Fig. 2), t_ϕ can be increased by minimizing the voltage applied to the A gates.

Although equation (4) is valid for white noise, at low frequencies it is likely that materials-dependent fluctuations ($1/f$ noise) will be the dominant cause of spin dephasing. Consequently, it is difficult to give hard estimates of t_ϕ for the computer. Charge fluctuations within the computer (arising from fluctuating occupancies of traps and surface states, for example) are likely to be particularly important, and minimizing them will place great demands on computer fabrication.

Although materials-dependent fluctuations are difficult to estimate, the low-temperature operations of the computer and the dissipationless nature of quantum computing mean that, in principle, fluctuations can be kept extremely small: using low-temperature electronics to bias the gates (for instance, by using on chip capacitors as discussed above) could produce $t_\phi \approx 10^6$ s. Electronically controlled nuclear spin quantum computers thus have the theoretical capability to perform at least 10^5 to perhaps 10^{10}

logical operations during t_ϕ, and can probably meet Preskill's criterion[8] for an error probability of 10^{-6} per qubit operation.

Constructing the computer

Building the computer presented here will obviously be an extraordinary challenge: the materials must be almost completely free of spin ($I \neq 0$ isotopes) and charge impurities to prevent dephasing fluctuations from arising within the computer. Donors must be introduced into the material in an ordered array hundreds of Å beneath the surface. Finally, gates with lateral dimensions and separations ~ 100 Å must be patterned on the surface, registered to the donors beneath them. Although it is possible that the computer can use SiO_2 as the barrier material (the standard MOS technology used in most current conventional electronics), the need to reduce disorder and fluctuations to a minimum means that heteroepitaxial materials, such as Si/SiGe, may ultimately be preferable to Si/SiO$_2$.

The most obvious obstacle to building to the quantum computer presented above is the incorporation of the donor array into the Si layer beneath the barrier layer. Currently, semiconductor structures are deposited layer by layer. The δ-doping technique produces donors lying on a plane in the material, with the donors randomly distributed within the plane. The quantum computer envisaged here requires that the donors be placed into an ordered one- or two-dimensional array; furthermore, precisely one donor must be placed into each array cell, making it extremely difficult to create the array by using lithography and ion implantation or by focused deposition. Methods currently under development to place single atoms on surfaces using ultra-high-vacuum scanning tunnelling microscopy[35] or atom optics techniques[36] are likely candidates to be used to position the donor array. A challenge will be to grow high-quality Si layers on the surface subsequent to placement of the donors.

Fabricating large arrays of donors may prove to be difficult, but two-spin devices, which can be used to test the logical operations and measurement techniques presented here, can be made using random doping techniques. Although only a small fraction of such devices will work properly, adjacent conventional Si electronic multiplexing circuitry can be used to examine many devices separately. The relative ease of fabricating such 'hybrid' (quantum-conventional) circuits is a particularly attractive feature of Si-based quantum computation.

In a Si-based nuclear spin quantum computer, the highly coherent quantum states necessary for quantum computation are incorporated into a material in which the ability to implement complex computer architectures is well established. The substantial challenges facing the realization of the computer, particularly in fabricating 100-Å-scale gated devices, are similar to those facing the next generation of conventional electronics; consequently, new manufacturing technologies being developed for conventional electronics will bear directly on efforts to develop a quantum computer in Si. Quantum computers sufficiently complex that they can achieve their theoretical potential may thus one day be built using the same technology that is used to produce conventional computers.   □

1. Steane, A. Quantum computing. *Rep. Prog. Phys.* **61,** 117–173 (1998).
2. Bennett, C. H. Quantum information and computation. *Physics Today* 24–30 (Oct. 1995).
3. Shor, P. W. in *Proc. 35th Annu. Symp. Foundations of Computer Science* (ed. Goldwasser, S.) 124–134 (IEEE Computer Society, Los Alamitos, CA, 1994).
4. Ekert, A. & Jozsa, R. Quantum computation and Shor's factoring algorithm. *Rev. Mod. Phys.* **68,** 733–753 (1996).
5. Grover, L. K. Quantum mechanics helps in searching for a needle in a haystack. *Phys. Rev. Lett.* **79,** 325–328 (1997).
6. Calderbank, A. R. & Shor, P. W. Good quantum error correcting codes exist. *Phys. Rev. A* **54,** 1098–1105 (1996).
7. Steane, A. M. Error correcting codes in quantum theory. *Phys. Rev. Lett.* **77,** 793–797 (1996).
8. Preskill, J. Reliable quantum computers. *Proc. R. Soc. Lond. A* **454,** 385–410 (1998).
9. Lloyd, S. A potentially realizable quantum computer. *Science* **261,** 1569–1571 (1993).
10. DiVincenzo, D. P. Quantum computation. *Science* **270,** 255–261 (1995).
11. Gershenfeld, N. A. & Chuang, I. L. Bulk spin-resonance quantum computation. *Science* **275,** 350–356 (1997).
12. Cory, D. G., Fahmy, A. F. & Havel, T. F. Ensemble quantum computing by NMR spectroscopy. *Proc. Natl Acad. Sci. USA* **94,** 1634–1639 (1997).
13. Loss, D. & DiVincenzo, D. P. Quantum computation with quantum dots. *Phys. Rev. A* **57,** 120–126 (1998).
14. Privman, V., Vagner, I. D. & Kventsel, G. Quantum computation in quantum Hall systems. *Phys. Lett. A* **239,** 141–146 (1998)..
15. Slichter, C. P. *Principles of Magnetic Resonance* 3rd edn, Ch 4 (Springer, Berlin, 1990).
16. Dobers, M., Klitzing, K. v., Schneider, J., Weimann, G. & Ploog, K. Electrical detection of nuclear magnetic resonance in GaAs-Al$_x$Ga$_{1-x}$As heterostructures. *Phys. Rev. Lett.* **61,** 1650–1653 (1988).
17. Stich, B., Greulich-Weber, S. & Spaeth, J.-M. Electrical detection of electron nuclear double resonance in silicon. *Appl. Phys. Lett.* **68,** 1102–1104 (1996).
18. Kane, B. E., Pfeiffer, L. N. & West, K. W. Evidence for an electric-field-induced phase transition in a spin-polarized two-dimensional electron gas. *Phys. Rev. B* **46,** 7264–7267 (1992).
19. Wald, K. W., Kouwenhoven, L. P., McEuen, P. L., van der Vaart, N. C. & Foxon, C. T. Local dynamic nuclear polarization using quantum point contacts. *Phys. Rev. Lett.* **73,** 1011–1014 (1994).
20. Dixon, D. C., Wald, K. R., McEuen, P. L. & Melloch, M. R. Dynamic polarization at the edge of a two-dimensional electron gas. *Phys. Rev. B* **56,** 4743–4750 (1997).
21. *CRC Handbook of Chemistry and Physics* 77th edn 11–38 (CRC Press, Boca Raton, Florida, 1996).
22. Feher, G. Electron spin resonance on donors in silicon. I. Electronic structure of donors by the electron nuclear double resonance technique. *Phys. Rev.* **114,** 1219–1244 (1959).
23. Wilson, D. K. & Feher, G. Electron spin resonance experiments on donors in silicon. III. Investigation of excited states by the application of uniaxial stress and their importance in relaxation processes. *Phys. Rev.* **124,** 1068–1083 (1961).
24. Waugh, J. S. & Slichter, C. P. Mechanism of nuclear spin-lattice relaxation in insulators at very low temperatures. *Phys. Rev. B* **37,** 4337–4339 (1988).
25. Kohn, W. *Solid State Physics* Vol. 5 (eds Seitz, F. & Turnbull, D.) 257–320 (Academic, New York, 1957).
26. DiVincenzo, D. P. Two-bit gates are universal for quantum computation. *Phys. Rev. A* **51,** 1015–1021 (1995).
27. Lloyd, S. Almost any quantum logic gate is universal. *Phys. Rev. Lett.* **75,** 346–349 (1995).
28. Herring, C. & Flicker, M. Asymptotic exchange coupling of two hydrogen atoms. *Phys. Rev.* **134,** A362–A366 (1964).
29. Andres, K., Bhatt, R. N., Goalwin, P., Rice, T. M. & Walstedt, R. E. Low-temperature magnetic susceptibility of Si:P in the nonmetallic region. *Phys. Rev. B* **24,** 244–260 (1981).
30. Ashcroft, N. W. & Mermin, N. D. in *Solid State Physics* Ch. 32 (Saunders College, Philadelphia, 1976).
31. Larsen, D. M. Stress dependence of the binding energy of D^- centers in Si. *Phys. Rev. B* **23,** 5521–5526 (1981).
32. Larsen, D. M. & McCann, S. Y. Variational studies of two- and three-dimensional D^- centers in magnetic fields. *Phys. Rev. B* **46,** 3966–3970 (1992).
33. Ashoori, R. C. Electrons in artificial atoms. *Nature* **379,** 413–419 (1996).
34. Abragam, A. *Principles of Nuclear Magnetism* (Oxford Univ. Press, London, 1961).
35. Lyding, J. W. UHV STM nanofabrication: progress, technology spin-offs, and challenges. *Proc. IEEE* **85,** 589–600 (1997).
36. Adams, C. S., Sigel, J. & Mlynek, J. Atom optics. *Phys. Rep.* **240,** 143–210 (1994).
37. Warren, W. S. The usefulness of NMR quantum computing. *Science* **277,** 1688–1690 (1997).

Correspondence should be addressed to the author (e-mail: kane@newt.phys.unsw.edu.au).